eman ta zabal zazu

Universidad Euskal Herriko
del País Vasco Unibertsitatea

Understanding of plasticizer effect on the temperature dependence of mechanical and dielectric relaxation function of polymers of interest for tire formulation.

PhD Thesis Submitted by

Thomas Gambino

to the

University of the Basque Country

Thesis supervisors:

Prof. Angel Alegría Loinaz
Prof. Juan Colmenero de León

Donostia - San Sebastían, 2019

Institutions

UPV/EHU : San Sebastían (Gipuzkoa) - Spain

Materials Physics Center : San Sebastían (Gipuzkoa) - Spain

Campus RDI - MICHELIN Ladoux- France

Understanding of "plasticizer" effect on the temperature dependence of mechanical and dielectric relaxation function of polymers of interest for tire formulation.

Abstract

Dynamic properties of elastomers in linear regime are one of the central research lines of Michelin Company. The understanding of plasticizer effect on the temperature dependence of mechanical relaxation is a key point in order to improve the performance of a tire such as adherence and decreasing rolling resistance.

Synthetic rubbers are widely used matrices component in order to produce tire. Almost all important rubber products in industry applications include blends in their compositions. Generally several type of rubbers are mixed and often plasticizers are added to the final system. The main reason for blending components is to combine the desirable properties exhibited by the original pure component. The dynamic properties of the system can be tuned by mixing components concentration and therefore find the optimal product regarding the different properties required for a tire. In addition, many other components such as fillers, antioxidant or vulcanization additives are added to the final mixture, leading to a high technology product, whose properties strongly depend on the interactions among those ingredients.

In this PhD, we present a study concerning the dynamics of Styrene Butadiene Rubber (SBR) mixed with an oligomer of polystyrene (PS) allowing to tuned the dynamic properties of the tire main material. This simplified industrial system was studied by means of Broadband Dielectric Spectroscopy (BDS), Differential Scanning Calorimetry (DSC), Dynamic Mechanical Analysis (DMA), Rheological measurements as well as elastic and inelastic Neutron Scattering instruments (NS).

The first chapter of this thesis is a general overview on polymers. We will define what are polymers, their structures and different physical properties. Then we will introduce the glass transition phenomena and the origin of relaxation processes in polymers. Finally, we will give the basis notions of polymer mixing.

In the second chapter the samples used all along this study are introduced. The different experimental method and the theoretical concepts related are explained.

In chapter 3, the methodology and concepts developed over the past years for the study of segmental dynamics on miscible polymer blends have been

applied to the investigation of a blend SBR/PS (50/50). In this way we obtain detailed information about the segmental dynamics of both components within the blend. To this end, a judicious combination of broad-band dielectric spectroscopy (BDS) and quasi-elastic neutron scattering (QENS) results on deuterium-labeled blends was required. The strategy for data analysis developed in this work made it possible to readily resolve the components segmental dynamics of the investigated mixtures. We will show that Gaussian distributions of the components effective glass-transition temperatures provide a very good description of all the experimental data collected over the whole accessible temperature range, not only by BDS and QENS but also those obtained by differential scanning calorimetry and by neutron elastic fixed window scan experiments.

In chapter 4, we will detailed a simple and fully predictive dielectric model which works over a very broad range of concentration in PS in the blends up to 70 wt%. This model is based on the theoretical concepts of thermally driven concentration fluctuations and self-concentration. A good agreement was obtained between the experimental results and the outputs of the model using only three fitting parameters. The smooth variation of these parameters with average composition also allows the evaluation of the dielectric relaxation of any intermediate composition. Moreover, we have shown how the model remains also valid for evaluating the dielectric relaxation at higher frequencies.

In chapter 5, the miscibility of the SBR/PS blends are studied from the SANS experiments, leading to the determination of the temperature dependence of the Flory interaction parameter. The combination of the dielectric modelling and the SANS analysis made possible to estimate the radius of the sphere, taken as the relevant volume to describe the fluctuation of concentration in the blend. This radius is found to be of the order of 10 $\dot{A}$, independent of the temperature and the concentration.

Finally, in chapter 6 the model previously presented for the modelling of the dielectric relaxation will be adapted in order to predict the high frequencies mechanical behaviour of SBR/PS blends. This model is fully predictive, and can be run at any desirable frequency/temperature and concentration of interest. In particular, by using the model above presented, one can predicted the high frequency mechanical behaviour of the SBR/PS blends, which is impossible to be directly measured by any experimental mechanical characterisation technique.

The main objective of this PhD thesis is to enhance the knowledge about the dynamics of polymer blends, with applications in the tire industry. An advanced understanding of the polymer dynamics as well as the prediction of the high frequencies mechanical properties will improve the design of materials with desired properties.

Key-words: miscible polymer blends, blend dynamics, dielectric spectroscopy, neutrons scattering, dynamic mechanical analysis.

Comprensión del efecto "plastificante" sobre la dependencia en temperatura de las funciónes de relajación mecánica y dieléctrica para polímeros de interés para la formulación de neumáticos.

Resumen

Las propiedades dinámicas de los elastómeros en régimen lineal son una de las líneas de investigación centrales de Michelin. La comprensión del efecto del plastificante en la dependencia en temperatura de la relajación mecáníca es un punto clave para mejorar el rendimiento de un neumático, en particular aumentar la adherencia durante el frenado y la disminución de la resistencia a la rodadura. De hecho, durante su período de uso, el neumático debe disipar la mayor cantidad de energía posible durante el frenado, sin embargo, debemos minimizar este proceso durante el rodamiento regular. Variar la temperatura de transición vítrea (T_g) del sistema permite modificar el dominio de la frecuencia y la temperatura en el que el material disipa la energía.

La transición vítrea es un concepto clave en el estudio de los polímeros y sus aplicaciones. Los polímeros generalmente están formados por una estructura de cadena larga y tienen una alta viscosidad en estado líquido. Cuando se realiza un enfriamiento, los movimientos moleculares se vuelven más lentos. A veces las estructuras químicas no son compatibles con la formación de una fase cristalina. De este modo, el polímero mantiene una conformación desordenada como un líquido, aunque la viscosidad es tan alta que el polímero podría verse como un sólido. La estructura de no equilibrio resultante se conoce como estado vítreo y la pérdida del fenómeno de equilibrio que conduce al estado vítreo se conoce como transición vítrea. En general, los valores de T_g muy por debajo de la temperatura ambiente definen el dominio de los elastómeros debido a que el enmrañameinto de las cadenas largas produce una respuesta elastica importante, a pesar de ser materiales relativamente blandos. Aquellos polímeros con valores de T_g por encima de la temperatura ambiente definen polímeros rígidos. Los polímeros amorfos exhiben diferentes procesos de relajación. A bajas temperaturas se produce la relajación secundaria (β), que se atribuye a la aparición de movimientos locales de pequeña amplitud. Calentando por encima de T_g, observamos la aparición de la relajación principal (α), que corresponde a una caída del módulo mecánico de varias décadas desde valores de unos pocos GPa (tipicos de un solido), y se atribuye a reordenamientos de varias unidades monoméricas que están bloqueadas por debajo de T_g. Esta brusca bajada el modulo mecco lleva asociada un gran disipacicca lo que explica que la T_g sea un

parametro clave en el contexto de las propiedades del material objeto de nuestro estudio.

La temperatura de transición vítrea de un polímero se ve generalmente fuertemente afectada al agregar un plastificante. Un plastificante suele ser una pequeña molécula que se inserta entre las cadenas de polímero y las espacia entre sí. Este proceso aumenta el volumen libre. Por lo tanto, las cadenas de polímero pueden deslizarse unas sobre otras más fácilmente y moverse a diferentes temperaturas de lo que lo harían sin el plastificante. Este segundo componente hace posible lograr mejores características de procesamiento de compuestos, al tiempo que proporciona flexibilidad en el producto de uso final. Sin embargo, también es posible usar, como en nuestro caso, como "plastificantes" una cantidad de cadenas poliméricas de otro tipo que las de la matriz polimérica. En ese caso, la palabra utilizada "plastificante" podría no ser apropiada porque, dependiendo del tipo de polímero usado como "plastificante", la temperatura de transición vítrea de la matriz del polímero puede aumentar, con respecto a la del polímero inicial. Este tipo de sistemas pertenece a la categoría de mezclas de polímeros miscibles.

Las mezclas de polímeros miscibles son en general tecnológicamente interesantes porque pueden conducir a nuevos materiales sin los gastos de tiempo y económicos requeridos para realizar nueva síntesis. La capacidad de comprender el comportamiento de las mezclas de polímeros miscibles, basado en el comportamiento de los polímeros puros que forman la mezcla, es un punto clave para diseñar mezclas de polímeros con las propiedades apropiadas. La dinámica y el comportamiento de relajación de las mezclas de polímeros son particularmente complicados de predecir. De hecho, los estudios de calorimetría típicamente revelan una única transición de vítrea ancha. Sin embargo, las sondas de dinámica segmental, como la espectroscopia dieléctrica de banda ancha (BDS) y resonancia magnetica nuclear por ejemplo, revelan que cada componente de la mezcla puede mostrar una dinámica distinta. Se han propuesto modelos teóricos basados en conceptos tales como las fluctuaciones expontaneas de concentración y la autoconcentración para explicar el comportamiento dinámico de la mezcla y sus componentes. Cuando una mezcla de polímeros en la región monofásica se acerca al límite de estabilidad de fase, se producen variaciones de la concentración al rededor del valor promedio, que se define como fluctuaciones de la concentración. Por otro lado, en una mezcla de polímeros miscible, debido a la conectividad de la cadena, el entorno local de un monómero de tipo A será, en promedio, rico en A en comparación con la composición en masa, y de manera similar para B. Este efecto se ha llamado como autoconcentración. El efecto de la mezcla en la dinámica del polímero se ha estudiado para numerosos sistemas. Nuestro estudio se centrará en la mezcla SBR/PS, un sistema industrial simplificado. Los cauchos de estireno butadieno (SBR) son los cauchos sintéticos más prevalentes que se derivan de la copolimerización de estireno y butadieno. Estos materiales tienen una buena resistencia a la abrasión y una buena estabilidad al envejecimiento cuando están protegidos por aditivos. Alrededor del 50% de los neumáticos de automóviles están hechos de diferentes tipos de SBR.

La relación estireno / butadieno tiene un fuerte efecto sobre las propiedades del polímero. Un oligómero de poliestireno, como aditivo de mayor T_g que SBR, será el segundo componente de las mezclas de polímeros dinámicamente asimétricas binarias que estudiaremos en este trabajo.

La reometría junto con la espectroscopía mecánica son técnicas convenientes para investigar el comportamiento dinámico mecánico de los polímeros en el rango de 10^{-3} Hz a 10^2Hz. Sin embargo, a mayor frecuencia, lo que corresponde a tiempos de relajación más cortos, estas técnicas no son apropiadas. La espectroscopia dieléctrica de banda ancha (BDS) es un método poderoso para el estudio de movimientos moleculares de materia blanda en un amplio intervalo de frecuencia (10^{-3} Hz a 10^9Hz) y rango de temperatura. El objetivo general de este estudio es investigar cómo podemos deducir del BDS, las propiedades mecánicas de alta frecuencia de un sistema de polímero dado y en particular de las mezclas de SBR/PS.

Esta tesis está dividida en seis capítulos:

El primer capítulo de esta tesis es una descripción general de los polímeros. Detallaremos sus estructuras y diferentes propiedades físicas. Luego introduciremos los fenómenos de transición vítrea y el origen de los procesos de relajación en los polímeros. Finalmente, explicaremos las nociones básicas de termodinamica de mezcla de polímeros.

En el segundo capítulo se presentan las muestras utilizadas a lo largo de este estudio. Se dan las diferentes propiedades físicas de los polímeros puros, así como el procedimiento de mezcla. Los diferentes métodos experimentales y los conceptos teóricos relacionados con las distintas tecnicas utilizadas estan tambíen explicados.

En el capítulo 3, se dedica a la metodología y los conceptos desarrollados en los útimos años para el estudio de la dinámica segmental en mezclas de polímeros miscibles y que se han aplicado primero a la investigación de una mezcla de SBR/PS (50/50) a modo de test. De esta manera, obtenemos información detallada sobre la dinámica segmental de ambos componentes dentro de la mezcla. Desde un punto de vista académico, observamos que no es obvio que los conceptos teóricos desarrollados y verificados en sistemas canónicos de mezcla de polímeros también se aplicarían al caso complejo de una mezcla de un copolímero y un oligómero. Como técnicas experimentales, en este capítulo, utilizamos DSC, BDS y dispersión de neutrones (mediciones tanto de exploración de ventana fija cuasi elástica (QENS) como elástica, junto con difracción con análisis de polarización). Para explotar la selectividad de la dispersión de neutrones, es obligatorio el uso de muestras en las que uno de los componentes está deuterado. La obtención de compuestos deuterados produce cambios en la microestructura del polímero, planteando dificultades en el análisis conjunto de los resultados experimentales. Estas difficultades fueron superadas con una combinación de BDS y QENS en todas las muestras parcialmente deuteradas utilizadas en este trabajo. El ansis de los datos se basa en la aplicación de

un modelo que considera dos ingredientes clave en los sistemas de mezcla: la heterogeneidad dinámica y las fluctuaciones de concentración. Los resultados obtenidos de esta manera muestran que el efecto de la mezcla de oligómero PS con SBR en cada componente se codifica principalmente en una distribución de T_g originada a partir de estos ingredientes combinados. El rango de temperatura cubierto por las distribuciones obtenidas concuerda bien con el de la de transición vítrea amplia que caracteriza estos materiales según lo observado por DSC. Además, también encontramos un buen acuerdo entre el rango de T_g deducido de los componentes individuales y el inicio del "ablandamiento microscópico" revelado por la pérdida de intensidad de la dispersión elástica de neutrones según se aumenta la temperatura. Conviene destacar que estos buenos acuerdos se obtienen a pesar de la complejidad de las mezclas investigadas, donde las propiedades dinámicas de los componentes puros se ven afectadas por diferencias relativamente pequeñas en la composición del copolímero y / o la microestructura de los polímeros involucrados. Esto apoya la robustez del enfoque seguido.

En el capítulo 4, detallamos un modelo dieléctrico simple y totalmente predictivo que funciona en un rango muy amplio de concentración en PS en las mezclas de hasta 70% en peso en polístireno. Este modelo se basa en los conceptos teóricos de las fluctuaciones térmicas de concentración y la autoconcentración. Se obtuvo un buen acuerdo entre los resultados experimentales y los resultados del modelo utilizando solo tres parámetros de ajuste. La suave variación de estos parámetros con la composición promedio permite también la evaluación de la relajación dieléctrica de cualquier composición intermedia. Además, hemos demostrado que el modelo también es válido para evaluar la relajación dieléctrica en frecuencias más altas.

En el capítulo 5, la miscibilidad de las mezclas SBR / PS se ha estudiado a partir de los experimentos de neutrones de bajos angulos (SANS), lo que lleva a la determinación de la dependencia con la temperatura del parámetro de interacción de Flory. La combinación del modelado dieléctrico y el análisis de SANS hizo posible estimar el radio de una esfera, que representa el volumen relevante para describir la fluctuación de concentración en la mezcla. Se encuentra que este radio es del orden de $10\mathring{A}$, y es independientemente de la temperatura y la concentración.

En el capítulo 6, finalmente, hemos adaptado el modelo presentado anteriormente para el modelo de la relajación dieléctrica con el fin de predecir el comportamiento mecánico de altas frecuencias de las mezclas de SBR/PS. Este modelo es totalmente predictivo y puede ejecutarse a cualquier frecuencia / temperatura y concentración de interés. En particular, utilizando el modelo presentado anteriormente, se puede predecir el comportamiento mecánico de alta frecuencia de las mezclas SBR / PS, lo cual es imposible de determinar directamente mediante cualquier técnica experimental de caracterización mecánica actualmente disponible.

Resumiendo, los resultados obtenidos en esta tesis doctoral permiten obtener

una mejor comprensión de la dinámica de las mezclas de polímeros, así como la predicción de las propiedades mecánicas de alta frecuencia que podrían ser un punto determinante para facilitar una mejora significativa en el diseño de materiales con propiedades deseadas.

Sin embargo, el trabajo aquí presentado se aplicó a un sistema industrial muy simplificado, compuesto por un elastómero y un segundo componente que permite ajustar las propiedades dinámicas del material principal del neumático. Los neumáticos generalmente están compuestos de hasta 200 materias primas diferentes, que se combinan con compuestos de caucho para crear los diversos componentes de un neumático en sú estado final. De cara a un trabajo futuro, sería muy interesante poder predecir las propiedades mecánicas de altas frecuencias de un sistema más "realista" y, por lo tanto, más complicado, añadiendo, por ejemplo, al sistema actual las cargas habituales utilizadas en la industria como las particulas de negro de humo por ejemplo, muy conocidas por su aptitud a mejorar las propiedades mecánicas de las mezclas de caucho. En la práctica, el SBR como caucho sintético se sustituye a menudo en gran parte por el caucho natural (NR) basado en el coste comparativo de las materias primas. Por lo tanto, sería también interesante ver cómo podríamos adaptar este estudio a las mezclas de NR/SBR/PS.

Palabras-clave: mezclas polimericas miscibles, dinámicas de mezclas, espectroscopía dieléctrica, espectroscopía mecánica, dispersión de neutrones.

Contents

Chapter 1

Introduction

After a brief overview on polymer properties, we will introduce the glass transition phenomena and the viscoelastic behaviour of polymers. In the linear regime, several more local relaxation processes are observed. Starting by the segmental α-relaxation and then followed by lower temperature secondary relaxation processes, we will discuss their origins and the different way to modify their behaviour.

1.1   Overview on polymers properties

A polymer is a material composed of long molecular chains called macromolecules. A macromolecule is obtained by polymerisation of small organic molecules called monomers. Molecular weight distribution functions are used to reflect the different molecular weight of the chains of a given polymer due to polymerisation conditions. The number-average molecular weight M_n and the weight average molecular weight M_w are respectively defined as

$$M_n = \frac{\sum_i N_i M_i}{\sum_i N_i} \tag{1.1}$$

and

$$M_w = \frac{\sum_i N_i M_i^2}{\sum_i N_i M_i} \tag{1.2}$$

with N_i the number of molecules of molecular weight M_i. The polydispersity index is defined as the ratio $M_w/M_n \geq 1$ and gives informations on the broadness of the molecular weight distribution.

As can be observed in Scheme 1.1 polymers are usually either amorphous which corresponds to non-organised macromolecules or semi-cristaline where part of the chains are organised but a partial disorder in the material is also observed. In this study only amorphous polymers are considered. The cohesion
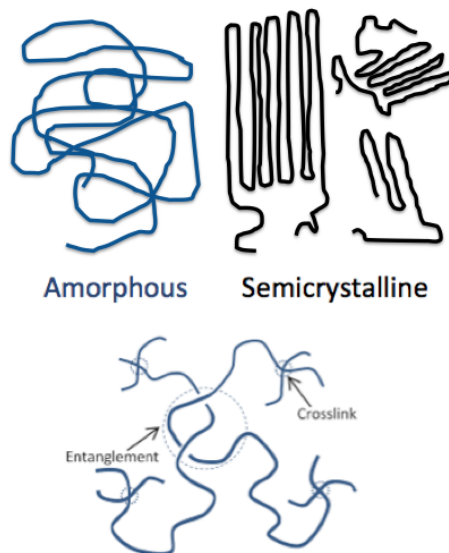
Figure 1.1: The arrangement of molecular chains in amorphous and semicrystalline polymers. In the lower scheme, the entanglement and cross link can be appreciated.

between chains is assured by physical interactions such as Van der Waals interactions. In the case of vulcanised samples, cohesions between polymer chains are also chemical. In order to obtain cross-linked polymer chains, a vulcanization recipe has to be mix with the initial polymer. In the case of elastomers, sulphur is a widely used additive in order to obtain cross links in the polymer matrix. The latter is able to build sulphur bridges in between two polymer chains. However this process is very long which imply unacceptable cost from an industrial point of view, thus activators and accelerators are usually added to the vulcanisation recipe.

1.2 The glass transition

1.2.1 The vitrification phenomena

The glass transition phenomenon is a common feature in all amorphous systems such as glasses or polymers.

Figure 1.2 shows the evolution of the thermodynamic state functions such as Volume (V), Entropy (S) and the Hentalpy (H) in function of the temperature. Because of the long entangled chains, when the polymer is cool down from is liquid state, crystallisation process is difficult. Moreover, the presence of irregular polymer microstructures also interfere with crystallization. Therefore, in many polymers crystallization cannot occur or only partially. When the temperature

is below the melting temperature, the amorphous phase is in the supercooled state. If the temperature keep decreasing, the so called *glass transition temperature* T_g is reached, and the high viscosity prevent the atoms rearrangement that would allow thermodynamic equilibrium to occur so a glassy state is reached.
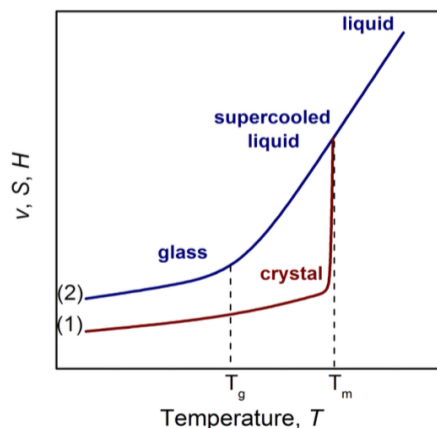

Figure 1.2: Evolution of the thermodynamic state functions with temperature.

The glassy state is then a non-equilibrium state and the glass transition is a kinetic phenomenon. Thus the temperature at which the glass transition occurs, T_g, is strongly linked to the cooling rate. The slower the cooling rate, the longer the molecules get to rearranged and the lower is the glass transition temperature. It is thus more convenient to define a glass transition domain than a single and unique glass transition temperature.

From a mechanical perspective, as can be observed in Scheme 1.3 in polymers we can identify three main domains, showing different features of the mechanical modulus as a function of the temperature, at a given frequency in the 10^{-2} - 10^3Hz range.

In the low temperature domain (a), the material is solid like, showing high modulus. The molecular motions are localised and sometimes the material is brittle.

In the intermediate temperature domain (b), around the glass transition temperature, a sudden change in the mechanical behaviour is observed as the value of the mechanical modulus suddenly drops by several decades. The molecular motions occur at the segmental level. The appearance of a rubbery plateau is the result of physical entanglements or crosslinks avoiding chain segments displacement over large distances. Both the width of this region as well as some properties of the polymer depend on the molecular weight between entanglements or crosslinks. Only polymers that are long enough can form stable flow restricting entanglements.

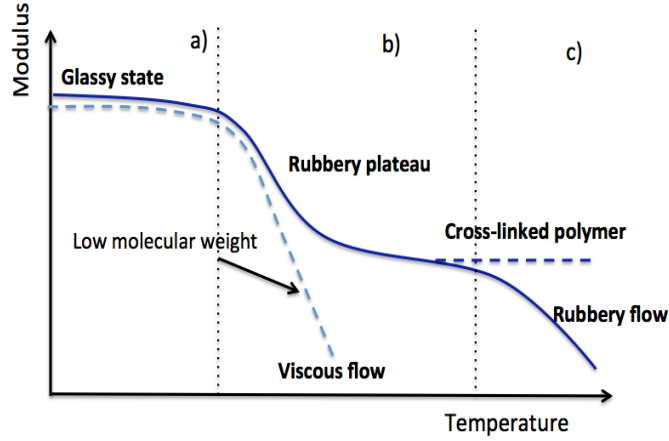In the last domain (c), above the glass transition temperature, the material

Figure 1.3: Evolution of the mechanical modulus in function of the temperature at a given frequency.

is fluid. Molecular motions are of larger amplitudes. The end of the rubbery plateau corresponds to the chains flowing. However when the polymer chains are permanently cross-linked, no flowing of the chains can be observed.

1.2.2 Viscoelastic behaviour of polymers

When an oscillatory stress is applied to a material, different scenarios can be distinguish:
- For purely elastic materials the stress and strain occur in phase.
- For purely viscous materials, there is a delay between stress and strain which manifest by a 90 degree phase difference.
- Viscoelastic materials are in between these two scenarios and present some phase delay (ζ) between 0 and 90 degree (see Figure 1.4).

In the time domain, respectively the strain and stress can be written as

$$\sigma(t) = \sigma_0 cos(\omega t) \tag{1.3}$$

$$\epsilon(t) = \epsilon_0 cos(\omega t - \zeta) \tag{1.4}$$

Which leads, in complex notation to :

$$\sigma^*(t) = \sigma_0 exp(i\omega t) \tag{1.5}$$

$$\epsilon^*(t) = \epsilon_0 exp(i\omega t) exp(-i\zeta) \tag{1.6}$$

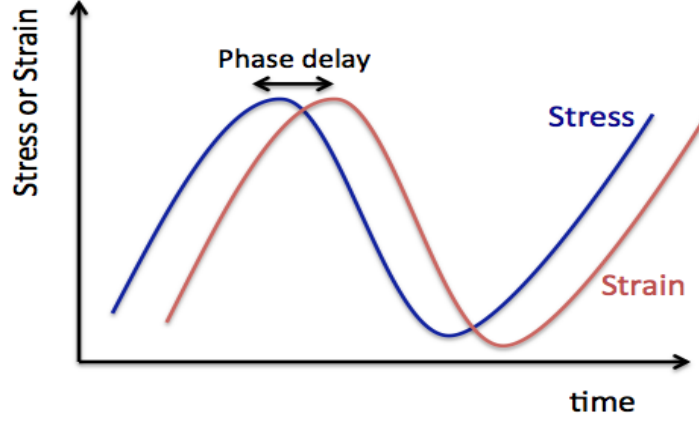For traction/compression the modulus is defined as follow:

13

Figure 1.4: Illustration of the strain's phase delay for an applied oscillatory stress.

$$E^*(\omega) = \frac{\sigma^*(t)}{\epsilon^*(t)} = E'(\omega) + iE''(\omega) \tag{1.7}$$

Where E' is the storage mechanical modulus and E'' is the dissipation modulus. G' and G'' are used to defined the mechanical modulus for shear experimental strain. E'' and G'' correspond to the energy that has been dissipated during a measurement cycle, whereas E' and G' correspond to the elastic energy which has been stored. The phase angle between stress and strain is obtained as:

$$tan(\zeta) = \frac{E''(\omega)}{E'(\omega)} = \frac{G''(\omega)}{G'(\omega)} \tag{1.8}$$

The phase angle is related to the disparity of the measured material regarding to a perfect elastic behaviour.

1.2.3 The origins of relaxation processes in polymers

The dynamic of glass forming systems are very complex and often involve several relaxation processes. Relaxations in polymers can involve different molecular entities. In addition of the polymer specific relaxation phenomena related with the polymer chain dynamics, polymers present a structural relaxation similar to that of all viscous liquids, the so called α-relaxation. Moreover, in polymers some relaxations may occur which involve smaller scale molecular rearrangements. These latter ones are secondary relaxation processes such as the so-called β and γ processes and mainly concerns some specific functional groups or side groups attached to the main backbone.

The segmental α-relaxation

The α-relaxation is strongly connected to the glass transition of polymers and the molecular motions involved in this process depend drastically on temperature. Approaching Tg from the melt, the molecular motions drastically slow down and the system appears frozen. The temperature dependence of the characteristic relaxation time associated can usually be well described by a Vogel-Fulcher-Tamann function:

$$\tau = \tau_0 \, exp\left(\frac{D \cdot T_0}{T - T_0}\right) \tag{1.9}$$

where τ_0 is the parameter that represents the relaxation time at $T \to \infty$, and the fragility parameter D are temperature independent. The Vogel temperature T_0 represents the temperature at which the characteristic relaxation time would diverge.

The Vogel-Fulcher-Tamann law can be justified by two main theoretical approaches. The first one, the free volume theory proposed by Doolittle [26] and then improved by Cohen [22] [21] and Turnbull [61] is the most common theory that has been proposed in order to model the segmental relaxation associated to the glass transition of amorphous systems. In this theory every single molecule can be model by a sphere, trap in a cage which is formed by the interactions with is closer neighbours. At low temperature, the average size of these cages v_m tend to v_0 which corresponds to the size of the cage without thermal agitation in a compact arrangement. When the temperature increases, the size of the cages also increases. At a given temperature T_0, the size of the cages is big enough to allow molecules to move under a constant potential energy U. This multiplication of molecular motions results in a brutal increase of the thermal expansion as well as the heat capacity. Molecular motions are then only possible if the size of the empty space is superior or equal than the size of the molecule. The material is then able to rearranged is structure by diffusion process with an average time τ_m:

$$\tau_m = \tau_0 \, exp\left(\frac{v_0}{v_{fm}}\right) \tag{1.10}$$

With v_{fm} being the average free volume.

Later, *Adam and Gibbs* [2] introduced the concept of cooperatively rearranging region (CRR) defined as a subsystem which, upon a sufficient thermal fluctuation, can arrange into another configuration independently of its environments. This theory relates the increase of structural relaxation time (τ) to the reduction of configurational entropy (S_c) by:

$$\tau(T) = \tau_0 \, exp\left(\frac{C_0}{TS_C}\right) \tag{1.11}$$

where C_0 is a constant which depends on the polymer type. The configurational entropy is not experimentally accessible, and therefore it is usually

estimated from the excess entropy ($S_C \propto S_{ex} = S_{melt} - S_{crystal}$). Thus, S_C can be written as

$$S_C(T) = gS_{ex}(T) = g \int_{T_k}^{T} \frac{\Delta C_p(T')}{T'} dT' \qquad (1.12)$$

where $\Delta C_p(T)$ is the excess heat capacity and T_k is the Kauzmann temperature where eventually the entropy of the equilibrated supercooled melt equals that of the corresponding crystalline material. If an inverse temperature dependence is assumed for ΔC_p ($\Delta C_p = \frac{k}{T}$) the VFT equation is recovered with $T_0 = T_K$.

The non-Arrhenius behaviour of the temperature dependence of the primary relaxation is an universal aspect of the α-relaxation occurring in all glass forming systems. In connection to this feature, the dynamic fragility parameter m is defined as:

$$m = \frac{\partial log\tau}{\partial(\frac{T_g}{T})}\Big|_{T=T_g} \qquad (1.13)$$

This dynamic parameter allow to classify the system as fragile or strong according to the Angell's criteria [7]. According to the way the characteristic relaxation time τ_α approaches the glass-transition temperature, the system showing a pronounced non-Arrhenius dependence are classified as fragile, while those manifesting an Arrhenius-like behaviour on temperature are called strong. According to this classification glass-forming polymers are usually classified as fragile.

The fragility D from the Vogel-Fulcher-Tamann law and the m parameter from Angell's criteria can be connected by the following equation:

$$m = \frac{T_g \, [ln\frac{\tau_{Tg}}{\tau_0}]^2}{D \, T_0 \, ln10} \qquad (1.14)$$

where τ_{Tg} is the relaxation time when $T = T_g$.

Usually for polymers, we have $\tau_{Tg} \approx 10^2 s$, $\tau_0 \approx 10^{-14} s$. The previous equation can be then expressed as:

$$m = \frac{590 \, T_g}{D \, T_0} \qquad (1.15)$$

As expected, when D from the Vogel-Fulcher-Tamann law has a high value, the Angell's parameter is low which imply a low fragility material and vice versa.

Relaxation in the Glassy State, Secondary relaxations processes

The secondary relaxations processes correspond to localised molecular motions which represent a separate subsystem in the sense of statistical thermodynamics. This implies that the system of the side groups is characterised by a specific

partial temperature and relaxation time. Depending on the molecules, the motions can be more or less cooperative. In the glassy state, the temperature dependence of the characteristic times can be describe by the Arrhenius law:

$$\tau = \tau_0 \, exp \, (\frac{E_a}{k_B T}) \qquad (1.16)$$

where τ_0 is the parameter that represents the relaxation time at $T \rightarrow \infty$, E_a represents the activation energy of the process and k_B is the Boltzmann's constant.

In the case of the present study only the Styrene Butadiene Rubber (SBR) copolymer present a significant β-relaxation process which is associated to local motions of butadiene monomers and therefore not affected by the presence of styrene [33].

The amplitude of the secondary processes is generally weak compared to the main segmental relaxation. In the case of SBR the dielectric intensity of the principal segmental relaxation is about three times stronger than the secondary one.

1.3   Thermodynamic of mixing

Mixtures are systems consisting of at least two components, binary mixtures consist of only two different species. If the mixture is uniform and all the components of the blend are intermixed on a molecular scale, the mixture is called homogenous. In the opposite case, if the mixture is composed of several different phases the blend is called heterogenous. One of the most typical example of this kind of mixture is that of oil and water. The entropy and energy changes on mixing are the key parameters in order to determined if an equilibrium state of a given mixture is homogenous or heterogenous. In this section we will describe a binary mixture under a lattice model with no volume change.[63]

1.3.1   Entropic contribution

We consider two components, A of volume V_A and B of volume V_B. The following assumptions are made:
i) The volume is conserved during mixing and the binary mixture has then a total volume of $(V_A + V_B)$.
ii) The conformational entropy of the component is identical in the mixed and pure states, and the mixture is macroscopically uniform.
iii) The two components are randomly mixed to fill the entire lattice.

The volume fraction of the components can be written as :

$$\Phi_A = \frac{V_A}{V_A + V_B}$$

$$\Phi_B = \frac{V_B}{V_A + V_B} \tag{1.17}$$

$$= 1 - \Phi_A$$

We defined the lattice site volume v_0 as the smallest units occupied by one constituting unit as molecules or monomers. Larger molecules like polymers occupy multiple connected lattice sites. The molecular volume of a molecule of component A can be written as :

$$V_A = N_A v_0 \tag{1.18}$$

N_A being the number of lattice site occupied by the component A. Polymer blends are mixtures of macromolecules of different chemical spices in which N_A and $N_B \geq 1$. The total system of volume $(V_A + V_B)$ occupies n lattice sites with:

$$n = \frac{V_A + V_B}{v_0} \tag{1.19}$$

The number of molecules of the component A can be expressed as:

$$n_A = \frac{n\Phi_A}{N_A} \tag{1.20}$$

The entropy S is determined as:

$$S = k_B ln(\Omega) \tag{1.21}$$

with Ω the number of states which is the number of ways to arrange molecules on the lattice. In an homogeneous mixture of A and B, the number of translational states of a given single molecule Ω_{AB} is the number of independent positions that the molecule can have on the lattice:

$$\Omega_{AB} = n \tag{1.22}$$

In a pure A state before mixing, the number of states Ω_A of each molecules of component A is

$$\Omega_A = n\Phi_A \tag{1.23}$$

The entropy change on mixing can be written for a single molecule of component A as:

$$\Delta S_A = k_B \, ln(\Omega_{AB}) \, - \, k_B \, ln(\Omega_A) = -k_B \, ln(\Phi_A) \tag{1.24}$$

Considering a binary mixture we have respectively $\Phi_A < 1$, $\Phi_B < 1$ and as a consequence the entropy change upon mixing is always positive. The total entropy of mixing can be calculated as:

$$\Delta S_{mix} = n_A \Delta S_A \ + \ n_B \Delta S_B = -k_B[n_A ln(\Phi_A) + n_B ln(\Phi_B)] \qquad (1.25)$$

Finally, the entropy of mixing per lattice site $\Delta \bar{S}_{mix} = \Delta S_{mix}/v_0$ is defined as

$$\Delta \bar{S}_{mix} = -k_B \left[\frac{\Phi_A}{N_A} ln(\Phi_A) \ + \ \frac{\Phi_B}{N_B} ln(\Phi_B) \right] \frac{n}{v_0} \qquad (1.26)$$

1.3.2 Energetic contribution

The energy of mixing can be negative in the case of promoting mixing or positive for unfavourable case of mixing. In order to estimate the energy of mixing, using the lattice model, we assume each component being places randomly into the lattice sites ignoring any possible correlations. Favourable or unfavourable interaction between components are considered small enough to not affect the random placement. This mean-field approach does not take into account the chain connectivity between monomers. Here we assume that the monomer volume of component A and component B are the same. The regular solution theory predicted that the energy of mixing between adjacent lattice sites occupied by the two component A and B can be split in three pairwise interaction energies, namely u_{AA}, u_{AB}, u_{BB}. The average pairwise interaction U_A of a monomer of component A occupying one lattice site with a neighbouring monomer on one of the adjacent sites can be determined using a mean field approach. In the following, we will write $\Phi_A = \Phi$ and $\Phi_B = 1 - \Phi$, assuming that the probability of the neighbour being a monomer of component A is equal to the volume fraction of these molecules.The average pairwise interaction of an A-monomer with one of its neighbouring monomers is:

$$U_A = u_{AA}\Phi \ + \ u_{AB}(1 - \Phi) \qquad (1.27)$$

The coordination number of the lattice z represents for each lattice site the number of closest neighbours. The average interaction energy for an A monomer with is z neighbours is therefore zU_A. Every pairwise interaction being counted twice, once for the monomer and once for its neighbour, the average energy per monomer is $\frac{1}{2}zU_A$. Therefore the total interaction energy can be written as:

$$U = \frac{zn}{2}[U_A\Phi + U_B(1-\Phi)] \ = \ \frac{zn}{2}[u_{AA}\Phi^2 + 2u_{AB}\Phi(1-\Phi) + u_{BB}(1-\Phi)^2] \quad (1.28)$$

with $n\Phi$ the number of A monomers. The total energy before mixing U_0 is then the sum of the two pure components energies:

$$U_0 = \frac{zn}{2}[u_{AA}\Phi + u_{BB}(1 - \Phi)] \qquad (1.29)$$

Therefore the energy change upon mixing per site can be expressed as:

$$\Delta \bar{U}_{mix} = \frac{U - U_0}{n} = \frac{z}{2}\Phi(1 - \Phi)(2u_{AB} - u_{AA} - u_{BB}). \qquad (1.30)$$

The difference of interaction energies in the mixture is characterized by the Flory interaction parameter χ which can be expressed as:

$$\chi = \frac{z}{2kT}(2u_{AB} - u_{AA} - u_{BB}) \qquad (1.31)$$

The Flory interaction parameter is a dimensionless measure of the differences in the strength of pairwise interaction energies between components in the mixture. The energy of mixing per lattice site can therefore be written as:

$$\Delta \bar{U}_{mix} = \chi\Phi(1 - \Phi)kT \qquad (1.32)$$

For miscible polymer blends χ is generally deduced from Small-Angle Neutron Scattering (SANS) measurements which usually involved deuterium labelling of one of the blend component. Assuming that there is no volume change upon mixing of the two component is a strong assumptions of the Flory-Huggins theory. Another hypothesis is that both components can fit on the sites of the same lattice. However, in almost all polymer blends, the volume per monomer change upon mixing, and some local packing effect occur. These phenomenas can be taken into account by the addition of a temperature independent constant in the expression of χ:

$$\chi \simeq A + \frac{B}{T} \qquad (1.33)$$

The parameters A and B have been determined for many polymer blends, A being the parameter which take into account the entropic part while B account for the enthalpic part.

1.3.3 Phase diagram

The Helmholtz free energy of mixing per lattice site $\Delta \bar{F}_{mix}$ can be defined as:

$$\Delta \bar{F}_{mix} = \Delta \bar{U}_{mix} - T\Delta \bar{S}_{mix} = kT[\frac{\Phi}{N_A}ln(\Phi) + \frac{1 - \Phi}{N_B}ln(1 - \Phi) + \chi\Phi(1 - \Phi)] \qquad (1.34)$$

The first and second terms have entropic origin and promote mixing in any case. For the last term, if $\chi < 0$ the two components are attracted one to another and we observe a single phase mixture at any composition of the blend. In the case of $\chi > 0$ there is a net repulsion between components. The evolution of the free energy of mixing in function of the composition allow to determinate the state of the system. If $\Delta \bar{F}_{mix}(\Phi)$ is convex the mixture is homogeneous. If $\Delta \bar{F}_{mix}(\Phi)$ is concave the following criterium determines the range of the miscibility gap:

$$(\frac{\partial \Delta \bar{F}_{mix}}{\partial \Phi})_{\Phi=\Phi'} = (\frac{\partial \Delta \bar{F}_{mix}}{\partial \Phi})_{\Phi=\Phi''} \qquad (1.35)$$

With Φ' and Φ'' are two distinct compositions of the mixture. By derivation of Eq.(1.34) with respect to the volume fraction of component A, we have:

$$\frac{\partial \Delta \bar{F}_{mix}}{\partial \Phi} = kT[\frac{ln\Phi}{N_A}\frac{1}{N_A} + \frac{ln(1-\Phi)}{N_B} - \frac{1}{N_B + \chi(1-2\Phi)}] \qquad (1.36)$$

In the simple case of a symmetric polymer blend with $N_A = N_B = N$:

$$(\frac{\partial \Delta \bar{F}_{mix}}{\partial \Phi})_{\Phi=\Phi'} = (\frac{\partial \Delta \bar{F}_{mix}}{\partial \Phi})_{\Phi=\Phi''}$$
$$= kT[\frac{ln(\Phi)}{N} + \frac{ln(1-\Phi)}{N} + \chi(1-2\Phi)] = 0 \qquad (1.37)$$

The coexistence curve, also called binodal denotes the condition at which two distinct phases may coexist. For a symmetric blend, the interaction parameter corresponding to the phase boundary can be written as:

$$\chi_b = \frac{ln(\Phi/(1-\Phi))}{(2\Phi - 1)N} \qquad (1.38)$$

In general, blends are asymmetric, and we can distinguish two different cases: $\frac{\partial^2 \Delta \bar{F}_{mix}}{\partial \Phi^2} > 0$ where the mixture is unstable, and $\frac{\partial^2 \Delta \bar{F}_{mix}}{\partial \Phi^2} < 0$ where the mixture is stable.

The spinodal curved is defined by

$$\frac{\partial^2 \Delta \bar{F}_{mix}}{\partial \Phi^2} = kT[\frac{1}{N_A\Phi} + \frac{1}{N_B(1-\Phi)} - 2\chi] = 0 \qquad (1.39)$$

$$\chi_S = \frac{1}{2}(\frac{1}{N_A\Phi} + \frac{1}{N_B(1-\Phi)}) \qquad (1.40)$$

This curve identified the boundary between unstable and metastable regions as can be oberved in Figure 1.5. The spinodal decomposition occurs because the mixture is locally unstable and any small composition fluctuation is enough to start the phase separation process.
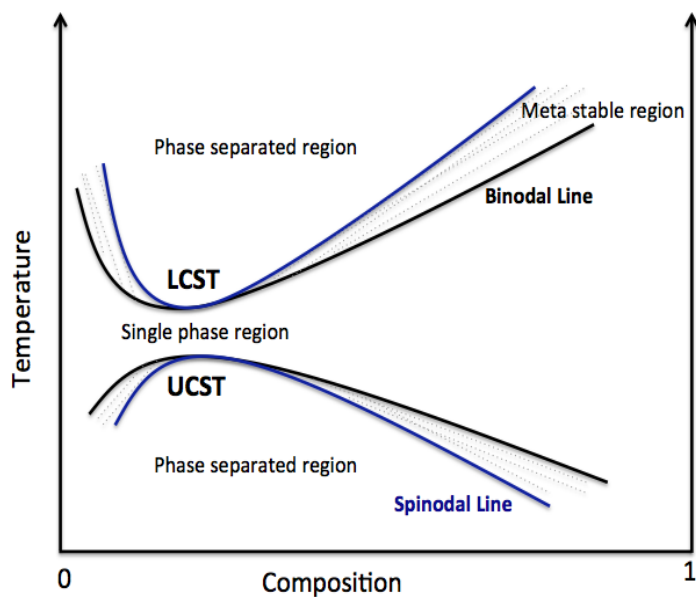
Figure 1.5: Illustration of a typical polymer phase behaviour including the Upper and Lower critical solution temperature scenario, namely UCST and LCST.

1.4 Modification of relaxation processes in polymers

A straight forward way of modifying the relaxation processes of a polymer is by direct modification of the polymer itself during the synthesis process. By this way, we can tuned the polymer microstructure which will directly influence his dynamic properties.

Another efficient way to obtain material with new properties is blending polymers. The blend is then made of the main polymer matrix and a second component. This second component can be a polymer of advantageous properties regarding the application or a plasticizer as it is the case in our study. This latter ones are made of oil or small molecules. The glass transition temperature of a polymer is generally strongly affected by adding a plasticizer. A plasticizer, as a small molecule, inserts itself in between the polymer chains and space them out from each other (See Scheme 1.6). This process increases the free volume. Thus the polymer chains can slide past each other more easily, and move around at different temperatures than they would without the plasticizer. This second component make possible to achieve improved compound processing characteristics, while also providing flexibility in the end-use product. However, it is also possible to use as "plasticizers" some amount of polymer chains of other type than those of the polymer matrix. In that case the used

word "plasticizer" might be not appropriate because depending of the type of polymer used as "plasticizer", the glass transition temperature of the polymer matrix can increase with respect to that of the initiate polymer. This kind of systems belongs to the category of two components miscible polymer blends.

Plasticizer

Main polymer chain
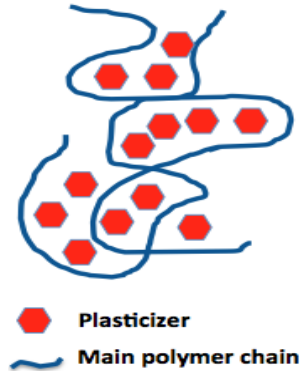
Figure 1.6: Illustration of "plasticizer" effect on a polymer matrix.

The segmental dynamic of blends such as poly(vinyl ethylene)/poly(isoprene), poly(vinyl methyl ether)/polystyrene, poly(ethylene oxide)/poly(methyl methacrylate) have been reported in the literature [34, 24]. The α-relaxation of the two components in the blend is strongly modified depending on both the composition and the interactions between the components, resulting in properties not observed in the pure components [20].

The main feature observed is the presence of two effective glass-transitions in polymer blends which was first attributed to the chain connectivity of each component, [40] although it has been shown that it is a more general phenomenon that occurs also in mixtures of smaller molecules. [16, 35] A main idea behind this concept is that the relevant cooperativity size at the glass-transition could be comparable to the repeating unit (or molecular) size. Thus, in a volume around a given component c the fraction occupied by units of this same component is larger than the average ('macroscopic') concentration (φ^c), giving rise to an effective concentration of this blend component φ^c_{eff} higher than the average one. This fact was captured with the concept of self-concentration (φ_s), [40] which allows connecting the effective and the macroscopic concentration as: $\varphi^c_{eff} = \varphi^c_s + (1 - \varphi^c_s)\varphi^c$. In this way, the effective glass-transition of a given blend component in the blend can be defined as: $T^c_{g,eff} = T_g(\varphi^c = \varphi^c_{eff})$, where $T_g(\varphi^c)$ refers to the above mentioned average-concentration dependent overall T_g.

The above commented ideas show that the complex dynamical behavior of polymer blends mainly arise from the combination of two major ingredients: i) thermal fluctuations of concentration and ii) inherent dynamic heterogeneity between the blend components. The fundamental investigations on the segmen-

tal dynamics of polymer blends giving rise to this conceptual framework have been developed by using experimental techniques that can provide selectivity to the individual blend components, such as dielectric spectroscopy (DS), [37] quasielastic neutron scattering (QENS), [51] and nuclear magnetic resonance (NMR), [30] among others.

1.5　General objectives of the present thesis

The aim of this work is to study the dynamics of a simplified industrial system, particularly a blend of styrene-butadiene rubber (SBR) with an oligomer of polystyrene (PS), in order to obtain detailed information about the segmental dynamics of both components in the blend. In this study we are mainly interested in two phenomenas, the rolling resistance and the adherence. By definition, the rolling resistance is the force resisting the motion when a body such as a tire rolls on a surface. The adherence refers to the combination of forces acting between two materials in close contact and preventing them from sliding against each other. Therefore, the ultimate goal of this work is the prediction of the mechanical behaviour of the studied system in the frequency ranges of the rolling resistance (10-10^2Hz) and the adherence domain (10^4-10^7Hz).

Mixtures of these polymers are good candidates to simultaneously fulfil the desired reduction of rolling resistance and increase of energy dissipation during braking. Using PS-oligomers, the high-T_g component acts as a "plasticizer". Varying the oligomer concentration allows tuning the average T_g of the system; also, miscibility is favored by using smaller macromolecules. In practice, it is observed that using these oligomers the wet grip performance is improved. On the other hand, from an academic point of view we note that it is not obvious *a priori* that theoretical frameworks developed and checked on canonical systems would also apply to the complex case of a mixture of a copolymer and an oligomer. In the next chapter, the material and the experimental techniques used in this study such as DSC, BDS, neutron scattering (both, quasielastic as well as elastic fixed window scan measurements, together with diffraction with polarization analysis) and the mechanical analysis instruments are presented.

24

Chapter 2

Material and experimental techniques

2.1 Material

In this part the pure components composing the blends as well as the blending preparation are presented.

2.1.1 Characteristic of the pure components

SBR polymer matrix

In this study we use a random copolymer of styrene and polybutadiene, Styrene Butadiene Rubber (SBR) as a main polymer matrix.

Styrene-butadiene rubbers (SBRs) were obtained from Michelin laboratory. [14] d_8-Styrene and d_6-butadiene deuterated monomers were supplied by Cortecnet (purity of 99%) and Eurisotop (purity of 99%), respectively. Before their use for copolymerization, the monomers were first dried over Butyllithium for d_6-butadiene and over calcium hydride and dibutyl magnesium for d_8-styrene and then distilled to obtain purifed monomers. To exploit neutron scattering selectivity, the use of samples where one of the components is deuterated is mandatory. Therefore similarly to hydrogenated SBR (hSBR) copolymers in classical runs, deuterated SBR (dSBR) copolymer samples were synthesized by anionic polymerization by the Michelin Company. The randomness of the copolymer has been checked by ^{1}H-NMR following the procedure described in the literature [60]. For the hSBR samples, we found that 99% of the styrene monomers are organized in short sequences of 1, 2 up to 3 following monomers, corresponding to a statistical repartition. For the deuterated sample, it was not possible to quantify the sequence distribution of styrene units. The very low amounts of protons of the deuterated sample are widely masked by the protons of the different antioxidants and impurities present in the sample. However, since a similar synthesis procedure has been followed for obtaining dSBR and hSBRs,

similar randomness is expected in both cases. The copolymerization was initiated by BuLi in methylcyclohexane at 50°C. Deuterated monomers were mixed in appropriate conditions to adjust microstructures of the hydrogenated chains synthesized. Indeed, as illustrated in Figure 2.1, the butadiene occurs as two isomers, the isomer 1,4 and the isomer 1,2 also called Vinyl. The 1,4 isomer occurs in configuration cis and trans.
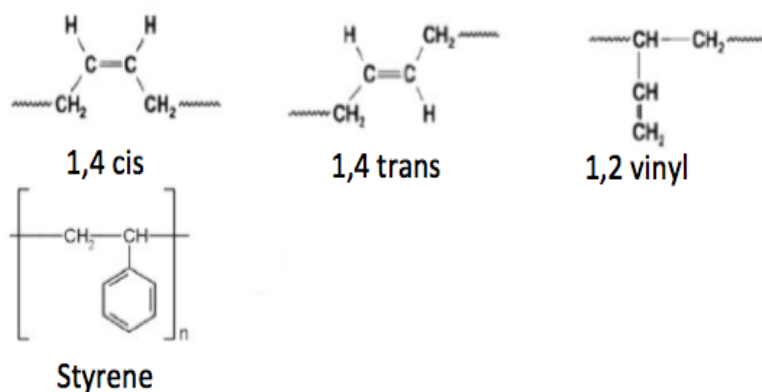
Figure 2.1: cis and trans configurations of the 1,4 butadiene isomer. The vinyl and styrene co-monomer are also represented.

Table 2.1 shows the microstructural composition, average molecular weight $(\overline{M}_n)$ and polydispersity values $(\overline{M}_w/\overline{M}_n)$ of the pure components used in this study.

As previously mentioned the random copolymers of styrene and polybutadiene provided by Michelin contains 0.25 wt % of antioxidants in order to prevent oxidative degradation. This degradation causes a loss of strength and flexibility of the material. Albeit these antioxidants contain strong dipolar moments they do not seem to influence the dielectric output due to the low amount used by Michelin.

Polystyrene

The protonated polystyrene (hPS1 and hPS2) and deuterated polystyrene (dPS) samples (purchased from Polymer Source) were synthesized by living anionic polymerisation of respectively styrene and styrene-d_8. Their physical properties are summarised in Table 2.1.

2.1.2 Blending preparation

Blends were prepared by solution casting using Tetrahydrofuran (THF) as a solvent with mass concentration of polystyrene from 10 wt % up to 70 wt %.

Table 2.1: Sample characteristics obtained by size exclusion chromatography (SEC) using THF as an eluent. The 1,2-butadiene (vinyl), 1,4-butadiene and styrene contents are given in mass %.

Sample	1,2 butadiene	1,4 butadiene	styrene	$\overline{M}_n$ (kg/mol)	$\overline{M}_w/\overline{M}_n$
hSBR1	18	54	28	101	1.04
hSBR2	33	47	20	22.8	1.03
dSBR	31	45	24	24.3	1.08
hPS1	-	-	100	0.99	1.12
hPS2	-	-	100	0.80	1.12
dPS	-	-	100	0.90	1.09

The obtained films were carefully dried under vacuum at 350K for 24h to remove the solvent completely. Reference samples of the neat polymers were prepared in a similar way.

2.1.3 Rubber vulcanization

As already mentioned in the previous chapter, vulcanization is a process in which individual polymer chains are converted into a three-dimensional network through chemical cross-linking. In order to allow the vulcanisation reaction to occur in an efficient way, the rubber is usually mixed with a series of ingredients in a process called compounding. The ingredients used for compounding for a tire in its final stage of production are classified into accelerators, activators, antioxidants, fillers and reinforcing agents, processing oils and vulcanizing agents. In this thesis, we studied a simplified industrial system, and we reduce the vulcanisation recipe as a cross-link agent (Sulphur) in 2.5 wt % and an accelerator (sulfenamides : CBS) in 2.5 wt % introduced in the sample solution using THF as solvent. After being dried under vacuum at 350K for 24h, samples are vulcanized in machine press for 60 minutes at 420K.

2.2 Experimental Techniques

2.2.1 Broadband dielectric Spectroscopy

In the past few years, polymeric materials have received a growing interest in the study of their dielectric properties. The used of Broadband dielectric Spectroscopy not only allows to analysed the sample in a broad frequency range but also make possible to isolate the dynamic of one of the component in the blend if the dielectric relaxation of one of the components is negligible.

Dielectric permittivity and relaxation phenomena

The interaction of electromagnetic fields with matters is described by Maxwell's equations

$$rot\mathbf{E} = -\frac{\partial \mathbf{B}}{\partial t} \tag{2.1}$$

$$rot\mathbf{H} = \mathbf{j} + \frac{\partial \mathbf{D}}{\partial t} \tag{2.2}$$

$$div\mathbf{D} = \rho_e \tag{2.3}$$

$$div\mathbf{B} = 0 \tag{2.4}$$

In this set of equations $\mathbf{E}$ and $\mathbf{H}$ describe the electric and magnetic field, $\mathbf{D}$ the electric displacement, $\mathbf{B}$ the magnetic induction, $\mathbf{j}$ the current density and ρ_e, the density of charges.

In a material, the electric displacement $\mathbf{D}$ can be written as

$$\mathbf{D} = \mathbf{P} + \varepsilon_0 \mathbf{E} \tag{2.5}$$

The polarization $\mathbf{P}$ describes the dielectric displacement which originates from the response of a material to an external field only. Hence it is defined in the linear regime as:

$$\mathbf{P} = (\varepsilon - 1) \times \varepsilon_0 \mathbf{E} \tag{2.6}$$

with ε_0 is the dielectric permittivity of vacuum and ε is the relative dielectric permittivity of the medium (> 1). This electric displacement comes from the vacuum $(\varepsilon_0 \mathbf{E})$ and also from the material. The contribution from the material is called polarization $\mathbf{P}$ and can be connected to the electric field by the following equation.

In the case of dielectric materials, the polarization comes from four main contributions.

Electronic polarization : Originates from the deformation of the electronic cloud due to the applied electric field.

Atomic polarization : Corresponds to the reorientation of the atoms nucleus in response to the electric field.

Dipole relaxation : Arises from the preferential orientation of the dipole in the direction of the electric field, in the case of a polar molecules.

Ionic relaxation : Mainly predominant at low frequency and is composed of interfacial, space charge relaxation and ionic conductivity.

If a stationary periodic disturbance $E(t) = E_0 exp(-i\omega t)$ is applied to the system where ω is the angular frequency with $\omega = 2\pi\nu$, with ν the ordinary frequency, the polarization can be then expressed as

$$\mathbf{P}(t) = \varepsilon_0(\varepsilon^*(\omega) - 1)\mathbf{E}(t) \tag{2.7}$$

where the $*$ symbol indicates a complex quantity reflecting the fact that $\mathbf{P}$ and $\mathbf{E}$ have in general different phases. With

$$\varepsilon^*(\omega) = \varepsilon^{'}(\omega) - i\varepsilon^{''}(\omega) \tag{2.8}$$

in which $\varepsilon^{'}(\omega)$ and $\varepsilon^{''}(\omega)$ are the real and the imaginary (loss) part of the dielectric permittivity. The real part of the permittivity is related to the stored energy in the sample, and the imaginary part, to the dissipation of energy within the medium.

The dielectric permittivity $\varepsilon^*(\omega)$ can be derived by measuring the impedance $Z^*(\omega)$ of a parallel plate capacitor, with vacuum capacitance C_0, filled with the material:

$$\varepsilon^*(\omega) = \frac{1}{i\omega Z^*(\omega)C_0} \tag{2.9}$$

The frequency and temperature dependence of the dielectric permittivity transfer specific features to $\varepsilon^{'}(\omega)$ and $\varepsilon^{''}(\omega)$. Thus the polymer dynamic properties can be investigated by studying $\varepsilon^*(\omega)$. As can be observed Figure 2.2 in a typical relaxation process, the real part of the permittivity shows a step-like decrease with increasing frequency and the imaginary part shows a peak. In general, the frequency ω_{max} of the maximum of the peak of $\varepsilon^{''}(\omega)$ is related to the characteristic relaxation time $\tau_{max} = 1/\omega_{max}$ of the fluctuating dipoles.

Phenomenological models of dielectric relaxation

Different model functions are available in order to describe these dynamic processes. The Debye relaxation represents the simplest case of the dielectric relaxation response. This is the model of non-interacting dipoles subjected to friction, in a typical relaxation processes for example the relaxation time τ_D is often referred to as Debye time. Within an alternating external electric field, the dielectric permittivity in this model is expressed by :

$$\varepsilon^*(\omega) = \varepsilon_\infty + \frac{\Delta\varepsilon}{1 + (i\omega\tau_D)} \tag{2.10}$$
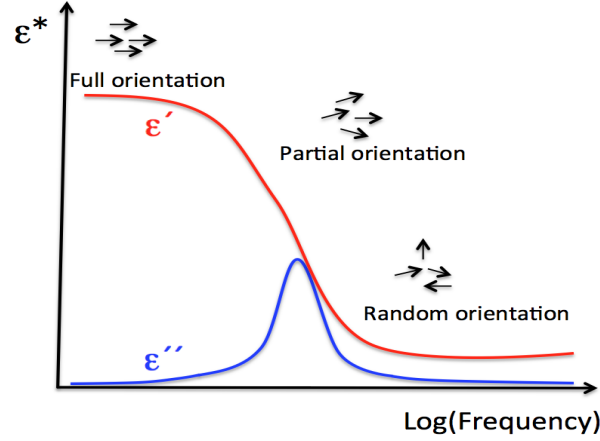
Figure 2.2: Evolution of the dielectric permittivity in function of the frequency.

where $\Delta\varepsilon = \varepsilon_s - \varepsilon_\infty$ is the dielectric strength with $\varepsilon_\infty = \lim_{t,\omega\to 0}\varepsilon$ and $\varepsilon_s = \lim_{t,\omega\to\infty}\varepsilon = \varepsilon_\infty + \Delta\epsilon$ the high and low frequency limiting values of the dielectric permittivity.

This theory fails in the description of the relaxation behaviour of most of the materials since the actual relaxations show significantly broader loss peaks in the frequency response. One can solve this problem by modifying the Debye equation introducing some phenomenological shape parameters. The Cole-Cole function is defined as [23]

$$\varepsilon^*(\omega) = \varepsilon_\infty + \frac{\Delta\varepsilon}{1 + (i\omega\tau_{CC})^\gamma}. \tag{2.11}$$

where γ is comprised in the range between 0 and 1 and leads to a symmetrical broadening. When $\gamma = 1$ the Debye function is obtained.

A more general model function was introduced by Havriliak and Negami (HN) [37]

$$\varepsilon^*_{HN}(\omega) = \varepsilon_\infty + \frac{\Delta\varepsilon}{(1 + (i\omega\tau_{HN})^\alpha)^\gamma}. \tag{2.12}$$

The fractional shape parameters α and γ describe the symmetric and asymmetric broadening of the complex dielectric function, and the condition $0 < \gamma$, $\alpha.\gamma \leq 1$ holds.

The frequency ω_{max} of the maximal loss depends on τ_{HN} and on the parameters α and γ according to [37]

$$\frac{1}{\omega_{max}} \equiv \tau_{max} = \tau_{HN}\frac{[\sin(\frac{\alpha\gamma\pi}{2+2\gamma})]^{\frac{1}{\alpha}}}{[\sin(\frac{\alpha\pi}{2+2\gamma})]^{\frac{1}{\alpha}}} \tag{2.13}$$

In the time domain the non-Debye pattern is usually described by the empirical Kohlraush-Williams-Watts (KWW) function in the following way

$$\varepsilon(t) = \varepsilon_\infty + \Delta\varepsilon[1 - exp((-\frac{1}{\tau_{KWW}})^{\beta_{KWW}})] \tag{2.14}$$

The HN-function under certain constrains corresponds approximately to the Kohlrausch-Wlliams-Watts (KWW) relaxation function [5]. In these cases there is a link between the KWW shape parameter (β) and the HN ones given by: [4]

$$\alpha\gamma = \beta^{1.23}. \tag{2.15}$$

Moreover, the KWW relaxation time is connected with the HN one as: [4]

$$\log\left[\frac{\tau_{HN}}{\tau_{KWW}}\right] = 2.6(1 - \beta)^{0.5} \exp(-3\beta) \tag{2.16}$$

Finally, the best correspondence between the HN and KWW descriptions can be found if the following relation between the HN parameters holds:

$$\gamma \approx 1 - 0.8121 * (1 - \alpha)^{0.387} \tag{2.17}$$

Dielectric Spectroscopy instruments

All the dielectric measurements were performed at the Material Physics Center (CFM) in San Sebastián. The dielectric permittivity $\varepsilon^*(\omega)$ was measured in the frequency range $10^{-2} - 10^6 Hz$ using the broadband dielectric spectrometer *Novocontrol, Alpha*. A general scheme of the device can be observed in Figure 2.3. To improve accuracy for low losses detection, this system compares the measure sample capacitance with that determined in the same conditions for a reference standard of negligible loss. However in the higher frequency range of $10^6 - 10^9 Hz$ an Agilent rf impedance analyser 4192B was used. In this frequency range the coaxial line at the end of which the sample is placed has to be previously characterized by a calibration procedure using well defined standards. In addition a cell calibration is required to account for the effects not directly related to the impedance of the sample capacitor.

To perform the broadband frequency dielectric measurements, samples were placed directly between two gold-plated electrodes, with diameters of 20 and 30 mm for the upper and lower electrodes respectively forming a parallel plate capacitor. A thin cross- shaped spacer of 0.1 mm thick made of Teflon was placed between the electrodes before compressing the sample to avoid short circuit (see Figure 2.4). For the high frequency dielectric measurements (see Figure 2.5), the capacitor was prepared in the same way, with the only difference in the gold-plated electrodes size, both with a diameter of 10 mm. For both frequency range measurements, samples were placed in their respective sample holders, and the measured temperature range was 130-420K. Data were recorded every 5 K. Samples temperature was controlled by a nitrogen gas flow with stability better than 0.1 K by Quatro cryosystem (Novocontrol).

31
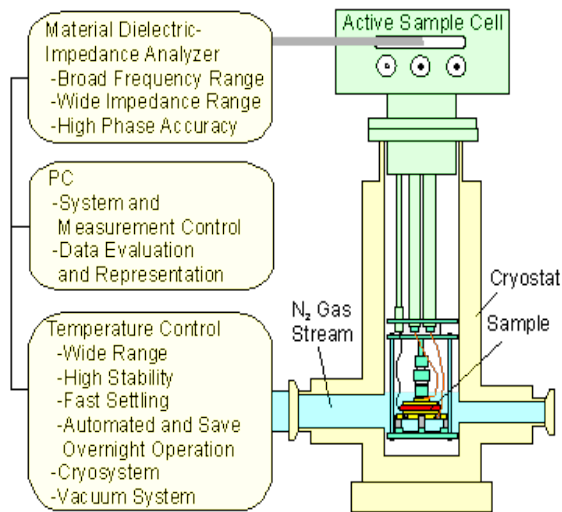
Figure 2.3: Principle setup of a dielectric spectrometer.
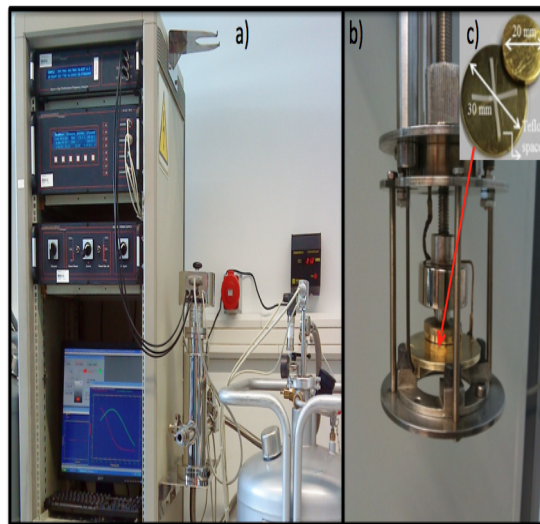
Figure 2.4: a) General perspective of the Novocontrol Alpha analyzer and the nitrogen deware for temperature control. b) Sample cell container. c) Teflon spacers and gold-plated electrodes.

2.2.2 Neutron Scattering

When the neutrons are scattered by atoms in the sample being investigated, their directions change, depending on the atoms relative positions. These scat-
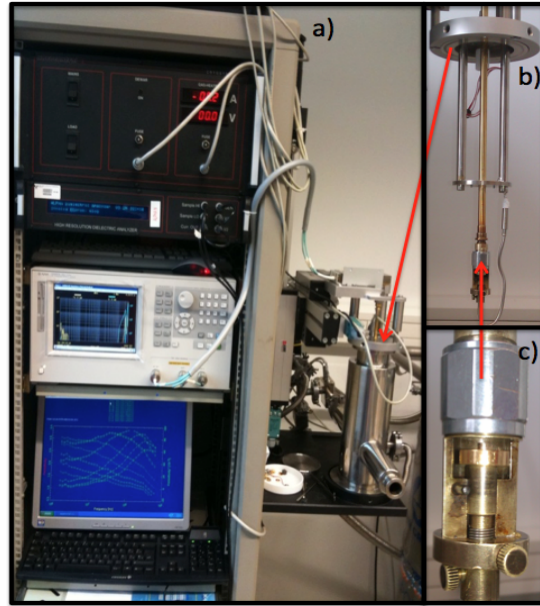
Figure 2.5: General perspective of the Agilent RF impedance Analyzer 4192B.

tering events show how the atoms are arranged in relation to each other which reveal the structure of the sample. The changes in the neutrons velocity give information on the atoms individual and collective oscillations, revealing their dynamic behaviour. "In simple terms neutrons helped answer the question of where atoms *are* and what atoms *do*".

Basic properties of Neutrons

A neutron is a subatomic particle characterised by the following physical properties:

-mass $m = 1.675 \times 10^{-27} Kg$,

-magnetic moment $\eta = -1.913 \ \mu_N$ in which $\mu_N = e\hbar/2m_p$

- spin $1/2$ and zero charge.

These properties make the interactions short-ranged nuclear and magnetic, thus the probability for a neutron to be scattered by matter is small and can be described in terms of the first Born approximation. The neutrons usually penetrate into the bulk without distorting the intrinsic properties of the sample and their magnetic moment makes the neutrons suitable atomistic magnetic probes.[48],[42],[32],[57],[13]

33

Differential cross-section

In a neutron scattering experiment, the magnitude measured is proportional to the double differential cross section. The probability that a neutron, with incident energy E_0, leaves the sample in the solid angle element $d\Omega$ around Ω and with energy exchange comprised between $\hbar\omega = E - E_0$ and $\hbar(\omega + d\omega)$ can be written as:

$$\frac{\partial^2\sigma}{\partial\Omega\partial\omega} = \frac{C}{\eta\Phi N\Delta\Omega\Delta\omega} \tag{2.18}$$

C is the count rate in the detector with efficiency η and N is the number of atoms in the sample. Φ is the flux of incident neutrons. Measuring the double differential cross section for all the energy transfers E lead to the *the differential cross section*:

$$\frac{\partial\sigma}{\partial\Omega} = \int dE \frac{\partial^2\sigma}{\partial\Omega\partial E} \tag{2.19}$$

Considering neutrons scattered by a sample undergoing a change from a state λ_0 to a state λ while the state of the neutron changes from $(\mathbf{k}_0, \sigma_0)$ to $(\mathbf{k}, \sigma)$, the corresponding cross section is given by :

$$\frac{\partial}{\partial\Omega} = \frac{1}{N\Phi d\Omega} W_{\mathbf{k}_0,\sigma_0,\lambda_0 \to \mathbf{k},\sigma,\lambda} \tag{2.20}$$

where $W_{\mathbf{k}_0,\sigma_0,\lambda_0 \to \mathbf{k},\sigma,\lambda}$ is the number of transitions per second from the state $\mathbf{k}_0, \sigma_0, \lambda_0$ to the state $\mathbf{k}, \sigma, \lambda$.

The latter equation can be reevaluated by using the Fermi's golden rule:

$$W_{\mathbf{k}_0,\sigma_0,\lambda_0 \to \mathbf{k}_1,\sigma_1,\lambda_1} = \frac{2\pi}{\hbar}|\langle\mathbf{k}_1,\sigma_1,\lambda_1|V|\mathbf{k}_0,\sigma_0,\lambda_0\rangle|^2\rho_{\mathbf{k}_1,\sigma_1(E_1)} \tag{2.21}$$

where V is the interaction potential between the incident neutron and the target sample that causes the transition, and $\rho_{\mathbf{k}_1}$ is the density of the final scattering states per unit energy range. To evaluate $\rho_{\mathbf{k}_1}$, we consider a large box of volume L^3 and the initial and final state of the neutrons are expressed by:

$$\psi_{\mathbf{k}_0}(\mathbf{r}) = \frac{1}{L^{3/2}}e^{(i\mathbf{k}_0.\mathbf{r})} \tag{2.22}$$

and

$$\psi_{\mathbf{k}}(\mathbf{r}) = \frac{1}{L^{3/2}}e^{(i\mathbf{k}.\mathbf{r})} \tag{2.23}$$

Periodic boundary conditions are applied in order to have plane waves solution:

$$\psi_{\mathbf{k}}(\mathbf{r} + \mathbf{L}_\alpha) = \psi_{\mathbf{k}}(\mathbf{r}) \tag{2.24}$$

where $\mathbf{L}_\alpha$ is any of the edge vectors of the cubic box. Thus the wave-vector can be written as

$$\mathbf{k} = \frac{2\pi}{L^2}(m\mathbf{L}_x + n\mathbf{L}_y + p\mathbf{L}_z) \tag{2.25}$$

with m, n, p integers. In the momentum space $d\mathbf{k} = k^2 d\mathbf{\Omega} dk$, therefore each extremity of a moment vector occupies a volume equal to $(2\pi/L)^3$ in the reciprocal space and the density of final stated is such that:

$$\rho(\mathbf{k})d\mathbf{k} = (\frac{L}{2\pi})^3 k^2 d\mathbf{\Omega} dk \tag{2.26}$$

Changing to energy space, considering $E = \hbar^2 k^2/2m$ we obtain

$$\rho(\mathbf{E})dE = (\frac{L}{2\pi})^3 \frac{mk^2}{\hbar^2} d\mathbf{\Omega} dE \tag{2.27}$$

Then, integrating over the energy, the equation for the density of the final scattering states per unit energy range :

$$\rho(\mathbf{E}) = (\frac{L}{2\pi})^3 \frac{mk^2}{\hbar^2} d\mathbf{\Omega} \tag{2.28}$$

The De Broglie relation $p = \hbar k$ allows to write the incident flux of neutrons such as:

$$\Upsilon = \frac{v}{L^3} = \frac{1}{L^3}\frac{\hbar k_0}{m} \tag{2.29}$$

Which leads to the cross section:

$$\frac{\partial\sigma}{\partial\mathbf{\Omega}} = \frac{1}{N}\frac{k}{k_0}(\frac{m}{2\pi\hbar})^2 |\langle \mathbf{k}\lambda\sigma|V|\mathbf{k}_0\lambda_0\sigma_0\rangle|^2 \tag{2.30}$$

Finally incorporating the energy conservation $\hbar\omega = E - E_0$, the double differential cross-section is given by:

$$\frac{\partial\sigma}{\partial\mathbf{\Omega}\partial E} = \frac{1}{N}\frac{k}{k_0}(\frac{m}{2\pi\hbar})^2 |\langle \mathbf{k}\lambda\sigma|V|\mathbf{k}_0\lambda_0\sigma_0\rangle|^2 \partial(\hbar\omega + E - E_0) \tag{2.31}$$

The neutron-nucleus scattering is isotropic and can be fully characterised by the scattering length b. Thus, the interaction potential between the sample and the neutrons can be described by the Fermi pseudo-potential:

$$V(\mathbf{r}) = \frac{2\pi\hbar}{m}\sum_i b_i\delta(\mathbf{r} - \mathbf{R}_i) \tag{2.32}$$

With b_i and $\mathbf{R}_i$ respectively the scattering length and the vector position of the i-th nucleus.

$$|\langle \mathbf{k}|V|\mathbf{k}_0\rangle| = \sum_i b_i \int d\mathbf{r} \, exp(-i\mathbf{k}.\mathbf{r}) \, \delta(\mathbf{r} - \mathbf{R}_i) \, exp(-i\mathbf{k}_0.\mathbf{r})$$

$$= \sum_i b_i \, exp(i\mathbf{Q} \cdot \mathbf{R}_i) \qquad (2.33)$$

with $\mathbf{Q} = \mathbf{k} - \mathbf{k}_0$.

In the simple case of an unpolarized neutron scattering experiment, *the master formula*: can be expressed as:

$$\frac{\partial\sigma}{\partial\mathbf{\Omega}\partial E} = \frac{1}{N}\frac{k}{k_0} \sum_{\lambda_0} p_{\lambda_0} \sum_{\lambda} \left| \left\langle \lambda| \sum_i b_i \, exp(-i\mathbf{Q}\mathbf{R}_i)|\lambda_0 \right\rangle \right|^2 \partial(\hbar\omega + E - E_0)$$

$$(2.34)$$

p_{λ_0} is the probability to find the sample in the initial state λ_0. In a real experiment, the intensity measured is not the double differential cross section for a process in which the sample goes from a specific state to another thus, it is necessary to sum over all the final states λ, keeping λ_0 fixed, and then average over all the initial states. To do so the *Heisenberg* operators and a representation of the delta *Dirac* function by an integral over time are used which leads to the real-time representation of the double differential cross section:

$$\frac{\partial\sigma}{\partial\mathbf{\Omega}\partial E} = \frac{1}{N}\frac{k}{k_0} \int_{-\infty}^{+\infty} exp(-i\omega t)dt \sum_{i,j} b_i^* b_j \left\langle exp(i\mathbf{Q}(\mathbf{R}_i(t) - \mathbf{R}_j(t))) \right\rangle \quad (2.35)$$

Coherent and Incoherent Scattering

The simple case of a system of N chemically identical particles is considered. Because b also depends on the combined spin state of the scattered neutron and the scattering nucleus even in such simplify system b may vary. The nuclear spins and the isotopes are randomly distributed in any atomic configurations and $\bar{b}_i$ is the average scattering length for a given atomic species.

$$\sum_{i,j} b_i^* b_j \, exp[i\mathbf{Q}(\mathbf{R}_i(t) - \mathbf{R}_j(0)] = \sum_{i,j} (\bar{b}_i^* \bar{b}_j + b_i^* b_j - \bar{b}_i^* \bar{b}_j) \, exp[i\mathbf{Q}(\mathbf{R}_i(t) - \mathbf{R}_j(0)]$$

$$= \sum_{i,j} \bar{b}_i^* \bar{b}_j \, exp[i\mathbf{Q}(\mathbf{R}_i(t) - \mathbf{R}_j(0)] + \sum_{i,j} (b_i^* b_j - \bar{b}_i^* \bar{b}_j) \, exp[i\mathbf{Q}(\mathbf{R}_i(t) - \mathbf{R}_j(0)]$$

$$(2.36)$$

We consider the sample to be an ensemble of a large number of independent subsamples and thus the cross-section will be an average over all these subsamples. Since under ordinary conditions isotopes and nuclear spins are fully randomly distributed in the sample, there is no correlation between the occupation i and j. Therefore, if $i \neq j$

$$\left\langle b_i^* b_j - \bar{b}_i^* \bar{b}_j \right\rangle = \left\langle b_i^* \right\rangle \left\langle b_j \right\rangle - \bar{b}_i^* \bar{b}_j \equiv 0 \tag{2.37}$$

while for $i = j$

$$\left\langle b_i^* b_j - \bar{b}_i^* \bar{b}_i \right\rangle = \left\langle b_i^* \right\rangle \left\langle b_i \right\rangle - \bar{b}_i^* \bar{b}_i = (b_i^{inc})^2 \tag{2.38}$$

with

$$b_i^{inc} = \sqrt{\left\langle b_i^2 \right\rangle - \bar{b}_i^2} \tag{2.39}$$

called incoherent scattering length. From the previous equation:

$$
\begin{aligned}
\frac{\partial \sigma}{\partial \Omega \delta E} &= \frac{1}{N} \frac{k}{k_0} \int exp[-i\omega t] dt (\sum_{i,j} \left\langle \bar{b}_i^* \bar{b}_j \right\rangle \; exp[i\mathbf{Q}(\mathbf{R}_i(0) - \mathbf{R}_j(t)] \\
&\qquad + \sum_{i,j} \left\langle b_i^* b_j - \bar{b}_i^* \bar{b}_j \right\rangle \; exp[i\mathbf{Q}(\mathbf{R}_i(0) - \mathbf{R}_j(t)] \\
&= \frac{1}{N} \frac{k}{k_0} \int exp[-i\omega t] dt (\sum_{i,j} \left\langle \bar{b}_i^* \bar{b}_j \right\rangle \; exp[i\mathbf{Q}(\mathbf{R}_i(0) - \mathbf{R}_j(t)] \\
&\qquad + \sum_{i,j} \left\langle (b_i^{inc})^2 \right\rangle \; exp[i\mathbf{Q}(\mathbf{R}_i(0) - \mathbf{R}_i(t)]
\end{aligned}
\tag{2.40}
$$

In the previous equation the first sum in the right side represents the *coherent* double differential cross section and depends on the correlation between the position of the atom i at time 0 with an atom j at time t, while the second sum represents the *incoherent* double differential cross-section which depends on the correlation between the position of the same *atom i* at different times. Defining the *coherent dynamic structure factor* and the *incoherent dynamic structure factor* as:

$$S(\mathbf{Q}, \omega) = \sum \int exp[-i\omega t] dt \; exp[i\mathbf{Q}(\mathbf{R}_i(0) - \mathbf{R}_j(t)] \tag{2.41}$$

$$S_{inc}(\mathbf{Q}, \omega) = \sum_i \int exp[-i\omega t] dt \; exp[i\mathbf{Q}(\mathbf{R}_i(0) - \mathbf{R}_i(t)] \tag{2.42}$$

and the **coherent cross-section** and the **incoherent cross-section** can be then written as:

$$\sigma_{coh} = 4\pi \left\langle b \right\rangle^2 \tag{2.43}$$

$$\sigma_{inc} = 4\pi (\left\langle b^2 \right\rangle - \left\langle b \right\rangle^2) \tag{2.44}$$

Finally the double differential cross section as combination of a coherent and incoherent part is:

$$\frac{\partial \sigma}{\partial \Omega \partial E} = (\frac{\partial \sigma}{\partial \Omega \partial E})_{coh} + (\frac{\partial \sigma}{\partial \Omega \partial E})_{inc} \qquad (2.45)$$

with

$$(\frac{\partial \sigma}{\partial \Omega \partial E})_{coh} = \frac{1}{N} \frac{k}{k_0} \frac{\sigma_{coh}}{4\pi} \, S(\mathbf{Q}, \omega) \qquad (2.46)$$

and

$$(\frac{\partial \sigma}{\partial \Omega \partial E})_{inc} = \frac{1}{N} \frac{k}{k_0} \frac{\sigma_{inc}}{4\pi} \, S_{inc}(\mathbf{Q}, \omega) \qquad (2.47)$$

The cross-sections in the previous equations are factorized in three independent parts: The ratio of the wave numbers k and k_0 reflect the scattering process. The total scattering cross-section σ depends on the composition of the sample and finally, the *dynamic structure factor* $S(\mathbf{Q}, \omega)$ and the incoherent scattering function $S_{inc}(\mathbf{Q}, \omega)$. $S(\mathbf{Q}, \omega)$ characterize the structural and dynamical properties of the scattering sample. $S_{inc}(\mathbf{Q}, \omega)$ provides information on self-atomic motions.

Correlation Functions

We can define the dynamic structure factor $S(\mathbf{Q}, \omega)$ as the time-Fourier transform of the *intermediate scattering function* $I(\mathbf{Q}, t)$

$$S(\mathbf{Q}, \omega) = \frac{1}{2\pi} \int_{-\infty}^{+\infty} I(\mathbf{Q}, t) exp(-i\omega t) dt \qquad (2.48)$$

$$S_{inc}(\mathbf{Q}, \omega) = \frac{1}{2\pi} \int_{-\infty}^{+\infty} I_{inc}(\mathbf{Q}, t) exp(-i\omega t) dt \qquad (2.49)$$

with

$$I(\mathbf{Q}, t) = \frac{1}{N} \sum_{i,j} \langle exp[i\mathbf{Q} \cdot \mathbf{R}_i(t)] \, exp[-i\mathbf{Q} \cdot \mathbf{R}_j(0)] \rangle \qquad (2.50)$$

$$I_{inc}(\mathbf{Q}, t) = \frac{1}{N} \sum_{i} \langle exp[i\mathbf{Q} \cdot \mathbf{R}_i(t)] \, exp[-i\mathbf{Q} \cdot \mathbf{R}_i(0)] \rangle \qquad (2.51)$$

We can also obtain the *space-time correlation function* and the *self space-time correlation function*, also called *Van Hove correlation functions* by the Fourier transform in space of the previous equations:

$$G(\mathbf{r}, t) = \frac{1}{(2\pi)^3} \int d\mathbf{Q} \, exp(-i\mathbf{Q}\mathbf{r}) I(\mathbf{Q}, t) \qquad (2.52)$$

$$G_s(\mathbf{r}, t) = \frac{1}{(2\pi)^3} \int d\mathbf{Q} \, exp(-i\mathbf{Q}\mathbf{r}) I_{inc}(\mathbf{Q}, t) \qquad (2.53)$$

Introducing the definition of intermediate scattering function we can write the Van Hove correlation function under the form of a pair-correlation function:

$$G(\mathbf{r}, t) = \frac{1}{(2\pi)^3} \sum_{i,j} \langle \delta(\mathbf{r} - \mathbf{r}' + \mathbf{R}_i(0)) \delta(\mathbf{r}' - \mathbf{R}_j(t)) \rangle \, d\mathbf{r}' \qquad (2.54)$$

Now, if we define the microscopic particle density operator can be defined as:

$$\rho(\mathbf{r}, t) = \sum_i \delta(\mathbf{r} - \mathbf{R}_i(t)) \qquad (2.55)$$

Thus the pair correlation function can be written as:

$$G(\mathbf{r}, t) = \frac{1}{N} \int \langle \rho(\mathbf{r}' - \mathbf{r}, 0) \rho(\mathbf{r}', t) \rangle \, d\mathbf{r} \qquad (2.56)$$

with the condition of normalization

$$\int G(\mathbf{r}, t) d\mathbf{r} = N \qquad (2.57)$$

Introducing the Fourrier components $\rho_k(t)$ of the particle density

$$\rho(r, t) = \frac{1}{(2\pi)^3} \int \rho_k(t) exp(i\mathbf{K} \cdot \mathbf{r}) d\mathbf{K} \qquad (2.58)$$

Thus the intermediate scattering function can be written as:

$$I((Q), t) = \frac{1}{N} \langle \rho_{\mathbf{Q}}(0) \rho_{-\mathbf{Q}}(t) \rangle \qquad (2.59)$$

In terms of the density-density correlation function, the interaction potential couples the neutron to the density of the target system and $S(\mathbf{Q}, \omega)$ is therefore determined by spontaneous density fluctuations in the sample, giving information on its structure and its dynamic. Moreover, under the approximation $(|\hbar\omega| \ll k_B T)$ the space-time correlation function can be written as:

$$G^{cl}(\mathbf{r}, t) = \frac{1}{N} \sum_{i,j} \langle \delta(\mathbf{r} - \mathbf{R}_j(t) + \mathbf{R}_i(0)) \rangle$$
$$\qquad (2.60)$$
$$G_s^{cl}(\mathbf{r}, t) = \frac{1}{N} \sum_i \langle \delta(\mathbf{r} - \mathbf{R}_i(t) + \mathbf{R}_i(0)) \rangle$$

The probability that a given particle i in the origin at time $t = 0$, any particle j, or only the same particle i in the self case, is in the volume $d\mathbf{r}$ around position $\mathbf{r}$ at time t are $G^{cl}(\mathbf{r}, t)d\mathbf{r}$ and $G_s^{cl}(\mathbf{r}, t)d\mathbf{r}$. There are two special cases of the Van Hove correlation functions that results to be of particular interest. At $t = 0$ we have:

$$G(\mathbf{r}, t = 0) = \delta(\mathbf{r})$$
$$G_s(\mathbf{r}, t = 0) = \delta(\mathbf{r}) + g(\mathbf{r})$$

(2.61)

The instantaneous pair correlation function namely $g(\mathbf{r})$ is accessible through diffraction experiments. By using the previous equations:

$$S(\mathbf{Q}) = 1 + \int_{-\infty}^{+\infty} S(\mathbf{Q}, \omega)d\omega = \int_{-\infty}^{+\infty} g(\mathbf{r}) exp[i\mathbf{Q}\mathbf{r}]d\mathbf{r} = I(\mathbf{Q}, t = 0) \quad (2.62)$$

The elastic incoherent structure factor

We consider an atom diffusing in a space which is very large as compared to the inter-atomic distances, the self-correlation function $G_s(\mathbf{r}, t)$ vanishes for $t \to \infty$, however if the atom is bound to a finite volume $G_s(\mathbf{r}, \infty)$ approaches a finite value with r varying in the volume. The self-concentration function can be decompose in two components: its asymptotic value in the infinite time limit and time-dependent term $G_s^{'}(\mathbf{r}, t)$:

$$S_{inc}(\mathbf{Q}, \omega) = \frac{1}{2\pi} \int_{-\infty}^{+\infty} \int_{-\infty}^{+\infty} exp[i(\mathbf{Q}\mathbf{r} - \omega t](G_s(\mathbf{r}, \infty) + G_s^{'}(\mathbf{r}, t))d\mathbf{r}dt \quad (2.63)$$

leading to

$$S_{inc}(\mathbf{Q}, \omega) = S_{inc}^{el}(\mathbf{Q})\delta(\omega) + S_{inc}^{in}(\mathbf{Q}, \omega) \quad (2.64)$$

Therefore, the incoherent scattering function has been decomposed into a purely elastic line, $S_{inc}^{el}(\mathbf{Q})\delta(\omega)$, and an inelastic component, $S_{inc}^{in}(\mathbf{Q}, \omega)$. The concept of the *elastic incoherent stucture factor* (EISF) provides a method that permits to extract geometrical information on localized single-particle motions by the determination of the elastic fraction of the measured spectra intensity. Moreover, selecting the appropriate instrumental energy resolution and under the condition that the motion is sufficiently well separated on the energy-scale from slower motions of the same atom, it is possible to isolate the EISF of a specific component.

Summarizing, while the incoherent scattering provides informations on the motions of a single particle, the coherent scattering relates the positions and motions of different particle in the system. It is possible to gain from this latter one information on the structure of the sample through the pair correlation function and the static structure factor. The dynamic structure factor account for the collective dynamics in the sample.

Neutrons: A suitable probe for soft matter

The use of thermal neutrons is a powerful way to investigate condensed matter. In fact they are characterized by energies of the same order of the energies of

Table 2.2: Scattering lengths and cross sections of SBR and PS atoms.

Element	$b_{coh}(fm)$	$b_{inc}(fm)$	$\sigma_{coh}(10^{-24}\text{cm}^2)$	$\sigma_{inc}(10^{-24}\text{cm}^2)$
H	-3.7409	25.274	1.76	80.26
D	6.674	4.04	5.59	2.05
C	6.6484	0	5.551	0.001

excitations in soft matter and their wavelength are comparable with the usual molecular dimension or with the intermolecular space. Since the interaction is nuclear, each isotope has a different scattering amplitude. Therefore, the amplitude of scattering that characterizes the interaction of a neutron with a given isotope is the scattering length b. The scattering length is a proper characteristic of the isotopes and varies randomly through the periodic table (see Table 2.2). The best advantage of neutron scattering for investigating soft matters is thus represented by the possibility of isotopic substitution, which allows to measure partial structure factors. Due to the very different scattering length of Hydrogen and Deuterium it is possible to label a single part of a macromolecules and selectively investigate its dynamics or label an entire molecule and study it, in contrast with the environment. Due to the high value of Hydrogen incoherent cross section, the experiments carried out on a protonated sample lead to informations on the single particle motion of hydrogens, while deuterated samples are needed to investigate the collective dynamics.

Neutron sources

The free neutron has a mean lifetime of about 900s, therefore it is necessary to produce the free neutrons continuously as the experiment is running. Nowadays, free neutrons for scientific research are produced by nuclear reactions mainly in fission reactor or spallation sources. The typical features of a neutron beam such as the energy or the time structure of the flux are determinant parameters in order to choose the optimal set up for a given experiment. There characteristics are determined by the kind of neutron source and by the thermic moderator used. As reported in Table 2.3 the different energy ranges of neutrons are classified according to the the moderator temperature as ultra-cold, cold, thermal and epithermal.

Neutrons produced by nuclear fission

In order to produce neutrons by nuclear fission, a low energy thermal neutron is captured by a fissile heavy isotope such as Uranium-235. The splitting uranium isotope gives rise to 2-3 high energy neutrons, lighter elements and a release of energy. One neutron per fission is necessary to assure the continuity of the chain reaction. This neutron is slowed down by the heavy water tank and scattered back into the fuel element. Finally 1-2 neutrons are available for carrying out the scientific experiment.

Neutrons produced by spallation

Another way to release neutrons from nucleus is via spallation reactions. High energy protons are accelerated and then hit a target made of a material

Table 2.3: Typical energy, velocity and wavelength range for the four type of sources in a reactor.

	Ultra-cold	Cold	Thermal	Epithermal
Energy	< 300 neV	300 nev - 12 meV	12 meV-100 meV	100 meV- 1eV
Velocity (m/s)	< 8	7.5- 1515	1515-4374	4374 - 13800
Wavelength ($\dot{A}$)	> 500	52.2 - 2.6	2.6 - 0.9	0.9 - 0.28

rich in neutrons. The De Broglie wavelength $\lambda = \sqrt{\frac{h^2}{2mE}}$ is so short that the protons does not interact with the nucleus as the whole but with the singles nucleons. The kicked nucleon can generate an inter-nuclear cascade. However the nucleus is still in an highly excited state and the energy is released by evaporation of particles including neutrons. A spallation source with a heavy nuclei target composed of mercury or tantalum can generally produces between 20 and 30 pulsed or quasi-continuous neutrons.

Neutron scattering instruments

Time-of-Flight spectrometer

Neutron time-of-flight spectrometer allows to determine the kinetic energy of a travelling neutron by measuring the time necessary to fly a known distance. The monochromatization of the incoming neutron beam can either be done by Bragg reflection from a crystal or by phased choppers selecting a single wavelength only. The latter technique is more flexible for the selection of the incident energy. A further chopper defines the starting flying time of the neutrons and their registration when they hit the detector gives the end of their flight through the spectrometer. From the time difference, one can obtained the velocity of the neutrons which lead to the energy transfer, namely $\bar{h}\omega$, which can be expressed as:

$$\bar{h}\omega = \left(\frac{l_1^2}{(l_0 - \sqrt{E/m_n}t_{flight})^2} - 1\right)E \tag{2.65}$$

where l_1 is the distance between the chopper and the sample, l_0 is the distance between the sample and the detector, E is the incident energy, m_n the neutron mass, and t_{flight} is the time it takes to a neutron to arrive to the detector. Depending on the desired incident wavelength, the instruments are constructed either using thermal neutrons or cold neutrons. Thermal neutrons make a larger Q range accessible while cold neutron yield better energy resolution. TOFTOF, the instrument used in this study, is a direct geometry multi-chopper time-of-flight spectrometer operated with cold incident neutrons located at the Heinz Maier-Leibnitz Zentrum (MLZ) in Garching, Germany. In contrast to the inverse time of flight spectrometer operating in spallation sources, in this kind of instrument only a few percent of the produced neutrons can be used although a larger Q-range is accessible. With this instrument, an excellent signal-to-background ratio can be achieved. Seven fast rotating choppers which are housed in four chopper vessels are used to prepare a monochromatic pulsed beam. This latter is focussed onto the sample by a converging super-mirror section. The scattered neutrons are detected by 1000 detector tubes with a time resolution up to 50 ns. The high rotation speed of the chopper system which can be up to 22 000 rpm, together with a high neutron flux allows free tuning of the energy resolution. An elastic energy resolution as high as $2\mu eV - 3meV$ and a neutron flux up to $10^{10}n \cdot cm^2 \cdot s^{-1}$ can be obtain. The TOFTOF instrument is suitable for both inelastic and quasi-elastic neutron-scattering.
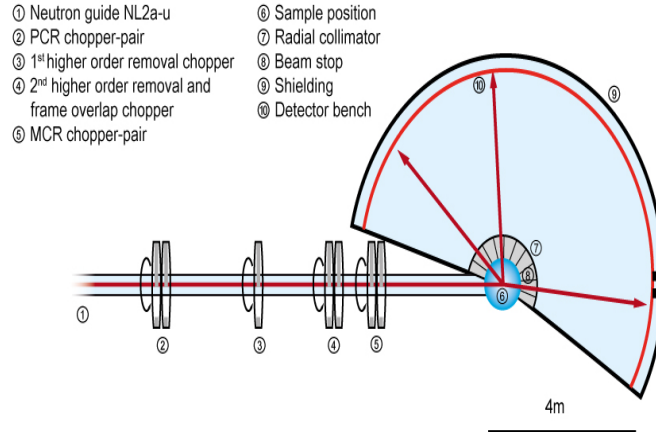
Figure 2.6: Geometry of the ToF spectrometer TOFTOF, MLZ, Garching Germany.

Backscattering spectrometer

Some large scale motions in soft matter such as the glass transition in polymers are often slow and therefore very difficult to be resolved by ToF. The observation of theses features require a much better resolution that what Time of Flight spectrometer can offer. In a ToF experiment the energy resolution is limited by the selectivity of the monochromator crystal or the pulse lengths given by the choppers that can be very small but at the expense of the intensity. Using a perfect crystal the spread of the selected wavelength $\Delta\lambda/\lambda$ is determined by the angular divergence $\Delta\alpha$ of the reflected neutrons. Differentiating the Bragg conditions $\lambda = 2sin\theta/d$ one obtains:

$$\Delta\lambda/\lambda = cot\theta \, . \, \Delta\theta \tag{2.66}$$

From the previous equation, if the neutron beam is reflected by $180°C$ then $\Delta\lambda/\lambda = 0$ which permit to improve drastically the resolution.

In Figure 2.7, a schematic representation of the SPHERES backscattering instrument used in this study can be observed. The first crystal is only a defector with low wavelength selectivity whereas the second one in backscattering

position permit the actual monochromomatization.

After their monochromatization, the neutrons are first scattered by the samples and then scattered again by the surrounding analyser crystals placed on the spherical surface. The reflected neutrons have to go through the sample again and finally hit the detector. However, the backscattering instrument raises some major technical challenges. The detector should not accept all neutrons in order to avoid the monochromatized beam to be scattered back into the source. Also, the multiple additional scattering caused by the second passage of the neutrons through the sample must be reduced. To investigate our system the SPHERES instrument at MLZ, Garching has been used. It is a third generation backscattering instrument with focussing optics and phase-space-transform chopper.
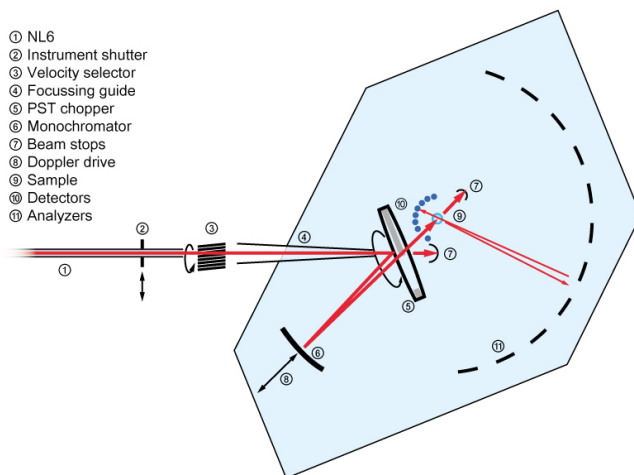
Figure 2.7: Geometry of the Backscattering spectrometer SPHERES, MLZ, Garching Germany.

Diffraction with polarization analysis: DNS

Diffraction with polarization analysis where performed on a diffusive scattering cold neutron time-of-flight spectrometer with both longitudinal and vector polarization analysis. This instrument allows the separation of nuclear coherent, spin incoherent and magnetic scattering contributions simultaneously over a large range of scattering vector Q and energy transfer E. One can observed in Figure. 2.8 the horizontal and vertical focussing monochromator, and a wide angular range around the sample is covered with detectors. The monochromatic incident beam is polarized with a focusing super-mirror bender, xyz-field coils allow for a change of the polarization at the sample, and the polarization analysis is performed with super-mirror analysers in focusing arrangement in front of each detector.

Measurements of the differential scattering cross sections were carried out by using the Diffuse Neutron Scattering Spectrometer (DNS) at the Forschungs-Neutronenquelle Heinz Maier-Leibnitz (MLZ) in Garching (Germany) capable of polarization analysis. Since the neutron spin is flipped with 2/3 probability in incoherent scattering due to nuclear spin disorder, whereas no flip occurs in the case of coherent scattering, this kind of analysis allows separating spin-coherent and spin-incoherent contributions [52]. In the ideal case where no instrumental effects apply, the ratio of the coherent to incoherent differential scattering cross sections of polarized neutrons is related to the spin-flipped $I_{SF}(Q)$ and non spin-flipped $I_{NSF}(Q)$ intensities as:

$$\frac{\left(\frac{\partial\sigma}{\partial\Omega}\right)_{coh}(Q)}{\left(\frac{\partial\sigma}{\partial\Omega}\right)_{inc}} = \frac{I_{NSF}(Q) - \frac{1}{2}I_{SF}(Q)}{\frac{3}{2}I_{SF}(Q)} \tag{2.67}$$

Here, the momentum transfer $Q = 4\pi\lambda^{-1}\sin(\theta/2)$ is the modulus of the scattering vector, with θ the scattering angle. An incident neutron wavelength of λ = 4.2 Å was used at DNS covering a Q-range from Q = 0.2 Å^{-1} to Q = 4 Å^{-1}.
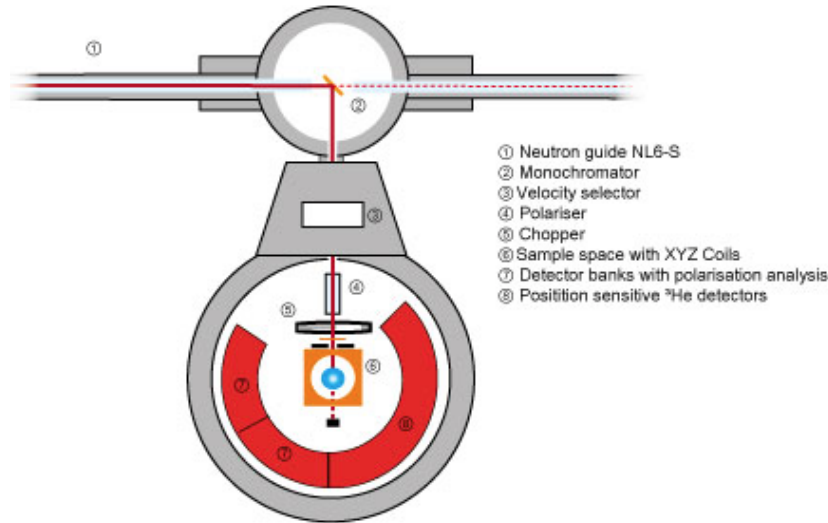
Figure 2.8: Geometry of the Diffuse Neutron Scattering Spectrometer (DNS), MLZ, Garching Germany.

Small Angle Neutrons Scattering: SANS

Small angle scattering is an useful technique in order to characterise structures of length scales between 1 and 1000nm which corresponds to a scattering vector of magnitude between 1 and $10^{-3}nm^{-1}$. The incident wave vector k is defined by two distant apertures of comparable size. The size of the collimation for a given cross-section is directly proportional to the distance between the diaphragms. The sample is placed next to the second aperture and the scattered neutrons are being recorded in a detector. The sample-detector distance is usually comparable to the collimation distance which make the overall length of theses instruments from 40 up to 80m. Small angle scattering from the sample appears on the position sensitive area detector around the primary beam stop. In this study KWS-2 SANS Instrument at MLZ, Garching, Germany has been used in order to obtain structural informations of our samples. KWS-2 represents a classical pinhole SANS instrument whose geometry can be appreciated in Figure. 2.9. Combining the pinhole mode using different neutron wavelength from 3 up to $20\mathring{A}$ and a sample detector distance from 2 up to 20m a wide Q-range typically from 10^{-4} to $0.5A^{-1}$ can be explored.
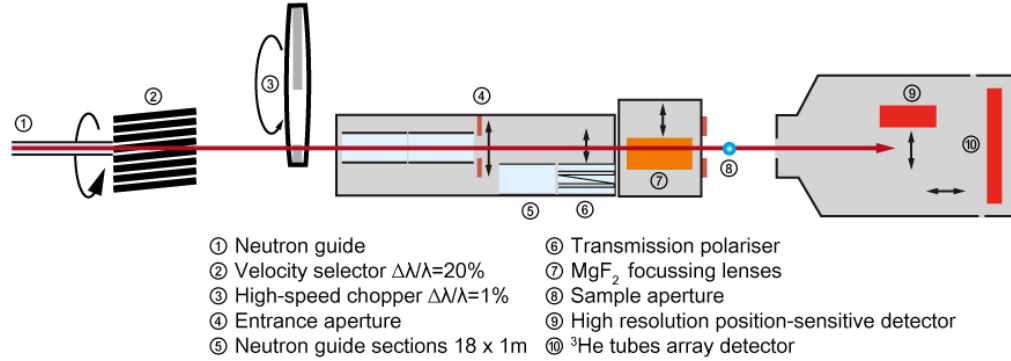
Figure 2.9: Geometry of the Small Angle Neutron Scattering Instrument KWS-2, MLZ, Garching Germany.

2.2.3 Modulated Differential Scanning Calorimetry (MDSC)

Differential Scanning Calorimetry is a widely used tool in order to measure changes in heat flow which arise from any transitions. In a typical DSC experiment, the difference in the amount of heat required to increase the temperature of a sample and a reference is measured as a function of the temperature. The reference and the sample are heated at the same rate, and the temperature difference between them is recorded. Whenever the studied sample experienced a transition process, a temperature difference is observed. The process is called endothermic if it leads to energy absorption and exothermic when some heat is released. Modulated Differential Scanning Calorimetry (MDSC) is an improved technique compared to a classical DSC device. An oscillating heat profile is applied to the sample and superimposed with the traditional linear one. In an MDSC experiment the modulated temperature can be written as:

$$T(t) = T_0 + \beta t + A_t sin(\omega t) \tag{2.68}$$

Where T_0 is the initial temperature, β is the linear heating rate, t is the time, A_t is the amplitude of temperature modulation and ω is the modulation frequency. Thus, the time dependent heating rate will be:

$$\frac{dT}{dt} = \beta + A_t \omega cos(\omega t) \tag{2.69}$$

The main advantage of MDSC is the separation of the reserving and non-reserving components of the heat flow.

$$\frac{dH}{dt} = C_p \frac{dT}{dt} + f(T, t) \tag{2.70}$$

where $\frac{dH}{dt}$ is the average DSC heat flow signal, C_p is the heat capacity, $\frac{dT}{dt}$ is the measured heating rate, which has both a linear and a modulated

components. The function $f(T, t)$ corresponds to the kinetic component of the total heat flow and is calculated from the difference between the Total Signal and the Heat capacity components. In this sense $C_p \frac{dT}{dt}$ gives the reversing heat flow component of the total heat flow. MDSC allows to measures the total heat flow, the heat capacity component and then obtain the kinetic component from their difference. The MDSC ability to resolve complex transitions into specific components lead to better data interpretation.
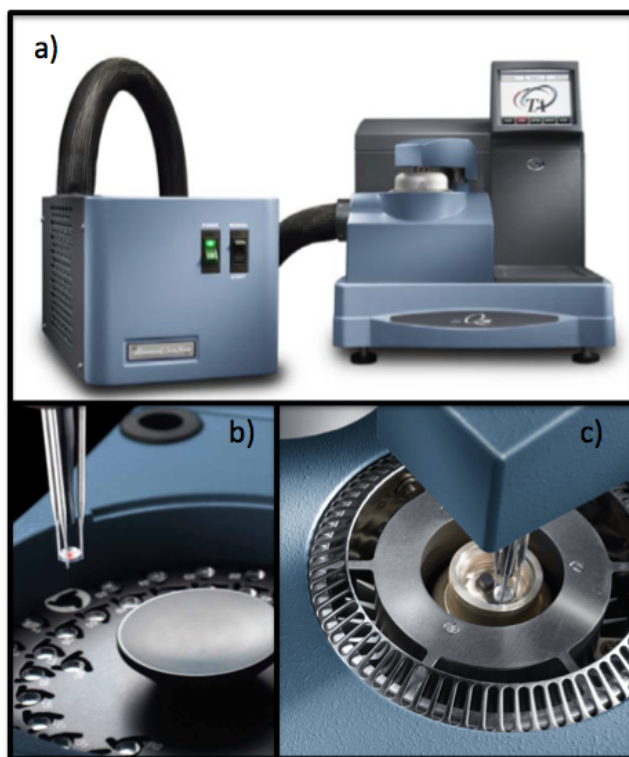
Figure 2.10: a) TA instruments Q2000 calorimeter. b) Automatic sample loader. c) Instrument Tzero cell.

DSC Instrument setup

The complete TA instrument Q2000, which can be observed in Figure. 2.10 is a research-grade differential scanning calorimeter. High quality DSC experiments require precise purge gas flow rates. Mass flow controllers, along with integrated gas switching, provide flexible control as part of individual methods. Purge gas flow rates can be set from 0-240mL/min in increments of 1mL/min. A liquid Nitrogen Cooling System (LCNS) allow to reach a lowest operational temperature of -180°C, a cooling rate capacity up to -140°C/min, and an upper temperature limit of 550°C.

In this thesis, Differential Scanning Calorimetry (DSC) measurements were

carried out on approximately 10 mg of sample using a Q2000 TA Instrument. Measurements were performed by placing the samples in sealed aluminum pans. A helium flow rate of 25 mL/min was used throughout. Data were acquired during cooling at 3 $^{\circ}C$/min from 100 $^{\circ}C$ to -100 $^{\circ}C$. Temperature-modulated experiments (MDSC) were performed using a sinusoidal variation of 0.5 K amplitude and 60 s period.

2.2.4 Mechanical measurements

In the case of mechanical spectroscopy, the available frequency range is much narrower than in the case of dielectric spectroscopy. Typically mechanical measurements are performed between (0.001 and 1000Hz) and a better precision of measurements toward low frequency is generally obtained. Also, one has to take into account the different coupling between mechanical stress and molecular groups compared to dielectric spectroscopy.

Dynamic Mechanical Analysis

Dynamic mechanical analysis (DMA) is a key technique to study and characterize materials and in particular for studying the viscoelastic behaviour of polymers. A sinusoidal stress is applied to a sample of known geometry and the strain in the material is measured, allowing to determine the complex mechanical modulus. The temperature of the sample, the frequency of the stress or a combination of theses parameters are often varied, leading to variations in the complex modulus. DMA can be used to efficiently locate the glass transition temperature of the material but also to identify transitions corresponding to other molecular motions such as secondary relaxation processes.

The instrumentation consists of a linear variable differential transformer which measures a change in voltage as a result of the instrument probe moves through a magnetic core. This instrument is also composed of a temperature control system, a linear motor, a drive shaft support and a guidance system to act as a guide for the force from the motor to the sample. Finally the sample clamps hold the sample which is being tested. A general schematic of the primary components of a DMA instrument is shown in Figure 2.11.

In this study, Dynamic Mechanical Analysis has been used to investigate the mechanical relaxation of our samples previously vulcanised. The vulcanisation does not affect the relaxations of the samples [15] and is only used in order to avoid the sample to flow during the experiment. Dynamical mechanical spectra were obtained with an MTS Model 831 Dynamic Mechanical Analysis instrument. The mechanical properties of the samples ($E^* = E' + iE''$) were recorded varying the temperature from 173 to 373K and the frequency from 0.1 up to 1000Hz. In order to stay in the linear regime small shear deformation close to 0.20 % were applied.
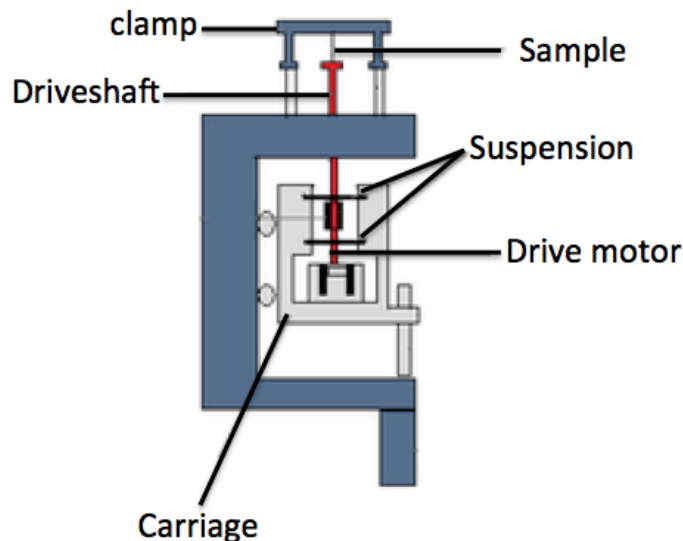
Figure 2.11:   General schematic of a Dynamic Mechanical Analysis instrument.

Rheometer

Complementary to the dynamic mechanical analysis, mechanical modulus can also be measured with rheological measurements. The rheological measurements have been performed on ARES rheometer. A strain is applied to a material via a motor, and the resultant stress is measured using transducer technology. DC servo actuators that control strain, strain rate, and frequency make possible accurate measurements of flow and viscoelastic properties.

Torque transducers measure the torque generated by the sample when the motor applies the deformation. A capacitive position sensor detects angular movement and a rotary motor measures the reaction torque to drive the geometry back to the original position. By decoupling the inertia of the system from the measurement, the transducer permits accurate and precise oscillatory measurements independent of sample viscosity. Depending on the application, different geometries of the instrument are awailable. The parallel plate geometry is widely used in the soft matter field.

In this work, rheology has been used to probe the molecular dynamics responsible for the mechanical relaxation of our samples. Dynamical mechanical spectra were obtained with an Ares-LS2 rheometer from TA Instrument using the parallel plate geometry as can be observed Figure 2.12. Sample radii and gap were 8mm and 1mm and the dynamic shear modulus was measured from 15 to 0.1Hz at strain of 0.1 wt %.
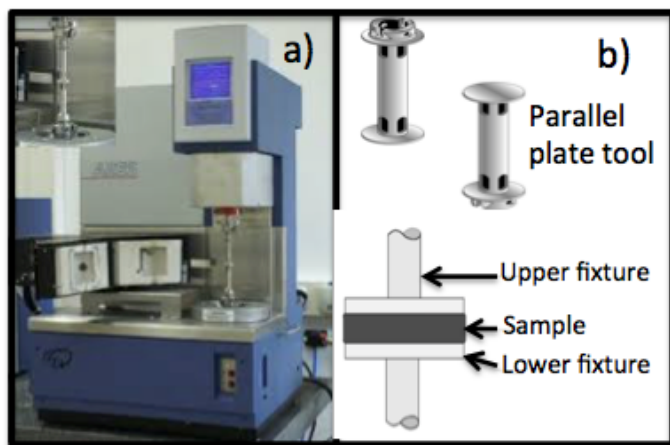
Figure 2.12: a) Ares-LS, TA Instrument device. b) Schematic view of the parallel plate tool.

Chapter 3

Applying Polymer Blend Dynamics Concepts to a Simplified Industrial System. A Combined Effort by Dielectric Spectroscopy and Neutron Scattering

The aim of this chapter is to apply the methodology described in the previous chapter to the investigation of the dynamics of a simplified industrial system, particularly a blend of styrene-butadiene rubber (SBR) with an oligomer of polystyrene (PS), in order to obtain detailed information about the segmental dynamics of both components in the blend. Using PS-oligomers, the high-T_g component acts as a "plasticizer". Varying the oligomer concentration allows tuning the average T_g of the system; also, miscibility is favored by using smaller macromolecules. In practice, it is observed that using these oligomers the greep performance is improved. On the other hand, from an academic point of view we note that it is not obvious *a priori* that theoretical frameworks developed and checked on canonical miscible polymer blend systems would also apply to the complex case of a mixture of a copolymer and an oligomer. As experimental techniques, in this chapter, we used DSC, BDS and neutron scattering (both, quasielastic as well as elastic fixed window scan measurements, together with diffraction with polarization analysis). To exploit neutron scattering selectivity, the use of samples where one of the components is deuterated is mandatory. The obtention of deuterated compounds yield changes in polymer microstructure, as presented in Chapter 2, posing difficulties in the joint analysis of the

experimental results. They were overcome by the judicious combination of BDS and QENS results on all the partially deuterated samples used in this work, based on applying a model which considers both key ingredients in blend systems –dynamic heterogeneity and concentration fluctuations. In this chapter, in addition to the pure components (hSBR2, dPS, dSBR and hPS2) we study two labelled blends (50 wt %), where SBR is protonated and PS is deuterated (hSBR/dPS). The opposite label blend, dSBR/hPS is also studied where the SBR component is deuterated whereas PS is protonated. The results obtained in this way show that the effect of blending PS oligomer with SBR on each component is mainly encoded into a distribution of effective T_gs originated from these combined ingredients. The temperature range covered by the obtained distributions nicely agrees with that of the broad glass-transition feature characterizing these materials as observed by DSC. Moreover, we also find a nice agreement between the deduced effective T_g-range of the individual components and the onset of the 'microscopic softening' revealed by the neutron elastic scans. Noteworthy, these good agreements are obtained despite the complexity of the investigated mixtures, where already the dynamical properties of the pure components are noticeable affected by relatively small differences in copolymer composition and/or microstructure of the polymers involved. This gives support to the robustness of the approach followed. Conversely, the analysis of the Q-dependence of the QENS results reveals non-Gaussian effects that could be attributed to the inherent heterogeneous atomic motions of the components even in the high temperature range accessed by this technique –where the effects of the distributions due to concentration fluctuations are expected to be practically negligible.

3.1 Experimental results

a. Differential Scanning Calorimetry.

The calorimetric T_gs of the samples were determined using MDSC by picking up the inflexion point of the reversible part of the heat flow (see Fig. 3.1). Starting with the neat systems, we note some differences in T_g between the protonated polymer and its respective deuterated counterpart for both SBR and PS, that could be attributed to the small differences in their microstructures, molecular masses and/or to isotopic effects (see Table 2.1). Due to their relatively low M_n, neat PS-oligomer samples show T_g-values around 280 K, significantly lower than the typical T_g value of PS. Even so, the values of T_g for the pure SBR samples are markedly lower –SBRs display their T_gs around 213 K (note that for the SBR investigated $M_n(SBR) \approx 23$ kg/mol is much larger than the entanglement mass $M_e(SBR) \approx 3$ kg/mol). The difference between the T_gs of the two pure components, ΔT_g, is thus close to 70 K and their blends can be considered as binary dynamically asymmetric blends. [24] In this case, SBR is the low-T_g (fast) component and polystyrene the high-T_g (slow) component. As expected, the glass-transition processes of the blends manifest as broad features in the range

between the T_gs of the pure components. Though nowadays it is established that each of the components display a different segmental relaxation in the blend, the corresponding effective T_gs are usually difficult to be resolved in the DSC traces. Therefore, to a first approximation, we have characterized the DSC results in the blends in the same way as in the homopolymers, namely by determining the inflection point. The such obtained results are listed in Fig. 3.1.

Sample	T_g(K)
dPS	283
hPS	279
hSBR/dPS	232
dSBR/hPS	237
hSBR	214
dSBR	212
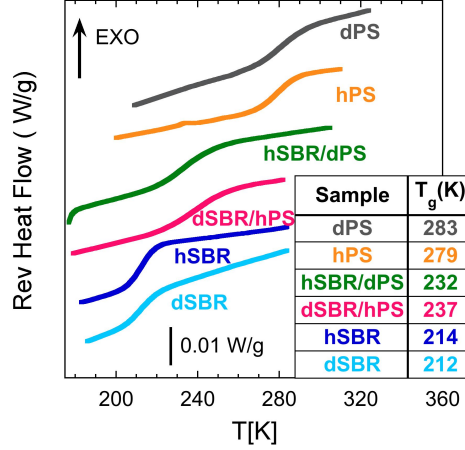
Figure 3.1: Reversible heat flow during cooling at 3 K/min for the samples investigated.

b. Elastic Fixed Window Scans and Diffraction with polarization analysis.

With increasing temperature the increasing mobility of the scattering centers (protons) translates into a decrease of the elastic contribution to the neutron scattering spectra. From the Q-dependence of this intensity, the mean squared displacement of the scattering centers at a time determined by the instrumental resolution $\langle r^2_{t_{Res}}(T) \rangle$ ($t_{Res} \approx 1/\omega_R$, where $\hbar\omega_R = \delta\hbar\omega$) can be estimated.

On the other hand, in the ideal case where no instrumental effects apply, the ratio of the coherent to incoherent differential scattering cross sections of polarized neutrons is related to the spin-flipped $I_{SF}(Q)$ and non spin-flipped $I_{NSF}(Q)$ intensities as:

$$\frac{\left(\frac{\partial\sigma}{\partial\Omega}\right)_{coh}(Q)}{\left(\frac{\partial\sigma}{\partial\Omega}\right)_{inc}} = \frac{I_{NSF}(Q) - \frac{1}{2}I_{SF}(Q)}{\frac{3}{2}I_{SF}(Q)} \tag{3.1}$$

Here, the momentum transfer $Q = 4\pi\lambda^{-1}\sin(\theta/2)$ is the modulus of the scattering vector, with θ the scattering angle. An incident neutron wavelength of $\lambda = 4.2$ Å was used at DNS covering a Q-range from $Q = 0.2$ Å^{-1} to $Q =$

4 Å^{-1}. Experiments were carried out at 295 K. The raw data were corrected for detector efficiency, flipping ratio, sample container and absorption using MLZ standard programs, finally obtaining the ratio between the coherent and incoherent differential scattering cross sections as function of scattering vector Q.

Using fully or partially protonated samples, the neutron signal is expected to be dominated by the incoherent contribution from the protons. The calculation of the ratio between coherent and incoherent cross sections $\sigma_{coh}/\sigma_{inc}$ for the samples investigated gives values between the minimum 0.075 for hSBR and the maximum 0.25 for the blend hSBR/dPS. These values correspond to the $Q \to \infty$ asymptotic limit of the ratio of the differential cross sections, but in the Q-range explored by QENS the coherent signal is in general Q-dependent. DNS provides the relative contributions of coherent and incoherent scattering to the scattered signal as function of the scattering vector. This serves as a guide to determine the optimal Q-range to analyze the QENS spectra and will be helpful for the interpretation of the dynamics results. Figure 3.2 shows the results obtained by DNS for the pure protonated components and the blends investigated by QENS. Since the incoherent differential cross section is independent of Q, the Q-dependence of the DNS data is imprinted by the coherent contribution, revealing the corresponding partial structure factor. A broad peak centered around 1.4 Å^{-1} is observed for all the samples. This peak reflects the short-range order of the polymeric chains. In addition, the blends results show a pronounced increase with decreasing Q-value for $Q \leq 1$ Å^{-1}. Such coherent contribution is originated by the contrast between the protonated and the deuterated chains. The interpretation of the structural information provided by DNS is developed in chapter 5. Here we mainly focused on the dynamical aspects accessed by the ToF and backscattering instruments, the interesting outcomes of the DNS results are that (i) the incoherent contribution (originated from the protons) clearly dominates the signal for all the samples investigated in the Q-range $Q \geq 0.4$ Å^{-1}; (ii) for the blends, the data in the range $Q \approx 0.6...1.0$ Å^{-1} show a minimum for coherent scattering, being this therefore the optimum Q-region to isolate the incoherent contribution; (iii) the data in the range $1.0 \leq Q \leq 1.6$ Å^{-1} could be affected by collective contributions from the partial structure factor; for $Q \geq 1.6$ Å^{-1} the coherent scattering is again relatively weak, and (iv) the low-Q data (below $Q \approx 0.5$ Å^{-1}) of the blends contain a rather strong coherent contribution.
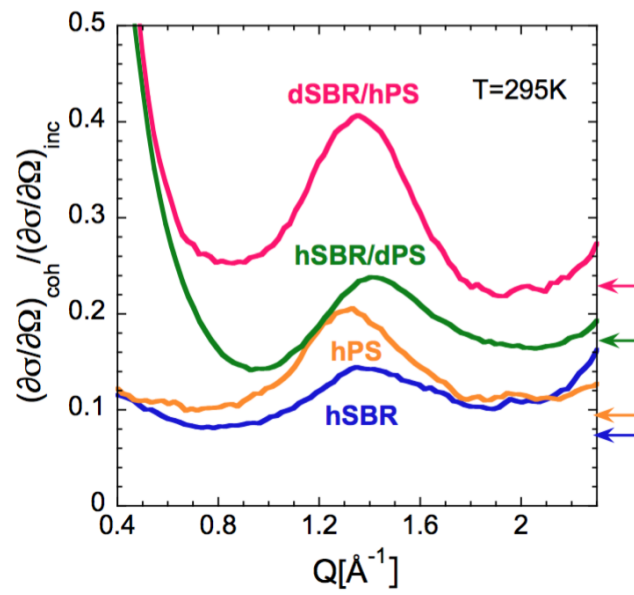
Figure 3.2: Diffuse Neutron Scattering results obtained for the pure protonated components and the blends at 295 K. The ratio of the coherent over the incoherent differential scattering cross section is presented as a function of momentum transfer. With the same color code, the horizontal arrows on the right mark the ratio between coherent and incoherent cross sections $\sigma_{coh}/\sigma_{inc}$, i. e., the theoretically expected $Q \to \infty$ asymptotic limit.

The mean squared displacement determines the leading (Q^2) term of the expansion

$$\frac{S_{el}(Q,T)}{S_{el}(Q,T \to 0)} = \exp\left[-\frac{\langle r^2_{t_{Res}}(T)\rangle}{6}Q^2 + B(T)Q^4 + ...\right]. \qquad (3.2)$$

If the Gaussian approximation is fulfilled, the Q^2-term is enough to describe the Q-dependence of the intensity. Expression 3.2 considering the Q^2 and Q^4 terms has been used to fit the EFWS data of the blends and to extract the value of the $\langle r^2_{t_{Res}}(T)\rangle$ as function of temperature. A representative example of the quality of the fits is shown in Fig. 3.3. Some discrepancies between the theoretical description and the experimental data can be found, mainly in the region around $1.2 \le Q^2 \le 2.5$ Å^{-2} ($1.1 \le Q \le 1.6$ Å^{-1}). As can be seen from the comparison with the DNS results on this sample (Fig. 3.3(b)), these discrepancies could be attributed to coherent effects. Despite being relatively small, coherent contributions induce a modulation on the elastic intensity. Since the EFWS data have been normalized to their low-T values, the observed effect could have two origins: (i) the shift of the peak around 1.4 Å^{-1} with temperature due to thermal expension, rendering the low-T normalization as inaccurate and/or (ii) a modulation of the parameters characterizing the collective motions with the structure factor. The values of $\langle r^2_{t_{Res}}(T)\rangle$ so obtained for the two blends investigated from these measurements and analysis might thus be somehow affected by these coherent effects.

On the other hand, in the case of mixtures like those here considered, the nature of the low-Q scattering is essentially coherent, as shown by the DNS experiments. Therefore, the extracted values of the mean squared displacement could also reflect a collective dynamics and not only the self-motions of the protons.

We also note that in general, the experimental results at low Q-values are particularly sensitive to multiple scattering contributions (though in our case they should not be significant). This is another ingredient that could hamper the correct determination of the mean squared displacement, since using a temperature-dependent prefactor accounting for multiple scattering effects can also introduce ambiguities.
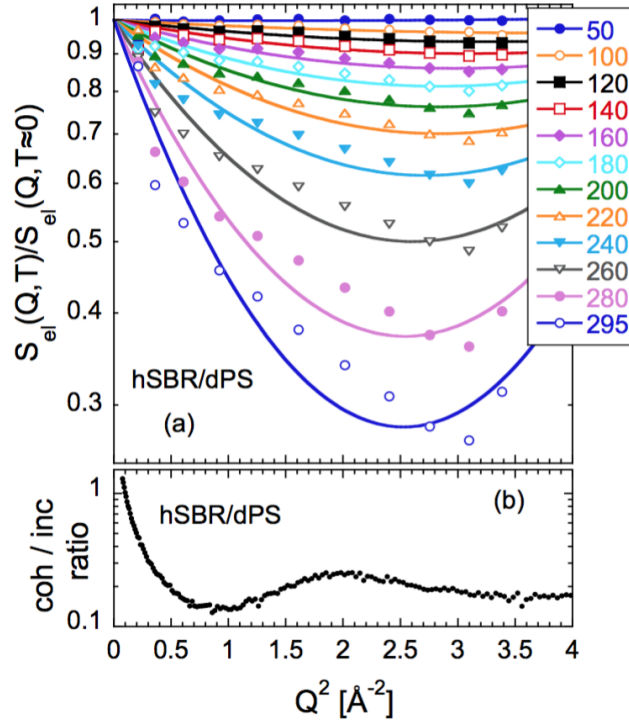
Figure 3.3: (a) Elastic intensity determined from the EFWS measurements at SPHERES for the blend hSBR/dPS at the different temperatures indicated (in K). The data have been normalized to the low-temperature values and are represented as function of the square of the scattering vector. Lines are fits to Eq. 3.2. (b) DNS results on the same sample at 295 K, plotted also as function of Q^2.

In the case of SPHERES, t_{Res} is of the order of the nanosecond. Because of being a magnitude which depends on the instrumental resolution, we will call it effective mean squared displacement. We also note that its determination is subjected to uncertainties due to several factors, in particular it can be affected by coherent contaminations as previously mentionned. The values of $\langle r^2_{t_{Res}}(T) \rangle$ obtained for the two blends investigated are represented as function of temperature in Fig. 3.4.

As can be seen in Fig. 3.4, the spatial extent of the atomic motions shows a nearly linear increase at temperatures where we expect glassy behavior for the samples according to the DSC experiments. A more dramatic increase is found at higher temperatures, which could be attributed to the dynamics of the segmental relaxation. Though qualitatively similar, the results for both samples develop in a different way, namely in a more moderate fashion for the sample dSBR/hPS. We remind that for this sample the neutron scattering results reflect the motions of the protons of the hPS component in the dSBR/hPS blend, while
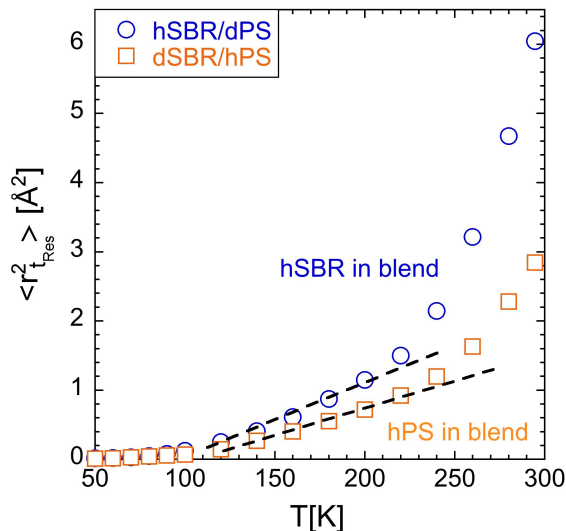
Figure 3.4: Temperature dependence of the effective mean squared displacement of protons obtained from fitting Eq. 3.2 in the two blends investigated. Dashed lines are guides to the eye displaying a linear increase in the intermediate temperature region.

for hSBR/dPS they correspond to the motions of the protons in the hSBR chains of the hSBR/dPS mixture. As can be observed in Fig. 3.4, for a given temperature, the molecular motions undergone by the hSBR component in the blend lead to significantly larger hydrogen displacements than those active in the hPS component of the dSBR/hPS mixture.

c. Quasielastic Neutron Scattering.

SBR Dynamics

We first present the results on the homopolymer hSBR as a representative example for the data analysis, which will also serve as reference for the blend results. For a Q-value of 0.6 Å^{-1} Figure 3.5 shows respectively ToF (Fig 3.5(a)) and backscattering (Fig. 3.5(b)) spectra normalized to their maxima as a function of the energy transfer. The data are compared with the respective resolution function. For the conditions chosen, the spectra collected in both spectrometers display a clear quasielastic broadening, indicative for dynamical processes with characteristic times in the region of those accessible by the instruments (tens of picoseconds to nanoseconds). To analyze the data, the spectra $S_{exp}(Q,\omega)$ measured in the energy domain were Fourier transformed into the time domain, obtaining the –still affected by the resolution– experimental intermediate scattering function $S_{exp}(Q,t)$. We remind that a convolution product in the fre-

quency domain translates into a simple product in the time domain. Thereby, the $S_{exp}(Q,t)$ functions were subsequently deconvoluted from the instrumental resolution by division by the corresponding Fourier transformed resolution signal, i.e., calculating $S(Q,t) = \frac{S_{exp}(Q,t)}{S_{res}(Q,t)}$. Figure 3.6 shows as an example the final intermediate scattering function obtained from the experimental data displayed in Fig. 3.5. Since different reference samples were used for determining the resolution of each instrument, the amplitudes of the resulting deconvoluted functions were affected by suitable matching factors. As can be appreciated in Fig. 3.6, with the wavelength used at TOFTOF, the Fourier time ranges of the two instruments almost overlap at about 0.1 ns and the degree of freedom for the adjustment of the amplitudes is very narrow. We also note that the combination of the results from TOFTOF and SPHERES allows covering over nearly 4 decades in the time domain.
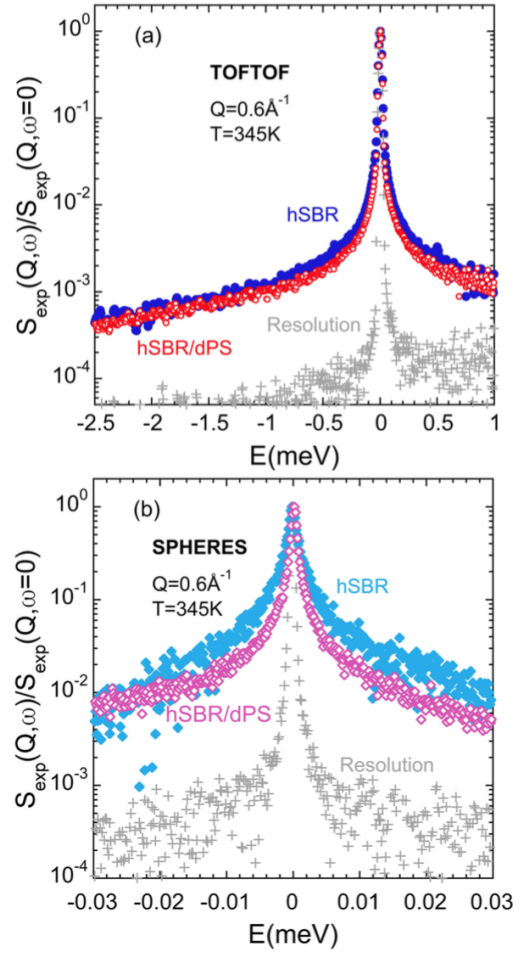
Figure 3.5: Normalized spectra measured by TOFTOF (a) and SPHERES (b) at $Q = 0.6$ Å^{-1} and $T = 345$ K compared with the corresponding resolution (crosses). Filled symbols correspond to the hSBR homopolymer and empty symbols to the hSBR/dPS blend.
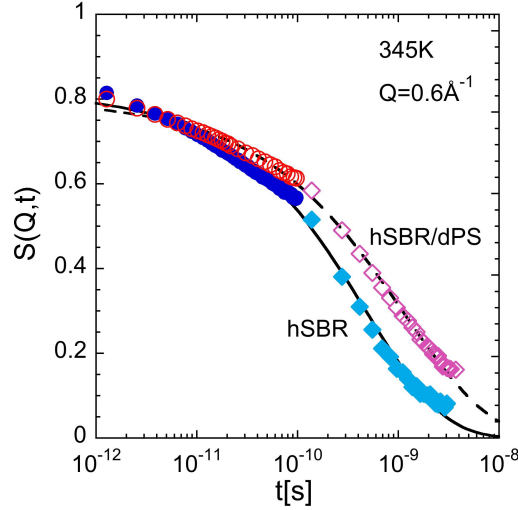
Figure 3.6: Intermediate scattering function obtained by Fourier transform and deconvolution of the results shown in Fig. 3.5 (same symbol code). Lines are fits of KWW functions (Eq. 3.3) to the experimental results for $t \geq 2ps$.

By now it is well established that well above T_g, at local length scales of the order of the intermolecular distances (few Angstroms), the main dynamical process driving the atomic motions in glass-forming systems is the decaging process involved in the structural or α-relaxation. [53] In such a range, the intermediate scattering function describing this phenomenon can be approximated by a stretched exponential or Kohlraush-Williams-Watts functional form: [65]

$$S_{KWW}(Q,t) = A(Q) \exp \left[- \left(\frac{t}{\tau_{KWW}(Q)} \right)^{\beta(Q)} \right] \tag{3.3}$$

Here β is the stretching parameter describing the deviations from the exponential behavior ($0 < \beta \leq 1$, and close to 0.5 for most polymers) [49] and τ_{KWW} the characteristic relaxation time. The prefactor A determines the amplitude of the function and accounts for faster dynamic processes. As can be seen in Fig. 3.6, this functional form describes well the intermediate scattering function also in the samples here investigated.

Figure 3.7(a) shows the resulting relaxation times for hSBR. They follow well a power law

$$\tau_{KWW}(Q,T) = a(T)Q^{-b}. \tag{3.4}$$

The b-parameter is found to be close to 3.5 for all the temperatures investigated for hSBR. We note that for a pure diffusive behavior $b = 2$. [9, 45]
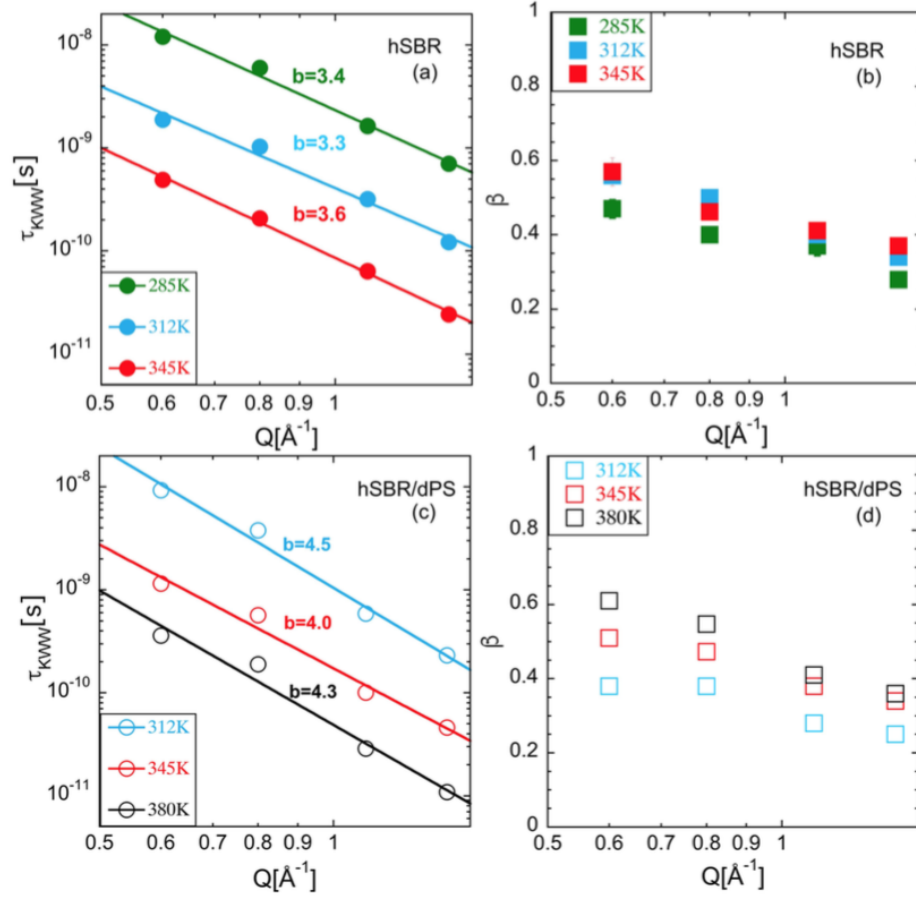
Figure 3.7: Momentum transfer dependence of the characteristic times (a, c) and stretching exponents (b, d) obtained from the KWW fit to the QENS results of hSBR (a, b) and the blend hSBR/dPS (c, d) at the different temperatures investigated. Lines are fits of Eq. 3.4 with the b-values indicated.

Figure 3.7(b) presents the stretching parameter β as function of Q. We found $0.3 < \beta < 0.6$, with a tendency to decrease with increasing Q. Figure 3.8(a) shows the temperature dependence of the β-value averaged over the Q-range investigated, $\langle\beta\rangle$. The bars in this figure mark for each temperature the interval within which the β-values are found for the different Q-values investigated. A general tendency of the values of the shape parameter to increase with increasing temperature can be observed.

For anomalous ($\beta < 1$) diffusion-like behavior, if the Gaussian approximation is fulfilled the β- and b-values are connected to each other as: $\beta \cdot b = 2$. [62]. In Fig. 3.8(b) the product of b and the data displayed in Fig. 3.8(a) is represented. The values found are smaller than the Gaussian expectation, but

tend to approach it at high temperatures. These results would be indicative of non-Gaussian effects usually interpreted in relation with dynamic heterogeneities [24].
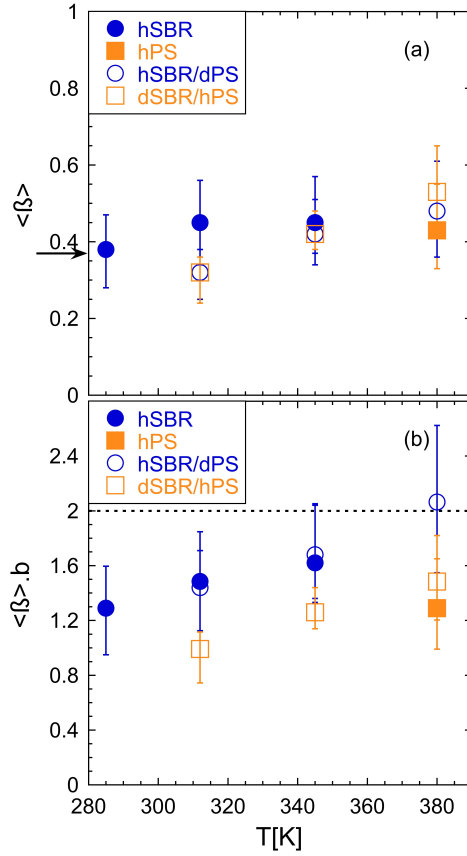
Figure 3.8: Temperature dependence of (a) the value of the stretching parameter averaged over the Q-range investigated and (b) the product of this average and the parameter determining the power-law dependence of the characteristic times obtained from the KWW-fits of the QENS data for the different samples investigated. The bars mark the interval within which the β-values (respectively, the product $\beta \cdot b$) are found for the different Qs investigated. The arrow in (a) marks the β-value used to describe the dielectric results, and the horizontal dotted line in (b), the value in the Gaussian case.

We now present the results obtained for the dynamics of hSBR in the blend

hSBR/dPS. The neutron intensity scattered by this sample at $Q \geq 0.5$ Å^{-1} is largely dominated by the incoherent scattering of the SBR hydrogens, as demonstrated by the DNS investigation. Figures 3.5 and 3.6 show that for hSBR in the blend, the QENS curves are narrower and correspondingly the intermediate scattering function decays at longer times than for hSBR in the homopolymer.

In the temperature and Q ranges here explored, the intermediate scattering function of the blend can be well described by KWW functions (see Fig. 3.6 as a representative example). Figure 3.7(c) shows the characteristic times obtained from the KWW fits, confirming a slowing down of the hSBR dynamics upon blending (compare Figs. 3.7(c) and (a)). The b-parameter values obtained from Eq. 3.4 for hSBR in the blend are close to 4.3 in average, i. e., higher than for pure hSBR ($b \approx 3.5$).

Figure 3.7(d) shows that the stretching parameter β for the hSBR/dPS slightly decreases when Q increases. The values, $0.25 < \beta < 0.6$, are in the same range as those obtained for hSBR, but change more with temperature. In particular, we observe significantly smaller β-values at 312 K for the blend than for the homopolymer. This can be better appreciated in Fig. 3.8(a). Figure 3.8(b) shows that the deviations from Gaussian behavior of the protons in hSBR are rather similar in the homopolymer and in the blend.

PS Dynamics

Figure 3.9(a) shows the relaxation times obtained from fitting the intermediate scattering function results for the pure sample, hPS, at the temeprature investigated of 380 K. Again they follow well a power law (Eq. 3.4) with $b = 3$. Figure 3.9(b) shows that for hPS β slightly decreases when Q increases. The product $\beta \cdot b$ for hPS also reveals non-Gaussian behavior, as can be appreciated in Fig. 3.8(b).
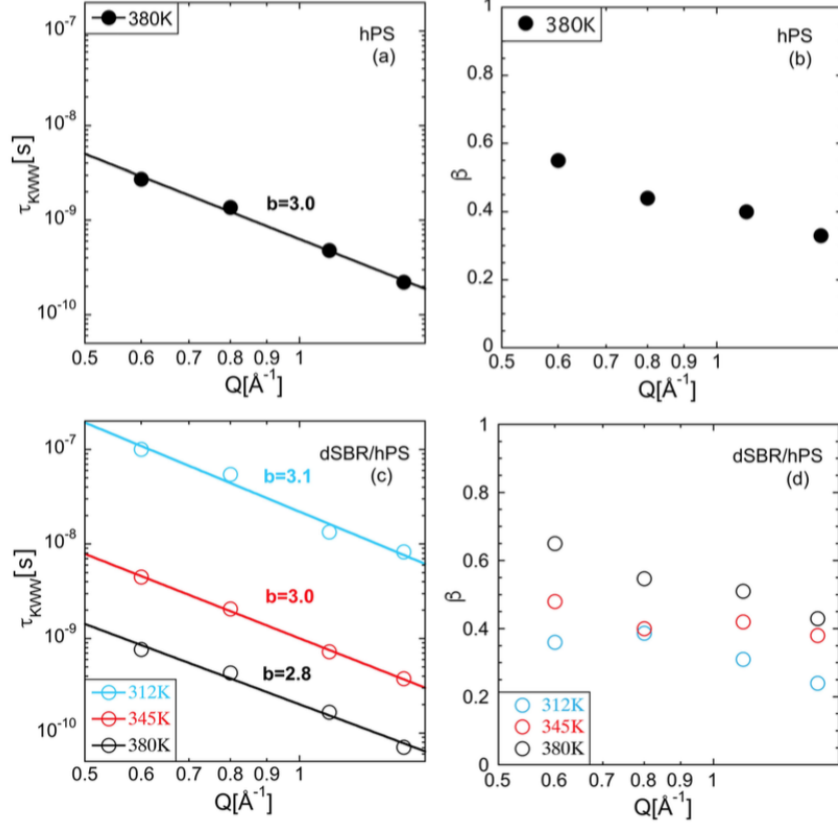
Figure 3.9: Momentum transfer dependence of the characteristic times (a, c) and stretching exponents (b, d) obtained from the KWW fit to the QENS results of hPS (a, b) and the blend dSBR/hPS (c, d) at the different temperatures investigated. Lines are fits of Eq. 3.4 with the b-values indicated.

The dynamics of polystyrene in the blend was followed by the QENS experiments on the sample dSBR/hPS, which above $Q \approx 0.5$ Å^{-1} are largely dominated by the incoherent contribution from protons of the polystyrene component.

We have made a rough estimation of the diffusive contribution of the PS oligomers based on the Rouse model. Considering the result at $Q=0.6$Å^{-1} ($\beta \approx 0.5$, $\tau_{KWW} = 2.7$ ns), we have assumed the Rouse expression $\tau_{self} = 9\pi/(W\ell^4 Q^4)$ to estimate the value of the Rouse variable $W\ell^4 \approx 81$Å^4/ns. From SANS results, on a mixture of deuterated and protonated styrene oligomers, which are presented in detail in chapter 5, we deduced $R_g = 10.3$ Å which corresponds to $R_e = \sqrt{6}R_g = 25$ Å. This gives an approximated value of 0.042 Å^2/ns for the translational diffusion coefficient in the Rouse model $D = W\ell^4/(3R_e^2)$. The corresponding characteristic time for translational diffusion $\tau_D = Q^{-2}D^{-1}$

is represented in Fig. 3.10. For example, at $Q = 0.6$ Å^{-1} this time would be about 66 ns, i. e., about 25 times that actually obtained from the KWW fit and practically out of the QENS dynamical window. Thus, the contribution from translational diffusion to pure PS dynamics could be considered as rather weak at the temperature investigated.
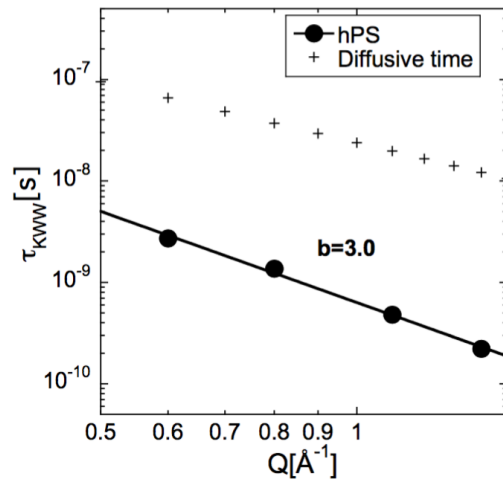
Figure 3.10:   Experimentally obtained characteristic times of hPS at 400K (circles) compared with the estimated times corresponding to the translational diffusion component of this oligomer (crosses).

The same kind of estimation for the blend results leads to diffusive contributions beyond or comparable to the QENS resolution window for the two lowest temperatures investigated. Only the highest temperature results could be somehow influenced by the diffusive terms, mainly at high Q-values (see Fig. 3.11).
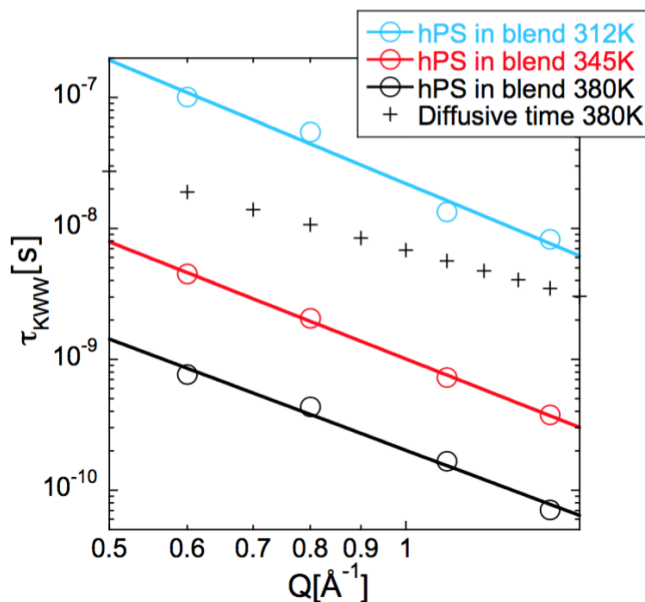
Figure 3.11: Experimentally obtained characteristic times from the blend dSBR/hPS at different temperatures (circles) compared with the estimated times corresponding to the translational diffusion component of this oligomer at the highest temperature investigated (crosses).

The obtained characteristic times reflect a faster dynamics for hPS in the blend as compared to the pure polystyrene, at a given Q and temperature (see Figs. 3.9(c) and (a)). Solid lines in Fig. 3.9(c) stand for the fit to Eq. 3.4. In average, the b-values are found to be rather close to 3, i. e., to that in pure hPS. The stretching parameter values deduced for the dSBR/hPS sample are plotted in Fig. 3.9(d) and their averages in Fig. 3.8(a). They show basically the same features as those determined for the hSBR component in the blend hSBR/dPS. However, in the respective blends the deviations from Gaussian behavior for the hPS component are markedly stronger than for the hSBR component.

d. Dielectric Spectroscopy.

Figure 3.12 shows representative examples of the frequency dependence of the dielectric loss peak obtained for the pure polymers both protonated and deuterated. We observe how the characteristics of the main loss peak attributable to the segmental dynamics (α-relaxation) change from the protonated polymer to its deuterated counterpart.

In agreement with the DSC results, at a given temperature, the dielectric loss peaks of the two protonated homopolymers and their deuterated counterparts are centered at different frequencies, especially for PS. It is also apparent that for

both SBR and PS the deuterated homopolymer shows a broader loss peak than that observed for the protonated counterpart. Moreover, in both cases, SBR and PS, the protonated polymer shows a stronger dielectric relaxation than the deuterated one. Since dielectric spectroscopy is not sensitive to deuteration, these differences must be due to the slightly different microstructures of deuterated and protonated polymers, leading to distinct segmental dynamics.

Figure 3.13 shows representative examples of the frequency dependence of the dielectric loss peak $\varepsilon''(\omega)$ obtained at different temperatures for the pure polymers and the blends investigated by QENS. We selected temperatures where we observe a main loss peak attributable to the segmental dynamics (α-relaxation), which position strongly depends on temperature. In agreement with the DSC results, the dielectric peaks of the two homopolymers are centered at similar frequencies at much lower temperatures for SBR than for PS. From the peak values of the dielectric permittivity losses in Fig. 3.13, it can also be seen that SBR has a stronger dielectric relaxation than PS. By comparing the results on the mixtures with those on the homopolymers (Fig. 3.13(a) and (b)) it is apparent that the dielectric response of the blends is broader and intermediate between those of the neat systems, as already reported for other polymer mixtures (see, e. g. [18] and [24] as general references). We also note that the BDS results of the two blends investigated by QENS, hSBR/dPS and dSBR/hPS, do not coincide for the same temperature. For example, at 255 K, the peak observed for the sample where the SBR component is protonated (hSBR/dPS, Fig. 3.13(a)) is centered at clearly higher frequencies than that displayed by the blend with the inverse isotopic label (Fig. 3.13(b)). Nevertheless, as an example, in the normalized representation $[\varepsilon''(\omega)/\varepsilon''_{max}]$ shown in Fig. 3.14, the hSBR/dPS results at 255 K look very much the same as those corresponding to the dSBR/hPS sample at 263 K. Since dielectric spectroscopy is not sensitive to deuteration, this temperature difference has to be attributed to the somewhat different microstructure of the blend components and/or to isotopic effects leading to distinct dynamics, as reflected in the DSC measurements. We note that clear differences are also visible in the dielectric relaxation between the deuterated and the protonated pure polymers as it is illustrated Figure 3.12.
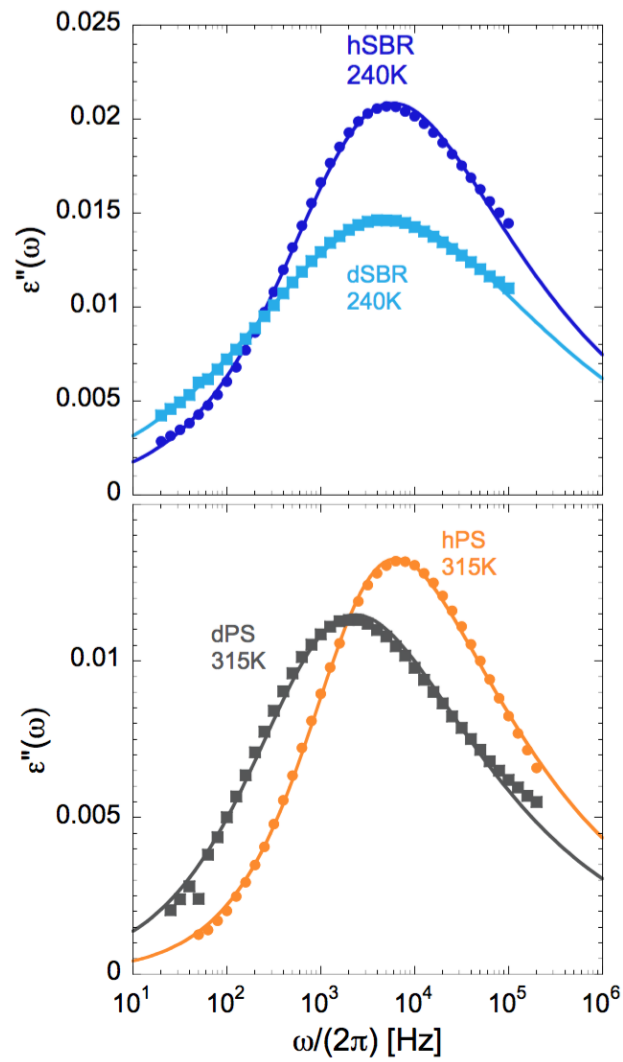
Figure 3.12: Frequency dependence of the dielectric loss for SBR and PS showing both the protonated and deuterated polymer. The lines stand for the fit of the experimental data by means of the Havriliak-Negami equation (Eq.2.12).
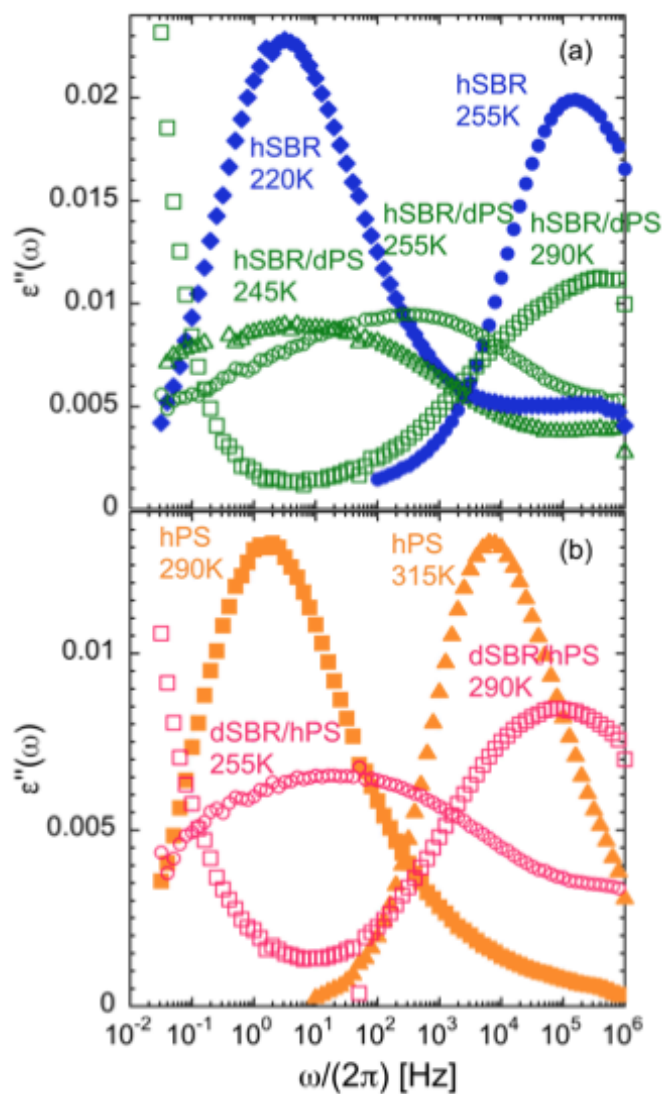
Figure 3.13: (a) Frequency dependence of the dielectric loss at 220 and 255 K for hSBR and for the blend hSBR/dPS at 245, 255 and 290 K. (b) Frequency dependence of the dielectric loss at 290 K and 315 K for hPS and for the blend dSBR/hPS at 255 and 290 K.
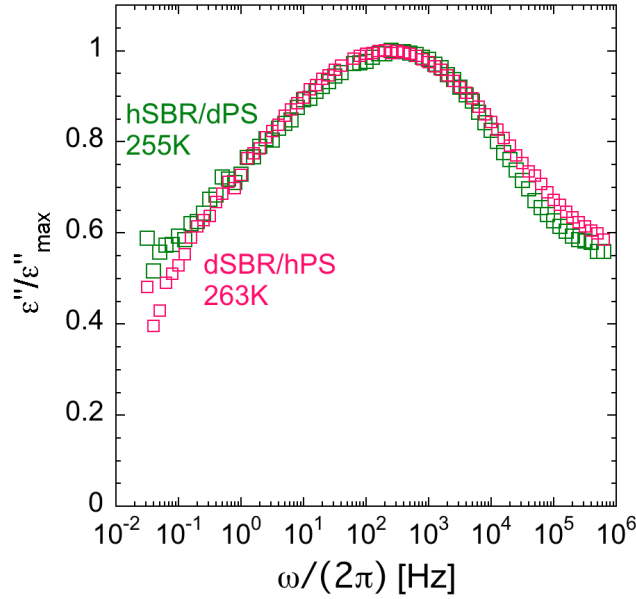
Figure 3.14: Normalized imaginary part of the dielectric permittivity for hSBR/dPS at 255 K and dSBR/hPS at 263 K as function of frequency.

Figure 3.15 shows the temperature dependence of the characteristic time scales, defined as the inverse of the angular frequencies at the dielectric loss maxima ($\tau_{max} = \omega_{max}^{-1}$) of the α-relaxation process for the pure polymers and the two blend samples investigated by QENS. For completeness, we have also included the results obtained on the deuterated homopolymers dPS and dSBR. The lines correspond to descriptions by means of the Vogel-Fulcher-Tammann VFT equation (see Eq. 1.9): [64, 28, 59]

In the fits, we kept constant the prefactor value $\tau_0 \equiv 10^{-13}$ s in the VFT equation (Eq. 1.9). First, the data of the two protonated homopolymers were considered. The values obtained for the fragility parameter D and the Vogel temperature T_0 are displayed in Table 3.1. Fixing the D-value to that obtained for the protonated counterpart, the VFT function also describes very well the data on the deuterated homopolymers. In Table 3.1 we can see that the values of the Vogel temperatures differ upon deuteration reflecting the differences found by the DSC experiments. Conversely, considering that the blend dielectric results are partially dominated by the SBR component, for describing the blend data the value of the D-parameter was fixed to be the same as that determined from the fit of the hSBR results. As can be appreciated in Fig. 3.15, the quality of the descriptions is very good for both blend samples. The difference is a shift in the Vogel temperature of about 5 K.

Table 3.1: Parameters involved in the VFT (see 1.9) description of the characteristic times shown in Fig. 3.15 with $\tau_0 \equiv 10^{-13}$ s. For the homopolymers, the dielectric strength and Havriliak-Negami parameters obtained fitting the curves well centered in the experimental frequency window are also given, as well as the value of the characteristic time at the calorimetric glass-transition temperature, τ_g.

Sample	$T_0[K]$	D	$\Delta\varepsilon$	α	γ	$\tau_g[s]$
hSBR	166.6	8.6	0.11	0.61	0.49	1.4
dSBR	166.4	8.6	0.09	0.47	0.63	3.0
hPS	231.7	6.9	0.06	0.70	0.43	47
dPS	235.3	6.9	0.06	0.65	0.46	74
hSBR/dPS	184.7	8.6	-	-	-	-
dSBR/hPS	190.1	8.6	-	-	-	-
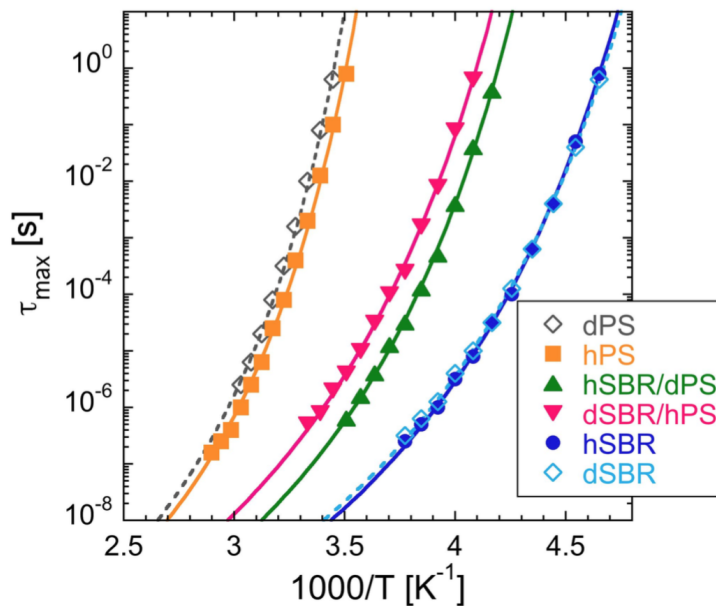
Figure 3.15: Temperature dependence of the characteristic times defined from the inverse of the frequencies of the dielectric loss maxima for the α-relaxation process of the different samples investigated. The lines correspond to descriptions by means of the VFT equation (Eq. 1.9) with $\tau_0 \equiv 10^{-13}$s. Empty symbols (corresponding fitting curves as dotted lines) stand for the deuterated homopolymers.

Regarding the shape of the relaxation curves, as usual, the results on the pure polymers can be well fitted around the main peak by means of the Havriliak-

Negami (HN) equation [37] (see Fig. 3.23)

$$\varepsilon_{HN}^{''}(\omega) = -Im\left\{\frac{\Delta\varepsilon}{[1 + (i\omega\tau_{HN})^{\alpha}]^{\gamma}}\right\} \tag{3.5}$$

where $\Delta\varepsilon$ is the dielectric relaxation strength, τ_{HN} is the characteristic relaxation time, and the fractional shape parameters α and γ describe respectively the symmetric and asymmetric broadening of the complex dielectric function $0 < \alpha$; $\alpha \cdot \gamma \leq 1$ holds. Despite the fact that the low frequency part of the loss peaks of the homopolymers slightly narrows by increasing temperature, it was possible to obtain good descriptions of the experimental data in the whole temperature range investigated keeping the product $\alpha \cdot \gamma$ constant (see Fig. 3.23). Table 3.1 presents the parameter values used to describe the loss curves of the homopolymers at temperatures where the corresponding loss peak was well centered in the experimental frequency range. The extra losses observed at higher frequencies for SBR (see Fig. 3.23(a)) are originated by the contribution of the β-process. This is mainly due to local dynamics within cis 1,4-butadiene segments [10, 46], which was not included in the model function. The HN function does not describe well the blend data since extra contributions at low frequency are evident in the loss peaks. This feature is commonly found in polymeric mixtures [34] and occurs in the the blends investigated here not only because of the expected polystyrene contribution at frequencies significantly lower than the peak of SBR but also due to the presence of thermal concentration fluctuations. [39]

We note that (under certain constraints) HN functions are descriptions of the Laplace transform of KWW relaxation functions. [5] The β-parameter value of the KWW function in the time domain corresponding to the HN functions describing BDS data can be calculated as $\beta \approx (\alpha \cdot \gamma)^{0.813}$, which provides $\beta \approx 0.37$ for the investigated homopolymers.

In the following, we show how the characteristic time of the susceptibility maximum can be obtained from the value of the KWW time corresponding to a given β-value. This transformation is necessary to compare the BDS results with those obtained above from QENS experiments. We illustrate the procedure with an example (β=0.55).

From the values of τ_{KWW} and β, the values of the shape parameters α and γ of the corresponding HN relaxation function in the frequency domain can be calculated from Ref. [4] as given in the tables of that reference and in the plots reproduced here (Figs. 3.16 and 3.17).

The arrow in Fig. 3.16 illustrates the case β=0.55, for which $\tau_{HN}/\tau_{KWW} \approx 2.2$.

For the considered example of β=0.55, from Fig. 3.17 we obtain α=0.82, γ=0.56.

Once the HN parameters are determined, we can calculate the characteristic time of the maximum of the susceptibility loss peak from Eq. 2.13. In Fig. 3.18 we plot directly the ratio between the time of the maximum and the HN characteristic time as function of the starting KWW β-parameter.

For β=0.55, the obtained ratio in Fig. 3.18 is 0.54. Thus, for this example, the final ratio between τ_{max} and τ_{KWW} is 0.54 x 2.2 = 1.2.
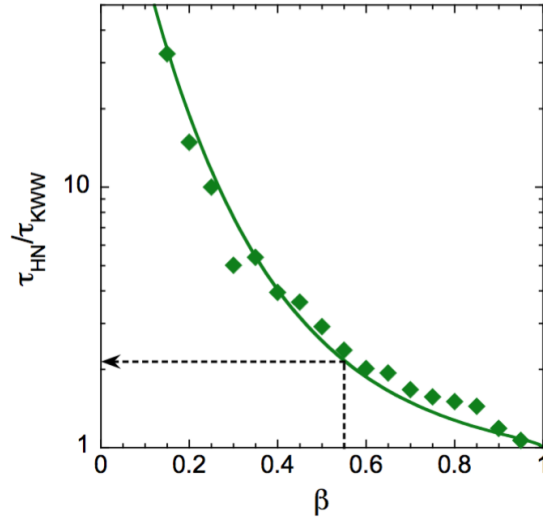
Figure 3.16: Ratio between the HN and KWW times obtained in Ref. [5]. The line is the equation 2.16 fitting the data.
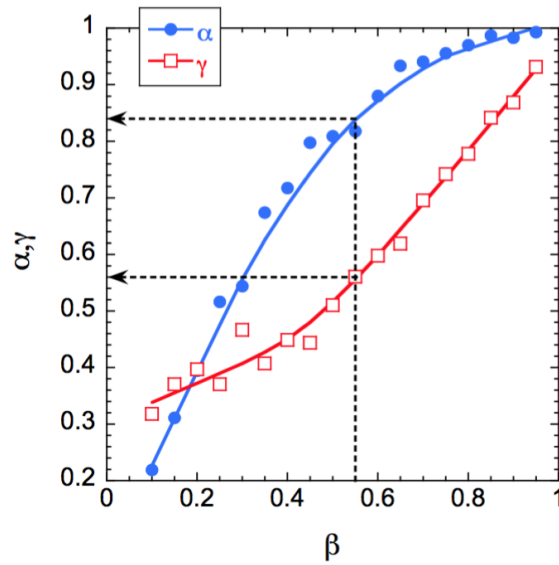
Figure 3.17: HN shape parameters corresponding to the KWW β-parameter obtained in Ref. [5]. Lines are guides for the eye.
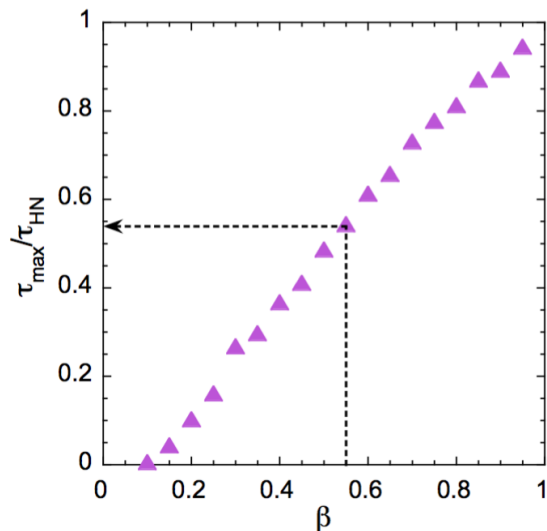
Figure 3.18: Ratio between τ_{max} and τ_{HN} obtained through Eq. 2.13. The input values of the α and γ parameters have been obtained as explained above based on the relationships shown in Fig.3.17.

We can now compare dielectric with QENS results. For both homopolymers, the stretching exponent β corresponding to the dielectric relaxation is in the range of the values obtained by QENS (see arrow in Fig. 3.8(a)). To compare the relaxation times, we have to take into account the Q-dependence of the time scale of the α-relaxation as measured by neutron scattering. In order to compare the dielectric and neutron scattering data we have first converted the QENS KWW time into a characteristic relaxation time corresponding to the maximum of the peak of the neutron dynamic susceptibility (τ_{max}). In principle, it is always possible to find a Q-value (we will call it $Q^{\star}$) at which the characteristic times of the α-relaxation determined by QENS become similar to those measured by BDS.

Combining the equations connecting KWW and HN parameters presented above, the time of the maximum susceptibility corresponding to a KWW relaxation function can be calculated. Thus, KWW neutron times can be transformed into the corresponding times characterizing the maximum neutron susceptibility. As previously commented, in neutron scattering the relaxation time is not only dependent on temperature but also on the momentum transfer Q. For $Q = 0.6$ and 0.8 Å^{-1}, Figure 3.19 shows the evolution of these characteristic relaxation times determined for the hSBR sample by means of QENS as compared to the corresponding dielectric ones. As can be seen in this figure, the extrapolation at high temperature of the law fitting the BDS data presented in the manuscript describes also very well results obtained by high-frequency dielectric measurements on the same sample. From the comparison between the DS and the QENS results, it is found that for hSBR the Q-value matching the time scales from

neutron scattering with those from dielectric relaxation appears to be $Q^\star \approx$ 0.7 Å^{-1}. As can be observed in Fig. 3.20(a), there is a good agreement between the VFT prediction of the high temperature dielectric data of hSBR and the values deduced by means of neutron scattering at $Q^\star_{SBR}$= 0.7 Å^{-1}.

Comparing the VFT line of hPS with the neutron data at 380 K, we find that $Q^\star_{PS}$= 0.55 Å^{-1} (see Fig. 3.20(b)).
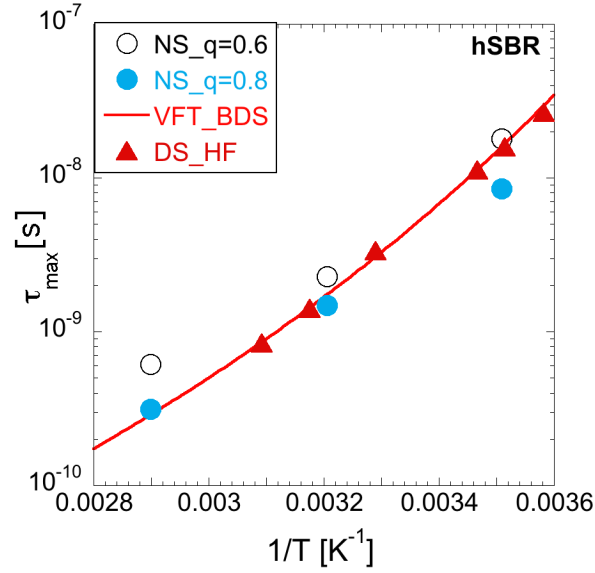
Figure 3.19: Characteristic time as function of the inverse temperature for the hSBR sample. Circles stand for the characteristic times by means of QENS, obtained at different Q-values. Triangles stand for the characteristic times obtained by means of high-frequency dielectric spectroscopy. The line is the Vogel-Fulcher-fit of the broad band dielectric spectroscopy data presented in the manuscript.
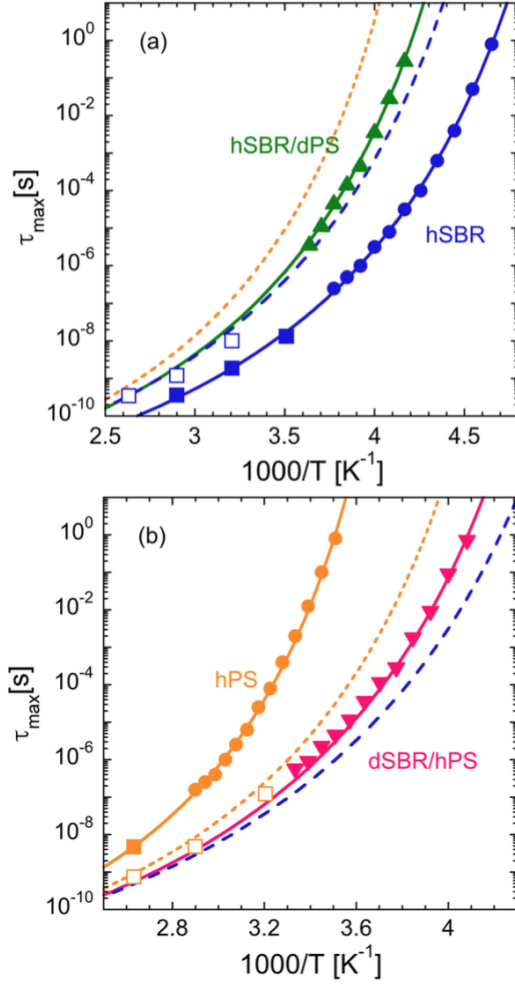
Figure 3.20: Temperature dependence of the characteristic times defined from the inverse of the frequencies of the loss maxima for the α-relaxation process obtained from dielectric spectroscopy (circles and triangles) and QENS at $Q^\star$ (squares). The solid lines correspond to a description of the dielectric data by means of the VFT equation. Dashed and dotted lines stand for the dynamics of the components in the blend (SBR and PS respectively, see text). Panel (a) shows the results for hSBR and the blend hSBR/dPS and panel (b) for hPS and the blend dSBR/hPS.

If we now consider the dynamics of hSBR in the mixture, we find that the QENS data on the blend hSBR/dPS at $Q^\star_{SBR} = 0.7$ Å^{-1} denote a slightly faster dynamics than the extrapolated high temperature dielectric data on the same sample (see Fig. 3.20(a)). This difference is what could be expected due

79

to the non-negligible slow polystyrene contribution to the BDS results of the blend. Moving to the QENS results from the dSBR/hPS sample corresponding to hPS dynamics in the blend, the values of the characteristic times at $Q^{\star}_{PS}= 0.55$ Å^{-1} are slightly larger than those deduced from BDS on the same sample (see Fig. 3.20(b)). This observation could again be attributed to the fact that hPS in the blend is moving more slowly than the average, whereas the SBR component –dominating the $\varepsilon''(\omega)$ peak position– is faster than average.

3.2 Discussion

The experimental results on our blends show clear indications of dynamic heterogeneity at the segmental level. For instance, the EFWS results reveal markedly different motional amplitudes of the two components in the two blends investigated. Also, if the QENS results on the characteristic times of the polymer components are directly compared, a clearly faster dynamics can be found for hSBR in the hSBR/dPS blend than for the hPS component in the dSBR/hPS blend as can be observed in Fig. 3.21.
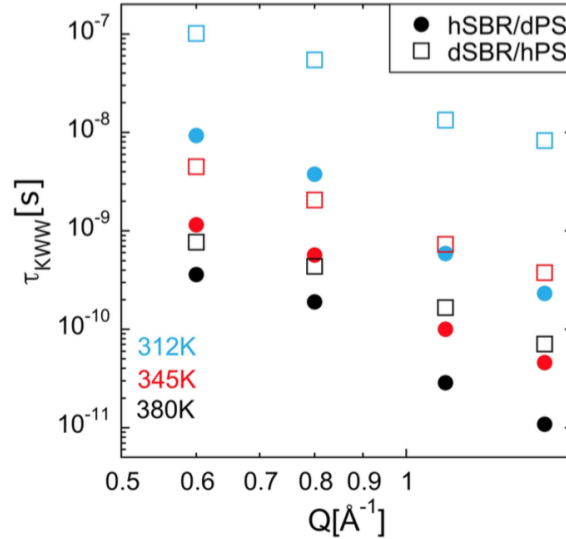
Figure 3.21: Scattering vector dependence of the characteristic time obtained from the QENS results on the hSBR component of the hSBR/dPS sample (filled circles) and the hPS component of the dSBR/hPS sample (squares) at the temperatures indicated.

This difference increases with decreasing temperature. We note however that a quantitative comparison of these results is not so straightforward, since there are differences in the dynamics of the neat components, as it has been mentioned above.

Another hint for dynamic heterogeneities in the blends can be found from the comparison between dielectric and DSC results. If, as a first approximation, we consider that the dielectric loss peak frequency in the blend mainly reflects the SBR-component dynamics, the fact that the fragility remains essentially unaltered for this component upon blending suggests that the change in T_g is the major reason for the changes in the SBR segmental dynamics in the blend. However, we note that the difference in the calorimetric glass-transition between the hSBR and the hSBR/dPS samples is 23 K, whereas the shift observed in the VFT temperature determined by BDS –attributable, in a first approximation, to the SBR component– is only 18 K. This difference is consistent with distinct segmental dynamics for the blend components, resulting in distinct effective glass-transition temperatures. In such a framework, T_g^{DSC} is an average value of the T_gs of the blend components, as anticipated in the previous section. We may examine the DSC results in more detail in order to extract information about the different behavior of the two blend components.

The calorimetric glass-transitions of the studied blends are slightly asymmetric and very broad, extending over a T-range larger than 50 K for both blends. The temperature derivative of the reversible heat flow provides a sensitive way to detect glass-transition processes. Figure 3.22 shows this function for the blends and respective homopolymers. Two overlapping glass-transition ranges could be envisaged in the blends from the high temperature shoulder of the signals; however, a reliable determination of the effective glass-transition values corresponding to each component is not possible from the DSC results. This has been realized in some specific blends of polymers whose neat components differ by more than 100 K in their respective T_g values [41, 24, 11].
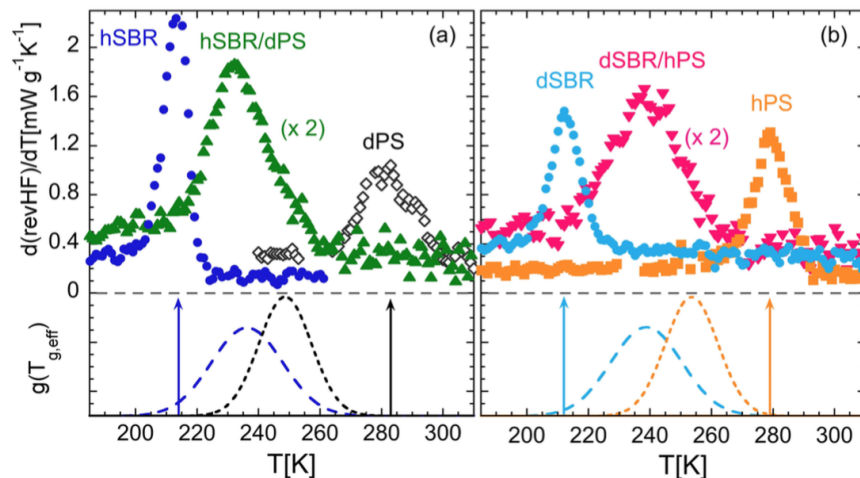
Figure 3.22: Derivative of the reversible heat flow for the blend hSBR/dPS (a) and dSBR/hPS (b) as function of temperature compared with that determined for the pure homopolymers. In the lower part of the figures, the arrows indicate the glass-transition temperatures of the neat polymers and the dashed (dotted) curves, the distribution functions of effective glass-transition temperatures of the SBR (PS) component deduced from the joint analysis of the QENS and BDS results.

In the following, we perform a joint analysis of BDS and QENS results based on concepts previously developed and by now well established for model polymer blends. The specific information provided by neutron scattering on the protonated blend component will be a key ingredient to disentangle the component dynamics of the two kinds of polymers *in the same blend*.

As can be seen in Table 3.1, the predominant contribution to the dielectric response is that of the SBR component. However, the dielectric signal of PS is significant and there would be an underlying two-peak structure in the BDS spectra with contributions from the two kinds of polymeric chains. In order to identify the component contributions to the dielectric relaxation in the blends we have assumed that each of the two components contributes proportionally to the BDS signal measured in the corresponding pure polymer. In addition, we have assumed that the contribution of each component in the blend arises as a superposition of contributions similar in shape to those of the corresponding pure polymer, but with different relaxation times. This relaxation time distribution would be mainly attributed to the presence of concentration fluctuations. [39] As aforementioned, concentration fluctuations constitute the ingredient which, together with the self-concentration effects, are believed to be decisive in determining polymer blend dynamics. Following previous results [18], it has been assumed that the effect of concentration fluctuations translates into a distribution of VFT temperatures $h(T_0)$ –equivalently, of ef-

fective glass-transition temperatures– for each of the components in the blend. The observed distributions of characteristic times are thus a consequence of the spread of VFT-temperatures in the blend, since it is usually safely assumed that the other parameters in the VFT equation (D and τ_0) can be considered nearly insensitive to concentration. [29] For the SBR components we assumed the D and τ_0 values determined above by fitting the whole peak position, i.e. $\tau_0 = 10^{-13}$ s and $D^{hSBR} = D^{dSBR} = 8.6$. In the case of the PS components we fixed $\tau_0 = 10^{-13}$ s but not the value of the fragility parameter (assuming that $D^{hPS} = D^{dPS}$), since it is well documented that the fragility of the high-temperature component in polymer mixtures is actually reduced by blending. [3, 29]

Under these assumptions, the dielectric loss peak of the blend would be expressed as:

$$\varepsilon''_{blend}(\omega) \propto \sum_c \phi_c \int \varepsilon''^c_{HN}(\omega, T_o) h^c(T_0) dT_0 \qquad (3.6)$$

where the index c refers to the component of the blend (c: hSBR and dPS for the hSBR/dPS sample, c: dSBR and hPS for the dSBR/hPS sample). The concentration ϕ^c of each component is always 50 wt% in the samples here investigated. Each contribution to the component permittivity $\varepsilon''^c_{HN}(\omega, T_o)$ is taken with shape parameters as those determined from the fits of the corresponding homopolymer data (see Table 3.1). The dielectric relaxation strength of each polymer component in the blend is assumed to be half of that determined as the average value in the corresponding homopolymer (see Table 3.1). Finally, the distribution functions $h^c(T_0)$ are assumed to be Gaussian functions given by:

$$h^c(T_0) = \frac{1}{\sqrt{2\pi}\sigma_0^c} \exp\left[-\frac{1}{2}\left(\frac{T_0 - \langle T_0^c \rangle}{\sigma_0^c}\right)^2\right] \qquad (3.7)$$

In this approach, the fitting parameters are the average value of the VFT-temperature $\langle T_0^c \rangle$ and the variance of the distribution σ_0^c for each component and one common fragility parameter D^{PS} (independent of isotopic substitution). The fitting procedure consisted of three steps: In a first step, we determined the value of D^{PS}. To do this, we made use of the selective information provided by the NS results on the dSBR/hPS sample, that reveal the temperature dependence of the hPS component in this sample at high temperature. This information however is not enough to univocally determine the value of the fragility for this blend component. Therefore, we tried to complement these high-temperature results with information from dielectric spectroscopy. We thus fitted the model function to the dielectric data of the same blend dSBR/hPS at 263 K, where the signal is well centered in the BDS window (see Fig. 3.24(b)). Assuming as first approximation the 'macroscopic' value, $D = 8.6$ for both blend components, we deduced an approximate value of the characteristic time of the PS-component in the blend at 263 K. The fit of a VFT function using this point value together with the high-temperature QENS data at $Q^\star$ allowed to determine the value of $D^{PS} = 7.6$ as the fragility of the PS component. A

second step consisted of obtaining an estimation of the values of the parameters characterizing the distributions $h^c(T_0)$ for the two blends. This was realized on the selected BDS data shown in Fig. 3.24 where the loss peaks are well centered in the experimental window. Starting from the resulting estimated values, in the third step we applied the model to other temperatures, refining the values of the parameters $\langle T_0^c \rangle$ and σ_0^c. The final values are compiled in Table 3.2. The model provides a rather satisfactory description of the data, as can be appreciated in Figs. 3.23 and 3.24. The deviations at lower and higher frequencies are respectively due to conductivity and the above-mentioned β-relaxation contributions, both of which are not considered in the model function.
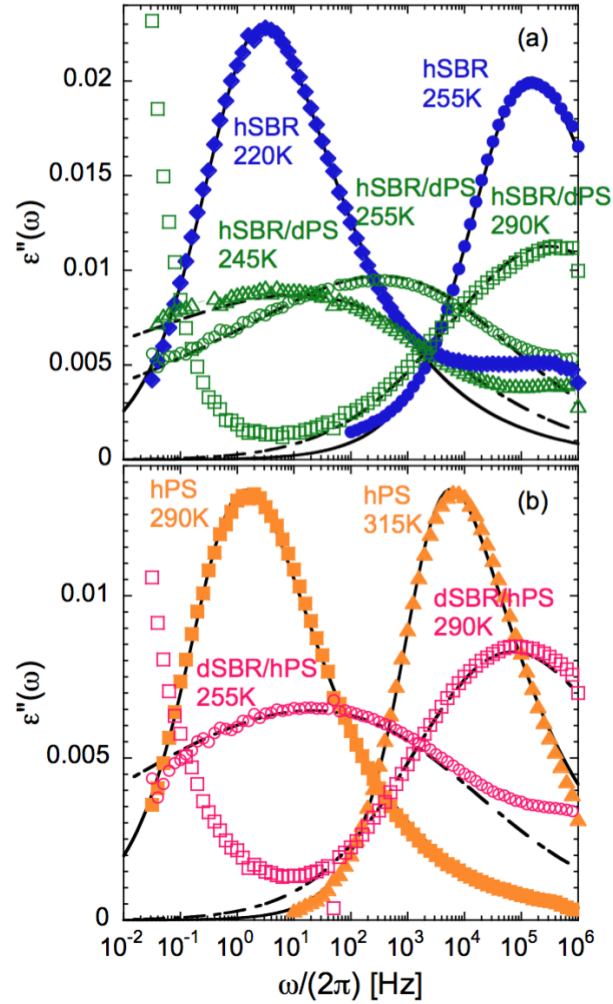
Figure 3.23: (a) Frequency dependence of the dielectric loss at 220 and 255 K for hSBR and for the blend hSBR/dPS at 245, 255 and 290 K. (b) Frequency dependence of the dielectric loss at 290 K and 315 K for hPS and for the blend dSBR/hPS at 255 and 290 K. In both panels, the solid lines stand for the fit of the pure polymers results (filled symbols) by means of the Havriliak-Negami equation (Eq. 2.12) and the dashed-dotted lines for the fit of the blends data (empty symbols) by means of the model proposed (see the text).
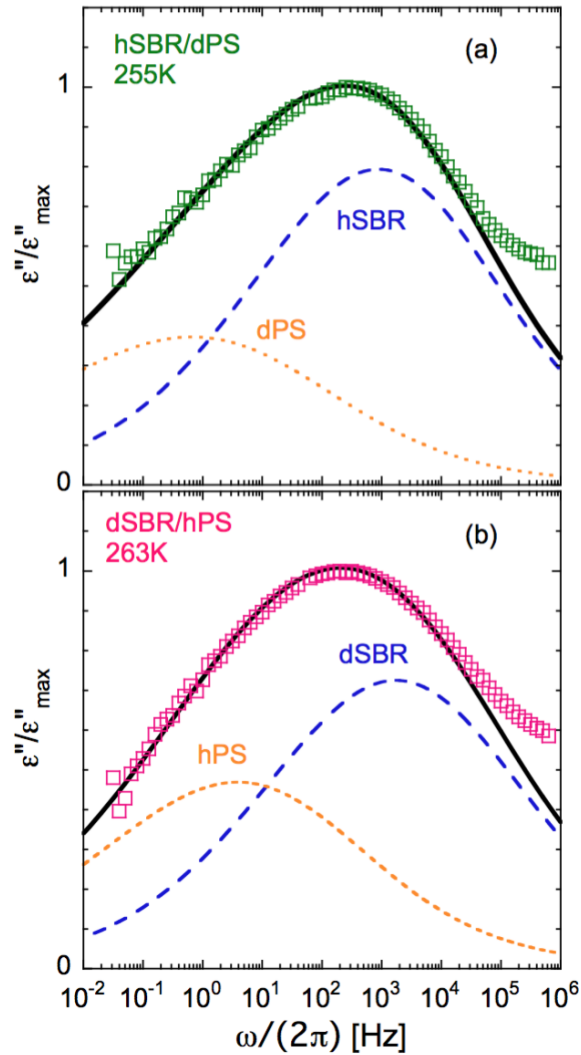
Figure 3.24: Normalized imaginary part of the dielectric permittivity for hSBR/dPS at 255 K (a) and dSBR/hPS at 263 K (b) as function of frequency. Solid lines stand for the fit by means of the proposed model. The contribution of each blend component is shown as dashed (SBR) and dotted (PS) lines.

The average T_0-values of the two components differ in about 20 K for both blends, translating in a clear dynamic heterogeneity in the mixture. From the above approach the resolved contributions of both components in the blends can be obtained, as shown in Fig. 3.24 (dashed and dotted lines). The resulting temperature dependence of the peak relaxation times of the SBR and PS components in each blend is included in Fig. 3.20 as dashed and dotted lines

Table 3.2: Parameters describing the fragility and the distribution function of VFT temperatures of each component in the blends. The corresponding values of the distributions of effective glass-transition temperatures are also included (see text)

Component c	D^c	$\langle T_0^c \rangle$[K]	σ_0^c[K]	$\langle T_{g,eff}^c \rangle$[K]	σ_g^c[K]
hSBR in hSBR/dPS	8.6	184.0	9.0	236.3	11.6
dPS in hSBR/dPS	7.6	203.5	7.0	248.7	8.6
dSBR in dSBR/hPS	8.6	187.0	9.0	238.8	11.5
hPS in dSBR/hPS	7.6	207.0	7.0	253.6	8.6

respectively. The dynamic heterogeneity is patent when these peak characteristic times are resolved, leading to vitrification at different temperatures for each of the components, i. e., different effective glass transitions. Conversely, the influence of concentration fluctuations is mainly reflected in the width of the T_0-distribution, which is slightly larger for SBR compared with PS (see Table 3.2).

As commented above, the underlying distributions of VFT-temperatures also naturally imply distributions of the effective glass-transition temperatures of the blend components $g^c(T_{g,eff})$ given by $g^c(T_{g,eff}) = h^c(T_0)\frac{dT_0}{dT_{g,eff}}$. To obtain these functions, a connection between the VFT temperature and the glass-transition temperature has to be invoked. Since the value of the VFT temperature determines the characteristic time, what is needed is to establish the value of the characteristic time of the α-relaxation at the glass-transition temperature $\tau_g = \tau(T_g)$. Often, this time has been assumed to be $\tau_g \equiv 100$ s. [6] However, this value changes from sample to sample, and also depends on the technique and the criterion used for determining T_g. [50] For instance, for pure hSBR and hPS we found that the relationship between the dielectric α-relaxation time and the calorimetric T_g (defined as the inflection point in the DSC traces) is: $\tau_g^{hSBR}(T_g) = 1.4$ s and $\tau_g^{hPS}(T_g) = 47$ s (see Table 3.1). One possible approach is to assume that in the blend these relationships still hold. Then, the distribution of effective glass-transition temperatures can be easily calculated:

$$g^c(T_{g,eff}) = \frac{\ln(\tau_g^c/\tau_0)}{D^c + \ln(\tau_g^c/\tau_0)} h^c(T_0) \tag{3.8}$$

Since the $h^c(T_o)$ functions are assumed to be Gaussian, $g^c(T_{g,eff})$ are also Gaussian functions, with the values of the average $\langle T_{g,eff}^c \rangle$ and variance σ_g^c given by $\langle T_0^c \rangle[D + \ln(\tau_g^c/\tau_0)]/\ln(\tau_g^c/\tau_0)$ and $\sigma_0^c[D + \ln(\tau_g^c/\tau_0)]/\ln(\tau_g^c/\tau_0)$ respectively (see Table 3.2). These $g^c(T_{g,eff})$ functions are broader than the corresponding $h^c(T_0)$ ones, and their average values are separated by ≈ 12 K for the hSBR/dPS blend components and by ≈ 15 K for the hSBR/dPS blend components. They have been represented in the lower parts of Figs. 3.22(a) and (b). We note that the simple addition of the distributions is not expected to reproduce the observed derivative of the heat flow; nevertheless, this comparison is very instructive to

show the robustness of our approach and the good agreement between its results and independent measurements from different techniques: as can be seen, the calculated distributions span over the entire range where the experimental DSC signals of the blends reflect glass-transition phenomena.

Now we consider the selective microscopic information on proton motions provided by the neutron scattering experiments. In Fig. 3.4 we see that, at a given temperature, the effective mean squared displacement of the SBR protons is significantly larger than that of the PS protons. The increase of the atomic displacements is due to both, vibrational motions and dynamics associated to molecular mobility at different levels (rotations of side groups, localized motions involved in the secondary relaxations, the structural relaxation, and overall chain dynamics). Depending on the temperature, some of these processes are either completely frozen or, at least, slow enough to lead to contributions resolvable by the QENS instrument. Vibrations are naturally active at all the temperatures and are in fact the source of the small increase of the effective mean squared displacements observed below 100 K. The increase of the slope in this temperature range has to be attributed to the onset of localized motions of small portions of the chains including atoms at the main-chains and/or in the phenyl rings in the glassy state, as those responsible for the secondary relaxations detected by other techniques. In the glassy state, a larger mobility is expected for the atoms located at butadiene units than for those at the styrene monomers. As it has been mentioned above, the dielectric signal of SBR contains a β-process that reflects the local motions involved in the cis 1,4-butadiene component of this polymer. These motions obviously contribute to the increase of the proton mean square displacement monitored by the EFWS experiments. Regarding PS, QENS investigations [12] on the glassy dynamics of this polymer revealed small amplitude oscillations of increasing amplitude with temperature as the main motions undergone by phenyl rings. These dynamical processes seem to be also active in the blend components. As it has been shown for other polymeric mixtures, the local motions undergone in the glassy state are not appreciably affected by blending [18].

At higher temperatures, an abrupt change in the slope of the effective mean squared displacement (see Fig. 3.4) is a signature of the glass-transition. We note that in the case of labelled samples like those here investigated, the calculation of the mean squared displacements is particularly subjected to uncertainties, due to coherent contaminations as previously mentioned. Therefore, to identify this transition we have directly calculated the temperature derivative of the measured elastic intensity function at 0.6 Å^{-1}, where the coherent contribution is low. Figure 3.25 shows the obtained results for the two blends investigated. This function shows always negative values –according to an increase of the mean squared displacement with increasing temperature. It displays a clear change in slope that reflects the start of the 'softening' of the component followed by the neutron scattering measurements. It occurs at about 220 K for hSBR in the hSBR/dPS blend and at about 240 K for hPS in the dSBR/hPS mixture. We can compare now these results with the distribution $g^c(T_{g,eff})$ for component c independently deduced from the above analysis of the BDS and QENS results.

These functions are represented in Fig. 3.25 for the two components of the blends which are followed in the EFWS experiments. As can be appreciated, the kink in the EFWS derivative coincides with the temperatures at which $g^c(T_{g,eff})$ starts to present significant values. Thus, through its derivative, the elastic scans provide a microscopic probe to determine the onset of the effective glass-transition range of the labelled component in the blends.
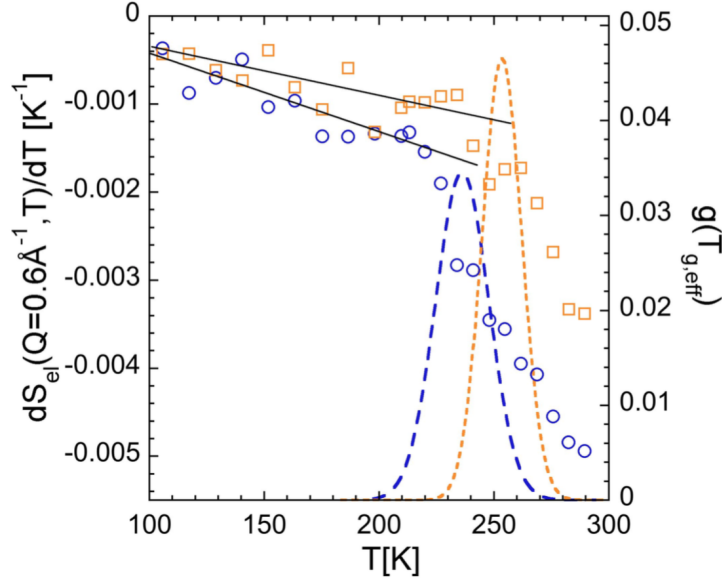
Figure 3.25: Derivative of $S_{el}(Q{=}0.6$ Å^{-1},T) with respect to temperature for the two blends investigated (circles: hSBR/dPS sample, squares: dSBR/hPS sample). The lines represent the deduced distributions of effective glass-transition temperatures for each of the components followed by the neutron scattering experiments.

On the other hand, regarding the comparison between dielectric and neutron scattering results, we note a significantly smaller value of $Q^\star$ for hPS than for hSBR. The meaning of the $Q^\star$ is not yet fully understood. In the case of a simple diffusive process, a simple approach based on molecular hydrodynamics and a molecular treatment of dielectric results allowed expressing $Q^\star$ in terms of a many body magnitude –a generalized Kirkwood parameter– and a single molecule magnitude –the hydrodynamic radius [9, 45]. The generalization to the case of polymeric materials showing anomalous diffusion is not straightforward, as recently shown [8]. A connection of $Q^\star$ with structural parameters like the position of the inter-main-chain correlation peak of the structure factor, Q_{max} was also explored in that work. Main-chain polymers (without side groups) or polymers with only methyl groups as side groups present rather similar values of $Q^\star \approx 0.9$ A^{-1} independently of the value of Q_{max}. However, for polymers with bulkier side groups, a correlation between $Q^\star$ and Q_{max} which is close

to their equivalence $Q^\star = Q_{max}$ can be deduced, within the uncertainties. Actually, the case of PS fits in that framework. Moreover, some microscopic information can be inferred from a phenomenological analysis. Since applying the Gaussian approximation it can be deduced that $\langle r^2(t = \tau_{max}^{DS})\rangle = 6/Q^{\star 2}$, [9] the finding of a small value of $Q^\star$ suggests that atoms in PS need to reach large displacements to fully relax dipoles in the α-relaxation process.

We finally consider the information provided by the QENS experiments on both the stretching and deviations from Gaussian behavior of the incoherent scattering function of the protons of the polymers. In principle, it could be expected that the presence of concentration fluctuations in the blend would give rise to more stretched functional forms and stronger deviations from Gaussian behavior than in the corresponding homopolymers, and that these effects would become more pronounced with decreasing temperature. As shown in Figs. 3.7 and 3.8, for a given temperature the effect of blending on SBR is to amplify the stretching. However, no significant impact on the Gaussian behavior is found, within the experimental uncertainties. For PS, at the temperature where data on the homopolymer have been recorded, we observe that both, stretching and non-Gaussian effects, become weaker upon blending with SBR (Figs. 3.8 and 3.9), contrarily to the a priori expectations. As previously pointed out, for a given temperature the PS component in the blend shows more pronounced stretching and non-Gaussian effects than the SBR component; also, its characteristic time is markedly longer.

Stretching and non-Gaussian effects following from heterogeneities tend to become weaker with increasing temperature due to the homogeneization of the molecular motions of the system with increasingly fast associated characteristic times. This is expected to happen already in homopolymers, and in fact it is the case here reported for hSBR, for which QENS data are available at different temperatures (Figs. 3.7 and 3.8). The faster the motions, the narrower becomes the distribution of characteristic times and consequently the closer to Gaussian is the probability distribution function of atomic displacements. Therefore, a suitable parameter to characterize the state of the system and compare different situations for different samples is using the characteristic time (isochronal representation). In Fig. 3.26 we have used as key variable the QENS relaxation time at a representative Q-value, namely $Q^\star$, to compare the stretching and non-Gaussian effects of the protons in the different components and/or conditions. In this representation, we observe that the behavior is practically independent of the particular environment and temperature of the sample. For a given value of $\tau(Q^\star)$, all data show similar values, within the uncertainties, for both β and $\beta \cdot b$ parameters.
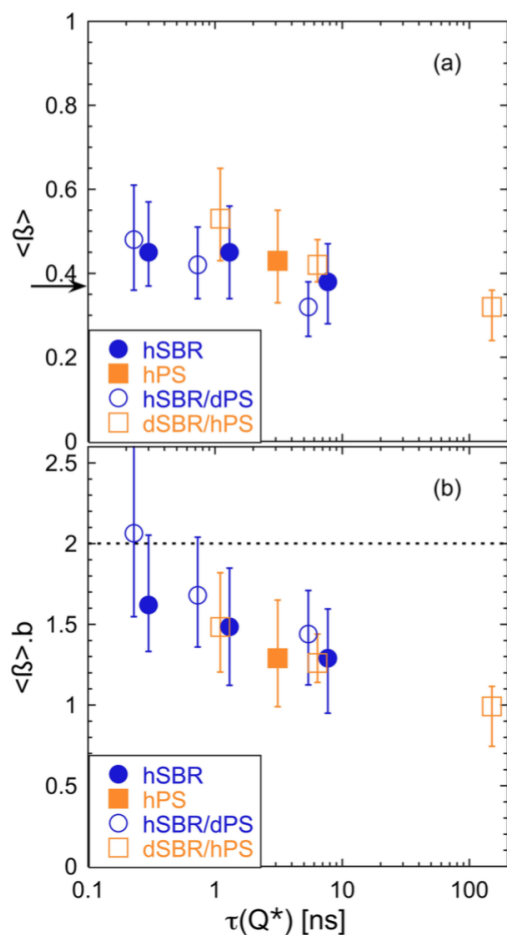
Figure 3.26: Data shown in Fig. 3.8 are represented here as function of the characteristic time at $Q^\star$.

The reason for these observations could be the intrinsic particularly marked heterogeneous and non-Gaussian behavior of the PS and SBR homopolymers. QENS is sensitive to atomic (protonic) motions, which are expected to be rather different for the diverse hydrogens located either at the phenyl rings or at the main chains. The Q-dependence of the stretching parameter and the large deviations from Gaussian behavior found for both homopolymers could be signatures of such heterogeneous microscopic motions. Being a random copolymer, we note that for SBR the situation is even more dramatic: also at the backbone, a highly heterogeneous dynamics is expected to take place since the atoms in the butadiene units would present an enhanced mobility with respect to the main-chain styrene atoms. In the high-temperature range investigated by QENS, the distributions of mobilities induced by concentration fluctuations in the blends

$G(\log \tau) = h(T_0)\frac{dT_0}{d\log(\tau)}$ are expected to be relatively narrow as can be observed in Fig 3.27.
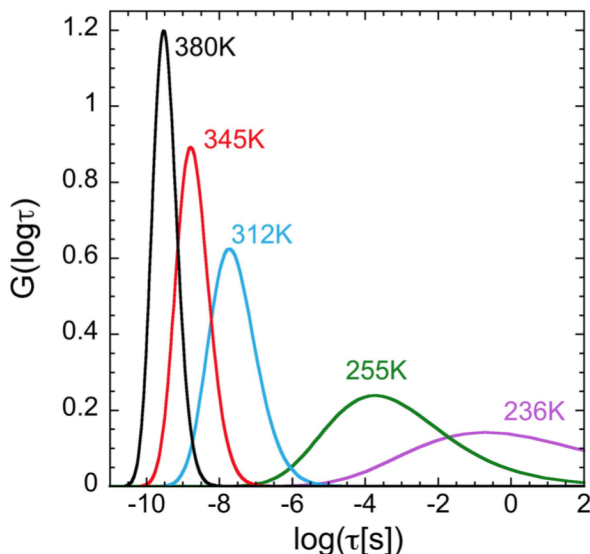
Figure 3.27: Distribution function of segmental relaxation times of SBR originated by concentration fluctuations in the blend hSBR/dPS deduced from the BDS and QENS analysis. The function is shown for different temperatures including those investigated by QENS on the blend samples.

Therefore, the main effect of blending at such high temperatures is to modify the overall timescale of the molecular motions, and the observed stretching and non-Gaussian behavior obey primarily to those intrinsically present in the homopolymers in an isochronal situation.

We note that in the analysis of experimental QENS results on polymers, the stretching of the α-relaxation contribution is usually assumed to be Q-independent. Some molecular dynamics (MD) simulations results have explored its possible variation with Q, in particular in the framework of the applicability of the Mode Coupling Theory (MCT). It is found that there is a tendency of the β-value to decrease with increasing Q, reaching asymptotic values of 0.24 (polybutadiene, PB) [24] or 0.35 (poly(vinyl methyl ether), PVME) [17] at high Qs. In the Q-range here investigated, the Q-variation of the β-values of the polymers (both, in the homopolymer and in the blend samples) is stronger than those found from MD-simulations in the above commented works. High-Q asymptotic β values even smaller than those reported for PB and PVME would be expected for SBR and PS, underlining the role of the dynamic arising from their complex microstructures.

3.3 Conclusions

In this work we have shown that the concepts and methodologies developed for the investigation of blend dynamics in systems composed of relatively simple homopolymers can be transferred to other more complex mixtures, particularly to a simplified industrial system involving the mixture of a random copolymer, SBR, with an oligomer, PS. The main conceptual ingredients are dynamic heterogeneity and concentration fluctuations, and the methodology involves the combination of different experimental techniques including DSC, BDS and QENS. As a part of this methodology, the investigation by neutron scattering techniques of isotopically labelled samples was a requirement in order to isolate the response of one of the components in the mixture. This yield to face the problem of comparing results from samples which are not exactly equivalent. We have shown that thanks to the combination of neutron scattering techniques (sensitive to the isotopic details) with dielectric relaxation data (where the isotopic labeling should not play a role) covering a broad frequency range, a complete description of the segmental dynamics *of the two* polymer components in a complex mixture was possible. In this way, we resolved the fragility of the two components in the blend and identified the distribution of effective glass-transition temperatures of each blend component that nicely match the whole glass-transition range of the mixture as determined by DSC. The agreement is also good for each individual component when the distribution of effective glass-transition temperatures is compared with the corresponding EFWS neutron scattering results. This suggests the possibility of using EFWS as a direct way to determine the onset of the effective glass transition of the components of a mixture.

Finally, since in the high-temperature range accessed by QENS the distributions of mobilities induced by concentration fluctuations are expected to be narrow, the observed stretching and non-Gaussian behavior of the scattering function can be attributed to the intrinsically heterogeneous microscopic motions occurring in these relatively complex polymeric chains.The characterization of concentration fluctuations in these systems can be carried out by small angle neutron scattering experiments. These measurements and their connection with the dynamic response are presented in Chapter 5.

Chapter 4

Modeling the effect of concentration on the segmental α-relaxation of SBR/PS blends.

The aim of this chapter is to extend the study presented in the previous chapter and establish a predictive dielectric model for SBR/PS blends in a wide range of concentrations. For this purpose, blends of SBR and polystyrene from 10 wt%PS and up to 70 wt%PS have been characterized. However, the homopolymers analysed present different microstructures respect to the ones analysed in the previous chapter. The polymers used in this chapter are those identified as hSBR1 and hPS1 in Table 2.1 where the sample characteristic are given. Therefore, a full characterisation by means of Differential Scanning Calorimetry and Broad Band Dielectric spectroscopy has to be performed prior to deal with the dielectric modelling of the blend.

4.1 Experimental results

4.1.1 a. Differential Scanning calorimetry

In this part, the results obtained by means of differential scanning calorimetry (DSC) for the pure component as well as the SBR/PS blends are presented. Figure 4.1 shows the evolution of the reversible heat flow in function of the temperature determined by DSC during cooling at 3K/mn for the different blends and both homopolymers investigated. The glass transition caused a baseline shift of the signal which becomes broader as we increased the amount of polystyrene into the blend. As observed in the previous chapter for the other set of sample, the glass-transition processes of the blends manifest as broad

features in the range between the $T_g s$ of the pure components. Moreover, it is now well established that each of the components display a different segmental relaxation in the blend. In the previous chapter we demonstrated that this is also the case in the SBR/PS system. The corresponding effective $T_g s$ are usually difficult to be resolved in the DSC traces. Therefore, to a first approximation, we have characterized the DSC results in the blends in the same way as in the homopolymers, namely by determining the inflection point.

Sample	T_g(K)
hSBR1	227
90/10	231
80/20	234
70/30	238
60/40	244
50/50	254
40/60	258
30/70	268
hPS1	305
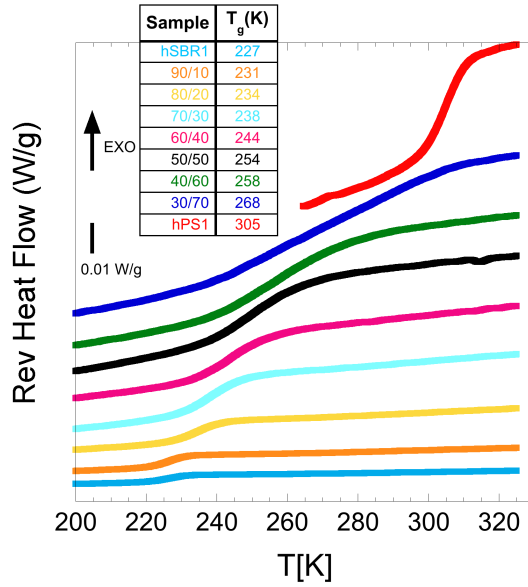
Figure 4.1: Reversible heat flow during cooling at 3 K/min for the samples investigated. The glass transition temperatures determined by taking the inflection point are specified for each sample.

Figure 4.2 shows the evolution of the glass transition temperature (inflection point) for the different blends as well as the pure components. The glass transition temperature decrease monotonously when adding SBR into the blends from that of hPS1 (303K) to that of hSBR1 (225K). For a binary system, the Fox equation 4.1 relates the T_g expected for the ideal blends with the T_g of the pure components.

$$\frac{1}{T_g^{Blend}} = \frac{\varphi}{T_g^{SBR}} + \frac{(1-\varphi)}{T_g^{PS}} \tag{4.1}$$

where φ is the weight fraction of SBR.

95
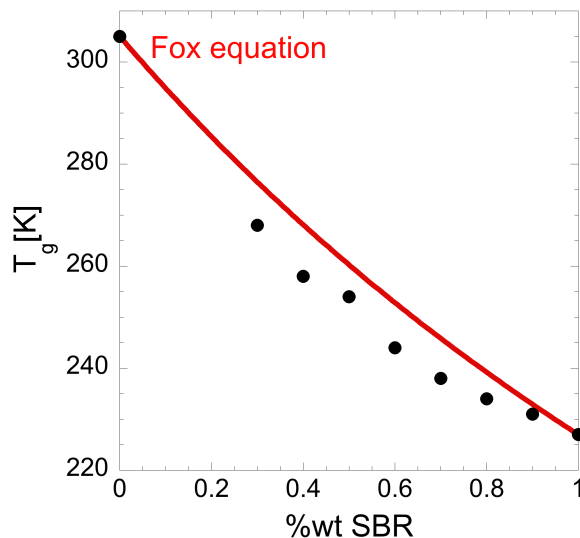
Figure 4.2: DSC results for the SBR/PS blends as a function of the amount of SBR in the blend. Dots represent experimental results. Red solid line represents the behaviour predict by the Fox equation for binary polymer blends.

As it is usually reported in the literature for amorphous polymer blends, we observed that our samples deviates from this calculated values, showing a stronger curvature than the behaviour predict by the Fox Equation. This is usually interpreted in relation with interactions between the two components of the blend. However, this could also be due to the presence of two effective $T_g s$ in the blend, corresponding to each component in the blend which make difficult to define a single value of T_g for a given composition. The model here presented take into account the fact that, each component behave differently in the blend, following the behaviour of the pure corresponding homopolymers.

4.1.2 b. Dielectric Spectroscopy

Pure components

In this section the dielectric characterisation of the pure components is presented.

Figure 4.3 shows representative examples of the frequency dependence of the dielectric loss peak $\varepsilon''(\omega)$ for the pure polymers. We observed a mean loss peak attributable to the segmental dynamics (α-relaxation) which peak's position is strongly affected by the temperature. In agreement with the Differential

Scanning Calorimetry results, the dielectric peaks of the homopolymers are centred at similar frequencies at much lower temperature for SBR than PS. Also, as reported in the previous chapter for the other SBR/PS system from the peak values of the dielectric permittivity losses it can also be seen that SBR has a stronger dielectric relaxation than PS.
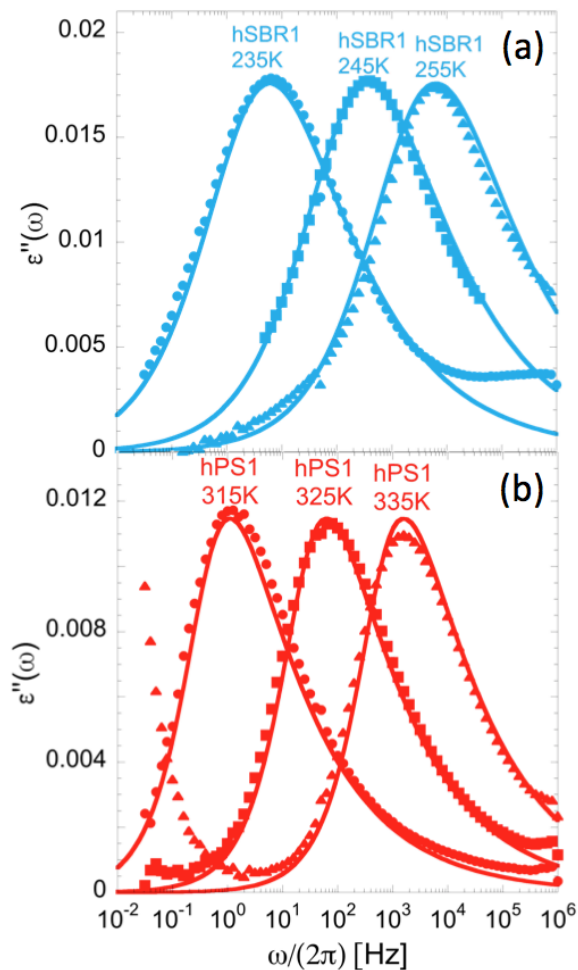
Figure 4.3: (a) Frequency dependence of the dielectric loss at 235, 245 and 255K for hSBR1. (b) Frequency dependence of the dielectric loss at 315, 325, 335K for hPS1. In both cases, the solid lines stand for the fit by means of the Havriliak-Negami Equation (see Eq. 2.12).

Figure 4.4 shows the temperature dependence of the characteristic time scales, defined as the inverse of the angular frequencies at the dielectric loss maxima $(\tau_{max} = \omega_{max}^{-1})$ of the α-relaxation process for the pure polymers. The

Table 4.1: Parameters involved in the VFT description of the characteristic times shown in Fig. 4.4 with $\tau_0 \equiv 10^{-13}$ s. The dielectric strength and Havriliak-Negami parameters obtained fitting the curves well centered in the experimental frequency window are also given.

Sample	$T_0(\mathbf{K})$	**D**	$\Delta \varepsilon$	α	γ
hSBR1	176.9 ± 2.9	8.6 ± 0.5	0.095 ± 0.004	0.57 ± 0.03	0.526 ± 0.03
hPS1	256.5 ± 3.2	6.3 ± 0.4	0.048 ± 0.002	0.84 ± 0.008	0.37 ± 0.008

lines corresponds to the description by means of the VFT equation. In the fits we kept constant the prefactor value $\tau_0 = 10^{-13}s$ in the Vogel-Fulcher-Tamman equation (Eq. 1.9). The values obtained for the fragility parameter D and T_0 are displayed in Table 4.1. With regards to the shape of the relaxation curves, as usual, the results on the pure polymers can be well fitted by mean of the Havriliak-Negami equation (see Eq.2.12) already presented in previous chapters. It was possible to obtain good description of the data over all the temperature range investigated. The different Havriliak-Negami parameters are resumed in Table 4.1.
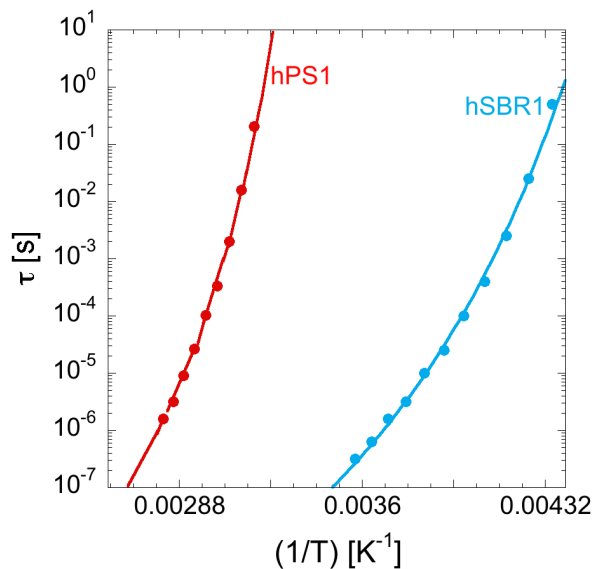
Figure 4.4: Temperature dependence of the characteristic times defined from the inverse of the frequencies of the dielectric loss maxima for the α-relaxation process of the different samples investigated. The lines correspond to descriptions by means of the VFT equation (Eq. 1.9) with $\tau_0 = 10^{-13}$s.

As previously mentioned, the segmental α-relaxation is usually well described by means of the Havriliak-Negami equation. However in order to im-

prove the description of the experimental data, the contribution of the SBR's β-relaxation has been modelled using a Gaussian function. Therefore, the dielectric loss corresponding to the contribution of the SBR β-relaxation can be expressed as:

$$\varepsilon_\beta^{''}(log_{10}(\omega)) = A_\beta \times exp\left[-\frac{1}{2}(\frac{(log_{10}(\omega) + log_{10}(\tau_\beta)}{\sigma_\beta})^2\right] \qquad (4.2)$$

where the amplitude is

$$A_\beta = \frac{5.65 \times 10^{-3}}{\sigma_\beta} \qquad (4.3)$$

the parameters σ_β accounting for the broadness of the peak is

$$\sigma_\beta = -0.785 + \frac{553.7}{T} \qquad (4.4)$$

and the variation of the characteristic time in function of the temperature (T) can be written as:

$$\tau_\beta/s = 2.1 \times 10^{-15} \times exp[\frac{4033}{T}] \qquad (4.5)$$

Figure 4.5 shows the dielectric loss for the SBR sample at low temperatures where the peak corresponding to the β relaxation process is well center in the experimental window. As can be observed, a good description of the data is obtained using the equation 4.2.
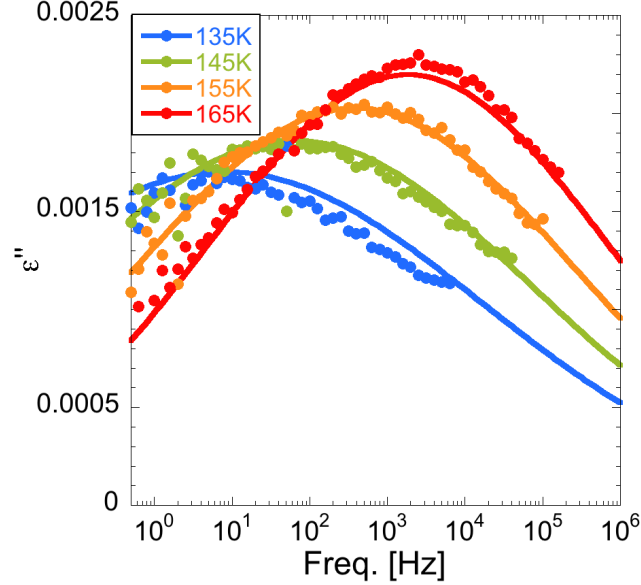
Figure 4.5: Dielectric loss of hSBR at four temperatures well below the glass transition temperature of the sample where the β-relaxation process can be appreciated. Solid lines stand for the fits by means of Eq.4.2.

The α and β-relaxation can be then well described over all the temperature range for the SBR sample. Therefore, the total dielectric loss can be written as:

$$\varepsilon_{SBR}^{''}(\omega) = \varepsilon_{\beta}^{''}(\omega) + \varepsilon_{\alpha}^{''}(\omega) \tag{4.6}$$

where the term corresponding to the α-relaxation is :

$$\varepsilon_{\alpha}^{''}(\omega) = -Im\left\{\frac{\Delta\varepsilon}{[1 + (i\omega\tau_{HN})^{\alpha}]^{\gamma}}\right\} \tag{4.7}$$

and the parameters $\Delta\varepsilon$, α, γ are the ones corresponding to hSBR1 given in Table 4.1.

Figure 4.6 shows an isochronal dielectric representation for the SBR component. In an isochronal representation we look at the evolution of the dielectric output at fixed frequency, which are here 10^3 and 10^7Hz. Figure 4.6 shows the dielectric loss in function of the temperature for the pure SBR sample where we can clearly detect a β and an α relaxation for SBR. At 10^3Hz the two different processes give rise to two peaks well defined and separated one from another. The peak centered at lower temperature being the one corresponding

to the β relaxation. Regarding the application of this study, in order to measure the high frequency dielectric properties of our samples, the high frequency dielectric spectroscopy instrument setup was used. At 10^7Hz the two relaxation processes merge giving rise to a broad single peak. The high frequency dielectric data present a scaling factor due to some geometric differences between the two different experiments. In Figure 4.6 the solid lines stand for the fits of the experimental data by means of Eq. 4.6. As can be observed a very good description of the experimental data is obtained. However some more discrepancies are observed at 10^7Hz which is due to the fact that the dielectric parameters ($\Delta\varepsilon$, α, γ) are being fixed to values that permit to optimised the description of the BDS data. However a good general description of the experimental data is obtained over all the extended frequency range, allowing in the following to construct a simple dielectric model for the blends.
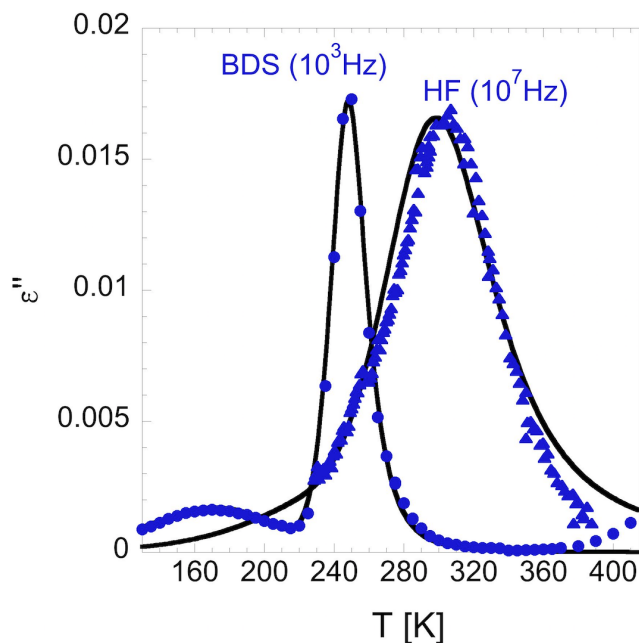
Figure 4.6: Representative dielectric spectra of the pure SBR polymer. The dielectric loss $(\varepsilon^{''})$ is plotted as a function of temperature at 10^3 and 10^7Hz respectively measured by Broadband Dielectric Spectroscopy (BDS) and with the High Frequency Dielectric instrument setup (HF). Solid lines stands for the description of the hSBR1 experimental data using Eq. 4.6.

SBR/PS blends

In this part, the results obtained by dielectric spectroscopy for the blends are presented.

Figure 4.7 shows the dielectric loss $(\varepsilon^{''})$ as a function of the temperature for

the different samples where we can clearly detect a β and an α-relaxation for the SBR and the representative blends. The polystyrene sample only presents an α-relaxation. From the shape and the position of the peaks, it is clear that the α-relaxation is strongly affected by blending. As we add polystyrene in the blend, a broader and slower α-relaxation is observed compared to that of the pure SBR. However within the experimental errors and as it was reported in the literature for other polymers [18], the β-relaxation does not seems to be affected by blending. Moreover regarding the industrial applications that Michelin is interested in, in the following we will focus on the α-relaxation.
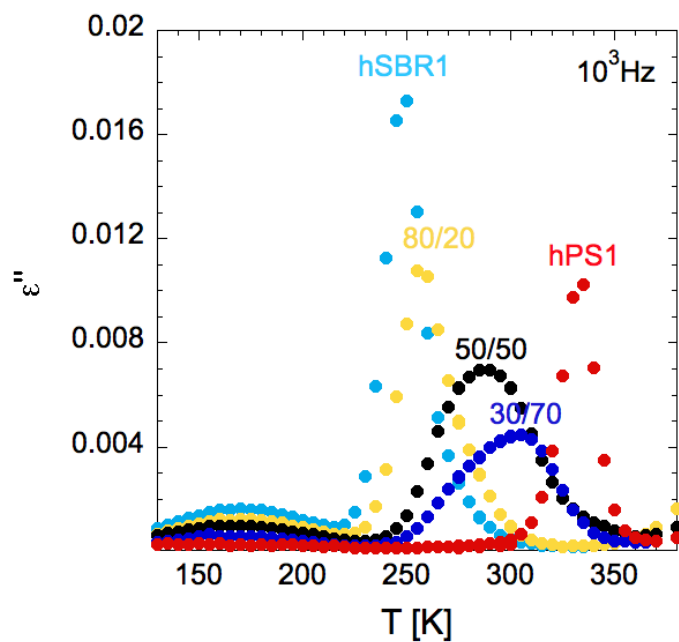
Figure 4.7: Representative dielectric spectra of the pure component and representative blends with respectively 80 wt%, 50 wt%, and 30 wt% of SBR. The dielectric loss ($\varepsilon^{''}$) is plotted as a function of temperature at $10^3 Hz$.

Figure 4.8 shows the α-relaxation at about 25K above the glass transition temperature of each sample.
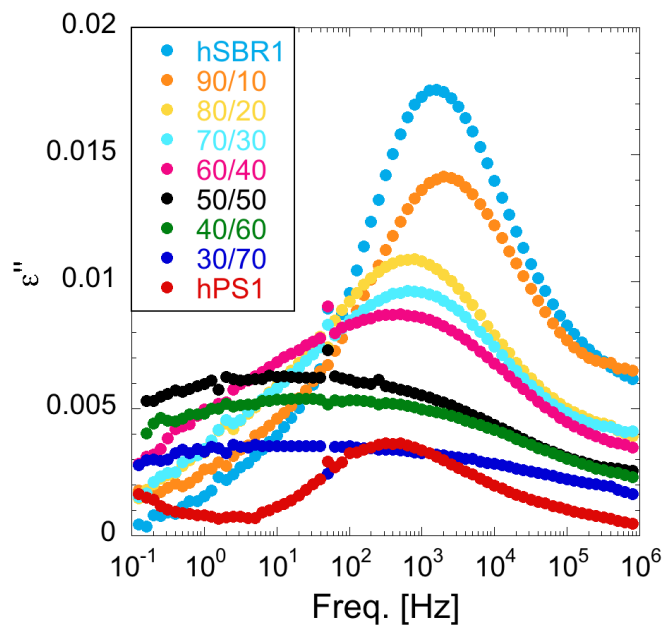
Figure 4.8: Dielectric loss ($\varepsilon^{''}$) of the α-relaxation for SBR/PS blends and the pure components at $T \approx Tg + 25K$ as a function of frequency.

We observe a broadening of the relaxation times distribution by adding PS into the blends, and a dramatic broadening of the relaxation peak is observed by adding 50 wt% of PS or more. As can be seen Figure 4.1, for these high amounts of PS into the blends a broad glass transition temperature is also observed by means of Differential Scanning Calorimetry.

4.2   Dielectric Modelling

As previously observed in the experimental data, the segmental dynamics of the two components in the blend is strongly modified depending on both the composition and the interactions between the components, resulting in properties not observed in the pure components [27]. In the case of binary miscible polymer blends, as it has been demonstrated in the previous chapter, blending affect the α-relaxation by producing a broadening of the relaxation and dynamic heterogeneity [24]. In this part, the dielectric model based upon the theoretical concepts detailed in the previous chapter, such as thermally driven concentration fluctuations and self concentration, is presented.

4.2.1 Modeling the dielectric behaviour of SBR/PS blends

As previously mentioned in chapter 4, the presence of statistical thermal concentration fluctuations produces a distribution of concentration $g(\varphi_i)$ around φ, the bulk concentration. The total dielectric permittivity of the blend can be then written as:

$$\varepsilon^*(\omega) = \sum_i g(\varphi_i) \times \varepsilon_i^*(\omega) \tag{4.8}$$

As can be observed in the Figure 4.9, the macroscopic sample can be divided in sub-volume i. Each sub-volume can be characterised by a given composition $(\varphi_i^{SBR}, \varphi_i^{PS})$ and a Vogel temperature (T_0^{SBR}, T_0^{PS}) associated to each component in the blend.
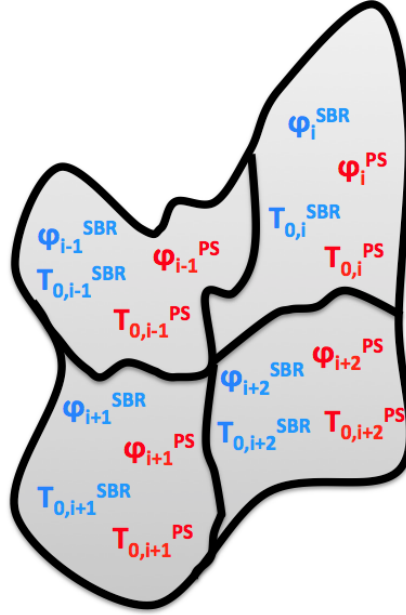
Figure 4.9: Schematic representation of the different sub-volumes composing the macroscopic blend. Each sub-volume contains both SBR and PS components.

The dielectric permitivity can be written in each sub-volume of composition φ_i as:

$$\varepsilon_i^*(\omega) = \varepsilon_{i,c1=SBR}^*(\omega) + \varepsilon_{i,c2=PS}^*(\omega) \tag{4.9}$$

The distribution of concentration around φ, the bulk concentration of SBR in the blend, is assumed gaussian, which leads to:

$$g(\varphi_i) \propto exp^{\frac{-(\varphi_i-\varphi)^2}{2\sigma^2}} \tag{4.10}$$

where the proportionality constant must satisfy the distribution function normalisation.

As already mentioned in the experimental results the Havriliak Negami equation allows a very good description of the dielectric loss of the pure components over all the temperature range investigated (see Figure 4.3). The Havriliak Negami parameters that define the shape of the dielectric loss are taken from the pure components and assumed to be unaffected by blending. These parameters can be found in Table 4.1.

The temperature dependence of the characteristic time scales corresponding to each component in the sub-volume of composition φ_i can be expressed as:

$$\tau_{i,c}(T) = \tau_{0,c} \times exp \left[\frac{D_c \times T_{0,i}^c}{T - T_{0,i}^c} \right] \tag{4.11}$$

Here we assumed that the fragility parameter D of each component is the same in all sub-volumes, which means that D do not depend significantly of concentration.

For hSBR1, the fragility and pre-factor of the Vogel-Fulcher-Tamman equation are taken from the pure component and we also assumed that they are unaffected by blending. For PS, the pre-factor is considered unaffected by blending, but we allow the fragility to change in the blend with respect to the pure component as it has been well documented in the literature that the higher T_g component see is fragility affected by blending. [3, 29] Following the results of chapter 4, the fragility of hPS1 in the blend has been then fixed to $D_{PS/Blend} = 7.6$

In order to evaluate $\tau_{i,c}(T)$ the Vogel-Temperature in each sub-volume $T_{0,i}^c$ as to be determined. To do so, as mixture rule, a Flory-Fox equation of Vogel temperatures have been applied for each component in the blend [38] [31], leading to:

$$T_{0,i}^{SBR} = \frac{T_0^{SBR} \times T_0^{PS}}{\varphi_{eff,i}^{SBR} \times T_0^{PS} + (1 - \varphi_{eff,i}^{SBR}) \times T_0^{SBR}} \tag{4.12}$$

$$T_{0,i}^{PS} = \frac{T_0^{SBR} \times T_0^{PS}}{1 - \varphi_{eff,i}^{PS} \times T_0^{PS} + (\varphi_{eff,i}^{PS}) \times T_0^{SBR}} \tag{4.13}$$

As previously explained, we introduce an effective concentration $\varphi_{eff,i}$ describing the fact that the dynamics of a given polymer segment in a miscible blend is controlled by the local composition in small region around the segment. This makes the concentration of each specific component to be higher than the average in this region, this effect being reflected by the corresponding self-concentration parameter. Thus, the local region around a SBR (respectively PS) chain (not near a chain end) has an effective concentration that can be expressed as:

$$\varphi_{eff,i}^c = \varphi_s^c + (1 - \varphi_s^c) \times \varphi_i^c \tag{4.14}$$

105

We can then write the dielectric loss for each component in the blend as :

$$\epsilon''_{SBR/Blend}(\omega) = \sum_i \epsilon''_{SBR} \left[\omega \times \tau(T^{SBR}_{0,i}(\varphi^{SBR}_i)) \right] \times g(\varphi^{SBR}_i) \times \varphi^{SBR}_i \quad (4.15)$$

$$\epsilon''_{PS/Blend}(\omega) = \sum_i \epsilon''_{PS} \left[\omega \times \tau(T^{PS}_{0,i}(\varphi^{PS}_i)) \right] \times g(\varphi^{PS}_i) \times \varphi^{PS}_i \quad (4.16)$$

The total dielectric loss of the blend can be obtained by adding the contribution of each component in the blend which leads to :

$$\epsilon''_{Blend}(\omega) = \epsilon''_{PS/Blend}(\omega) + \epsilon''_{SBR/Blend}(\omega) \quad (4.17)$$

The simple dielectric model here presented allows us to describe the dielectric behaviour of the SBR/PS blend with only three parameters. These parameters are σ, φ^{SBR}_s, φ^{PS}_s accounting respectively for thermally driven concentration fluctuation and self-concentration effects.

4.2.2 Dielectric modeling results

In this section we compare the dielectric modeling that has been presented with the experimental dielectric data. This comparison has been performed over a broad range of concentrations, from 30 wt% SBR up to 90 wt% SBR. Figure 4.10 shows the comparison between the experimental dielectric data and the different outputs of the model for the different blends investigated in isothermal conditions at some representative temperatures. As can be observed, in Figure 4.10 the different outputs of the model are also represented using a slightly different vertical scale, which was necessary to match the loss peak intensities. The dielectric behaviour of the blend can be disentangled identifying the contribution of each component in the blend as well as the contribution coming from the β-relaxation of the SBR component. We compare the outputs of the model and the experimental data at three different temperatures where the peak corresponding to the segmental α-relaxation is well observed in the experimental window. As can be observed, the high frequency dielectric signal is mainly dominated by the SBR component also for blends with high concentration in polystyrene. It is also to be underlined that, when comparing the total output of the model (see orange line in Figure 4.10) with the BDS data (empty square in Figure 4.10) a good agreement is obtained over a broad frequency range using only three fitting parameters.
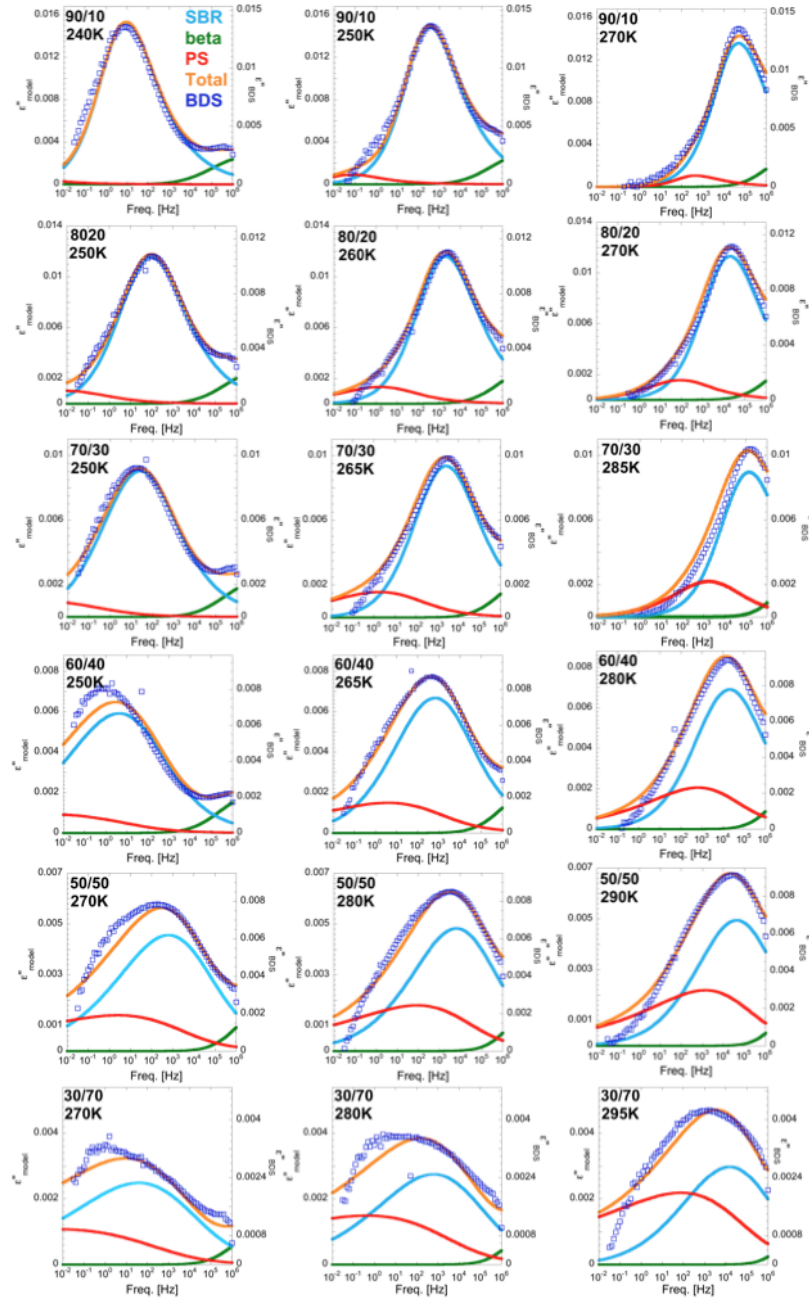
Figure 4.10: Output of the dielectric model compared to the experimental dielectric data. The different blends investigated are presented at three different temperatures where the peak corresponding to the segmental α-relaxation is well observed in the experimental window. Blue empty squares stand for the experimental dielectric data. Solid lines stand for the different outputs of the model.

Table 4.2: Evolution of the dielectric modelling parameters in function of the concentration in SBR in the blend.

wt% SBR in the blend	σ	$\varphi_{s,SBR}$	$\varphi_{s,PS}$
90	0.05	0.40	0.30
80	0.11	0.40	0.27
70	0.14	0.40	0.25
60	0.18	0.32	0.13
50	0.22	0.23	0.13
30	0.25	0.20	0.15

Table 4.2 resumed the fitting parameters used for each sample. At a given composition the fitting parameters are kept constant over all the temperature range analysed.

Figure 4.11 shows the evolution of the fitting parameters in function of the concentration of SBR in the blend. As can be observed in Figure 4.11 the two self concentration parameters increase when adding SBR into the blend. At a given concentration of SBR in the blend, the value found for the self concentration corresponding to the polystyrene component is always lower than the one found for the SBR component. As can be observed, the variance σ of the distribution of concentration decreases when adding SBR into the blend. For the pure components, no extra broadening is expected which leads to $\sigma = 0$ in terms of distribution of concentration.
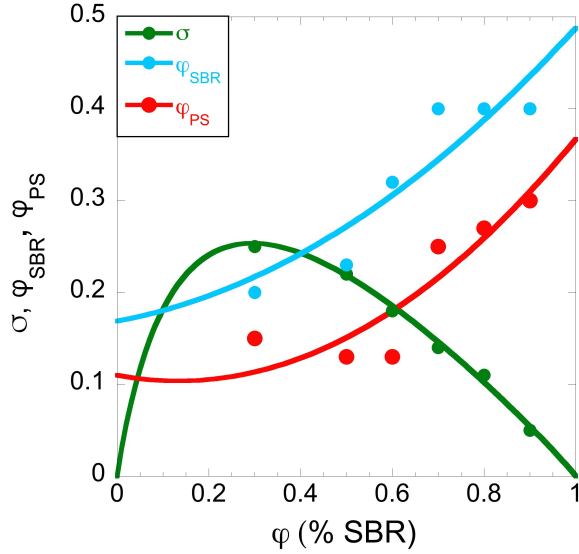
Figure 4.11: Evolution of the model parameters in function of the concentration of SBR in the blend. Solid lines stand for the fit of σ, φ_s^{SBR} and φ_s^{PS} respectively by means of Eq. 4.18, 4.19 and 4.20.

Beside the fact that the φ_s values show high changes, the σ values present a rather smooth variation with concentration. The SBR concentration dependence of the σ, φ_s^{SBR}, φ_s^{PS} parameters can be conveniently described by the following equations (see lines in the Figure 4.11) :

$$\sigma = 0.0366 \times \left[\frac{1}{(1000 \times \varphi)} \times \frac{1}{174 \times (1 - \varphi)} \right]^{1.4} \tag{4.18}$$

$$\varphi_s^{SBR} = 0.169 + 0.093 \times \varphi + 0.226\varphi^2 \tag{4.19}$$

$$\varphi_s^{PS} = 0.11 - 0.093 \times \varphi + 0.35\varphi^2 \tag{4.20}$$

Using these equations, the different values of the fitting parameters could be interpolated at any desirable blend composition.

Figure 4.12 shows the experimental data already presented in Figure 4.7 adding the dielectric model prediction using as σ, φ_s^{SBR} and φ_s^{PS} parameters values the ones predicted using the equations 4.18, 4.19 and 4.20 for a given composition.
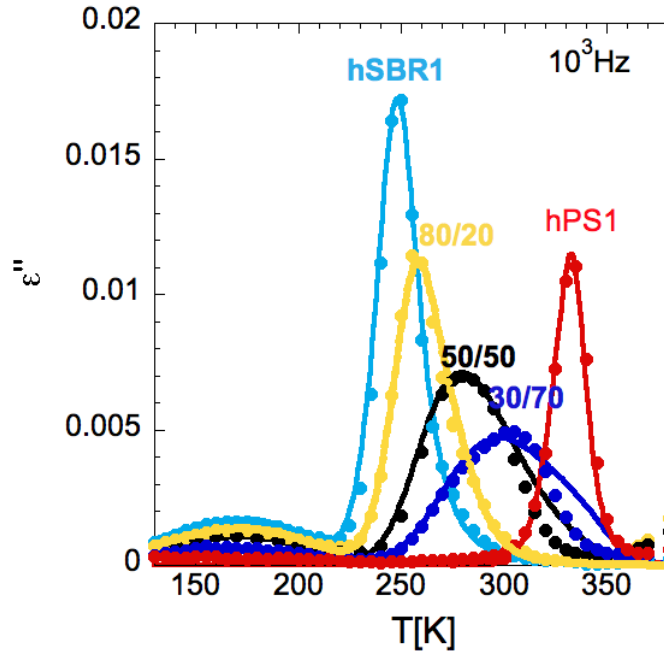
Figure 4.12: Representative dielectric spectra of the pure component and representative blends with respectively 80 wt%, 50 wt%, and 30 wt% of SBR. The dielectric loss ($\varepsilon^{''}$) is plotted as a function of temperature at $10^3 Hz$. The solid lines stand for the dielectric model prediction using as σ, φ_s^{SBR} and φ_s^{PS} values, the ones predicted by using the equations 4.18, 4.19 and 4.20 for a given composition.

As can be observed, for all the samples investigated the description of the peak maximum is very good. Regarding the shape of the dielectric loss for the α-relaxation, a very good agreement is obtained for a blend with 80 wt% of SBR. When adding 50 wt% of SBR or less, the dielectric loss tends to be overestimated at high temperature.

The dielectric modelling presented above can be eventually used for evaluating the dielectric relaxation at any frequency of interest. Particularly, in the context of the present thesis work it will be interesting to evaluate the high frequency dielectric response, which direct experimental determination is more difficult. Figure 4.13 shows the comparison between the dielectric modelling and the high frequency setup experimental data. As can be observed, a very good description of the data is obtain for blends containing until 50 wt%PS.
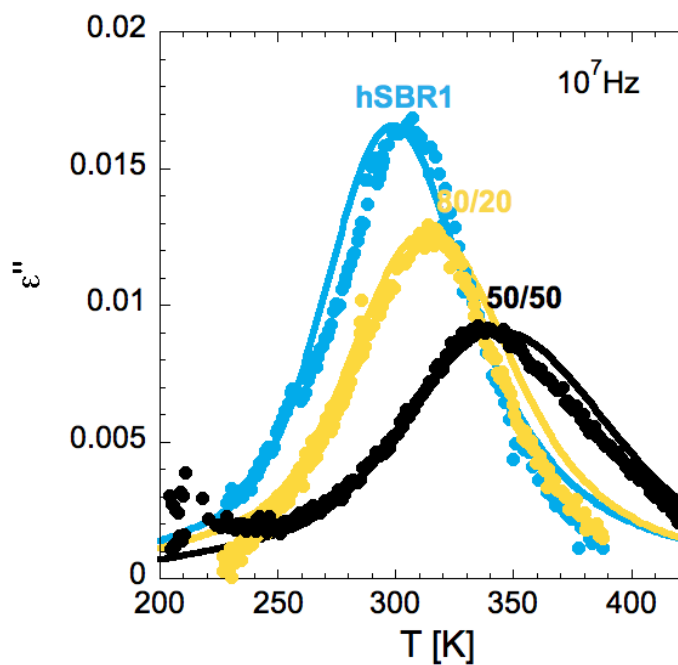
Figure 4.13: Representative dielectric spectra of the pure SBR component and representative blends with respectively 80 wt% and 50 wt% of SBR. The dielectric loss (ε'') is plotted as a function of temperature at $10^7 Hz$. The solid lines stand for the dielectric model prediction using as σ, φ_s^{SBR} and φ_s^{PS} values, the ones predicted by using the equations 4.18, 4.19 and 4.20 for a given composition.

4.3 Conclusions

In this chapter we have shown that, following the study presented in the previous chapter, we are able to model the dielectric behaviour of a simplified industrial system involving the mixture of a random copolymer, SBR with an oligomer, PS. Prior to work on this dielectric model, a complete calorimetric and dielectric study had to be performed for the pure components and the different blends. In this chapter we have then detailed a simple and fully predictive dielectric model which works over a very broad range of concentration in PS in the blends up to 70 wt%. This model is based on the theoretical concepts of thermally driven concentration fluctuations and self-concentration, introduced in the previous chapter. Finally a good agreement is obtained between the experimental results and the outputs of the model using only three fitting parameters. The smooth variation of these 3 parameters with average composition also allows the evaluation of the dielectric relaxation of any intermediate composition. Moreover, we have shown how the model remains also valid for evaluating the dielectric relaxation at higher frequencies. The object of the following chapter will be the combination of the Small Angle Neutron Scattering technique with the dielectric modelling above presented as an efficient way to estimate the size of the relevant volume for the fluctuations of concentrations involved in the dielectric relaxation.

Chapter 5

Concentration fluctuations and scattering in SBR/PS blends

In the previous chapter, we presented a model that permits to well describe the segmental dynamics of SBR/PS blends, two polymers forming a miscible blend the dynamics of each component having very different temperature dependence. By this way, we manage to describe the effect of fluctuation of concentration on the segmental relaxation of this system using only three free parameters, φ_s^{SBR} and φ_s^{PS} the self-concentration accounting for chain connectivity and σ accounting for the width of the distribution of concentrations. In particular, the concept of concentration fluctuations allows to rationalise the extra broadening in the dielectric spectra of the blends which is a consequence of dynamic heterogeneities. The aim of this chapter is to combine the Small Angle Neutron Scattering technique with the dielectric modelling above presented as an efficient way to estimate the size of the relevant volume for the fluctuations of concentrations involved in the dielectric relaxation. Some informations concerning the miscibility of the SBR and PS components will also be deduced from the scattering experiments.

5.1 Concentration Fluctuations

5.1.1 Theory

In this section a short summary of the theory relevant for the characterisation of concentration fluctuation by SANS is first presented in the case of a binary polymer blend. Then the scattering data obtained for SBR/PS blends will be discussed.

For a binary blend of polymer chains of species A and B with corresponding degrees of polymerisation N_A and N_B and volume fractions φ_A and φ_B the

mean-field theory based on the Random Phase Approximation (RPA) predicts [58] :

$$\frac{1}{S(Q)} = \frac{1}{N_A\varphi_A S_A(Q)} + \frac{1}{N_B\varphi_B S_B(Q)} - 2\chi \tag{5.1}$$

where $S_i(Q)$ is the chain form factor of species i and χ the temperature dependent Flory interaction parameter. In a neutron scattering experiment we do not access directly the structure factor $S(Q)$ but the intensity scattered $I(Q)$, which is related with $S(Q)$ as

$$I(Q) = K_n\nu_0 S(Q) \tag{5.2}$$

where ν_0 is the molar volume of a reference unit cell

$$\frac{1}{\nu_0} = \frac{\varphi_A}{\nu_A} + \frac{\varphi_B}{\nu_B} \tag{5.3}$$

and the contrast term K_n can be written as :

$$K_n = \Delta\rho^2 = N_{av}(\frac{a_A}{\nu_A} - \frac{a_B}{\nu_B}) \tag{5.4}$$

with a_i the scattering length and ν_i the monomeric volume of component i and N_{av} is Avogadro's number. In terms of measured magnitude $I(Q)$ the equation 5.1 can be written as:

$$\frac{K_n}{I(Q)} = \frac{1}{N_A\varphi_A\nu_A S_A(Q)} + \frac{1}{N_B\varphi_B\nu_B S_B(Q)} - \frac{2\chi}{\nu_0} \tag{5.5}$$

To describe the intensity measured in the whole experimental window accesses in the Small Angle Neutron Scattering (SANS) measurements, a high-Q incoherent background I_{inc} has to be added to the Ornstein-Zernike (OZ) term $(\frac{I(0)}{1+(Q\xi)^2})$, as well as a lower-Q contribution that can be parametrised in terms of a power law Q^{-x} with x-exponent values around 4. In the Ornstein-Zernike (OZ) equation, ξ represents the correlation length. The scattering intensities at low Q regime are known to reflect the global structures of the material. This drastic upturn toward low Q values as expressed by $I(Q) \sim Q^{-4}$ describes large domain structures with sharp interfaces which can originate from phase separation. In the intermediate Q-range (0.01 Å^{-1}< Q < 0.1 Å^{-1}) I(Q) $\sim Q^{-2}$ and the data can be well described by the Ornstein-Zernike term in the equation 5.6. In this scattering range, the data reflect the local conformation of the chains in the blends and are directly connected to the fluctuation of concentration. Therefore the SANS data can be described over all the measured Q-range in term of the following equation:

$$I_{exp}(Q) = \frac{A}{Q^x} + \frac{I(0)}{1 + (Q\xi)^2} + I_{inc} \tag{5.6}$$

5.1.2 Scattering experiments in SBR/PS blends

In this chapter, in order to increase the contrast between the two components of the blends which leads to more accurate experimental data, we use deuterated samples. The blends here analysed are made by using the protonated Styrene Butadiene Rubber (hSBR2) and the deuterated Polystyrene (dPS) presented in Chapter 2 of this thesis. The blends are prepared following the procedure described in the Chapter 2, in the section 2.1.2. The samples characteristics such as the molar mass or the polydispersity obtained by size exclusion chromatography of the pure components are given in the Table 2.1

Figure 5.1 shows the Small Angle Scattering (SANS) data obtained for the blends with respectively 20, 40, 50 and 70% of polystyrene. In this typical representation, the intensity (I), is plotted in function of the scattering vector (Q) at the different temperature investigated. For all four blends investigated, the scattering intensity, especially in the low Q regime ($Q < 0.06\dot{A}^{-1}$), decreases as the temperature rises, implying that the fluctuation of concentration become larger with decreasing the temperature. This suggests that the blends treated in this study exhibit an Upper Critical Solution Temperature (UCST) type phase diagram. An example of this kind of phase diagram scenario is given in the section 1.3.3 Chapter 1 of this thesis. As can be observed, the SANS experimental data can be well described by means of the equation 5.6. Only for the blend with 20% PS, in the case of highest temperature investigated, the fit has been restricted to $Q > 0.02\dot{A}^{-1}$ assuming $A = 0$. From the Ornstein-Zernike parameters, relevant information in order to characterise the fluctuation of concentration in SBR/PS blends can be obtained.
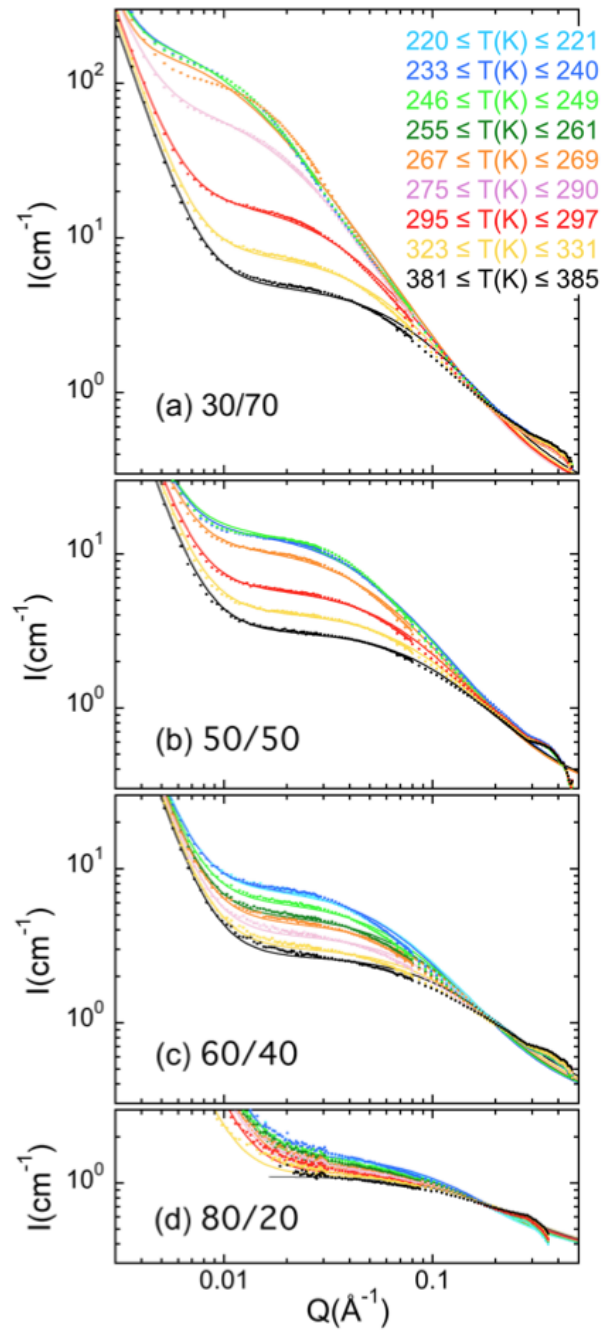
Figure 5.1: Small Angle Neutron Scattering results on the blends with respectively 70% (a), 50% (b), 40% (c) and 20% (d) of polystyrene. The different colours correspond to different temperatures as encoded in panel (a). The solid lines are fits to the equation 5.6 to the experimental data (in the highest temperature investigated for 20%, the fit has been restricted to $Q > 0.02 \mathring{A}^{-1}$ assuming A=0.

In particular, Figure 5.2 (a) shows the temperature dependence of ξ, the correlation length of fluctuation of concentration for the different samples investigated. The correlation length clearly increases at a given temperature when adding polystyrene into the blend. Moreover, although $\xi \simeq 10\mathring{A}$ for the SBR rich blends, in the case of the blend with 70% PS, ξ reaches values close to $100\mathring{A}$ at the lowest measured temperatures.

Figure 5.2 (b) shows the temperature dependence of the second parameter of the Ornstein-Zernike term, the inverse amplitude $I(0)$. The dotted lines show the $(I(0)^{-1})$ linear dependence in function of the inverse of the temperature. From this data, the spinodal temperature can be determined for a given composition by picking up the intersection point of the inverse of the intensity $(I(0)^{-1})$ with the temperature axis (see dashed arrow in Figure 5.2 (b)). By doing this for blends of different composition, the spinodal curve of the SBR/PS system can be constructed. As defined in the section 1.3.3 of the introduction chapter of this thesis, this curve identify the boundary between unstable and metastable regions. The spinodal decomposition occurs because the mixture is locally unstable and any small composition fluctuation is enough to start the phase separation process. The vertical arrows mark the location of the calorimetric glass-transitions for each sample. The different values are summarized in the Table 5.1. The dashed arrows mark the spinodal temperature. As can be observed in the Figure 5.3 for blends until 50% PS the spinodal decomposition is predicted to occur at temperatures much lower than the calorimetric T_g of the sample meaning that, the sample is in his glassy state, well before the phase separation could start to occur.
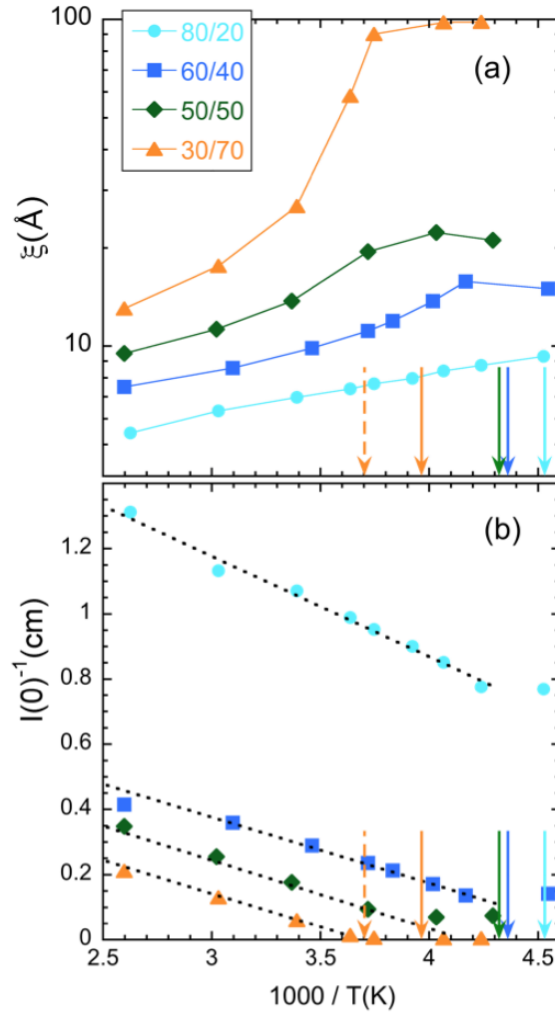
Figure 5.2: Inverse temperature dependence of the parameters involved in the Ornstein-Zernike (OS) contribution of the SANS results: correlation length ξ (a) and inverse of the amplitude $I(0)$ (b). The different symbols correspond to the different compositions investigated, as indicated in panel (a). The vertical arrows mark the location of the glass-transitions for each sample following the same sample code, and the dashed arrow the spinodal temperature. Dotted lines in (b) show linear dependences.

Table 5.1: Evolution of the glass transition temperatures T_gs, determined by picking up the inflection point of the reversible heat flow during cooling at 3K/min for the different samples investigated.

Sample	T_g[K]
hSBR2	214
hSBR2/dPS 80/20	221
hSBR2/dPS 60/40	229
hSBR2/dPS 50/50	232
hSBR2/dPS 30/70	252
dPS	283
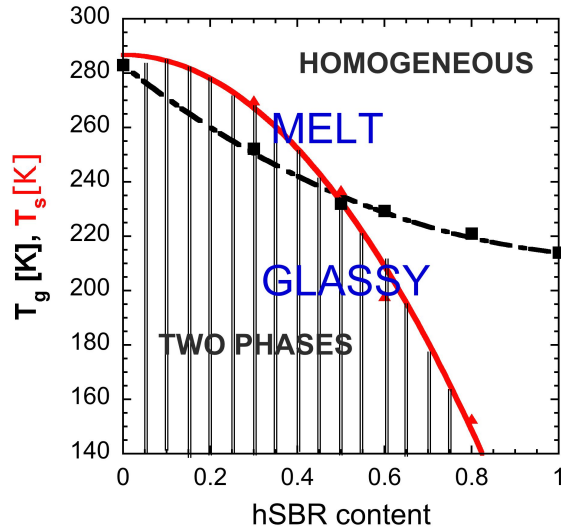
Figure 5.3: Evolution of the glass transition temperature (black squares) and the spinodal temperature (red triangles) in function of the SBR content in the blend. Lines are guides for the eyes. The different phase domains as well as the thermal state are specified.

From this scattering data, one key parameter characterising the miscibility of SBR/PS blends can be also deduced, namely χ the Flory interaction parameter. Since for $Q = 0$, $S_A(0) \equiv S_B(0) \equiv 1$, from the values of $I(0)$ the χ can be determined as a function of temperature. The equation 5.5 can be therefore written as :

$$\frac{K_n}{I(0)} = \frac{1}{N_{PS}\varphi_{PS}\nu_{PS}} + \frac{1}{N_{SBR}(1 - \varphi_{PS})\nu_{SBR}} - \frac{2\chi}{\nu_0} \qquad (5.7)$$

where the degrees of polymerisation are $N_{PS} = 9$, $N_{SBR} = 393$, and the monomeric volumes $\nu_{PS} = 163\mathring{A}^3$, $\nu_{SBR} = 104\mathring{A}^3$.

119

Figure 5.4 shows the PS-volume fraction dependence of the magnitude $K_n/I(0)$ at 267K, 295K, 333K and 385K. χ is left as a free parameter in the equation 5.7 when fitting the $K_n/I(0)$ data. Therefore, χ can be deduced at the four temperatures investigated. The Flory interaction parameter temperature dependence obtained is shown in the inset of the Figure 5.4.
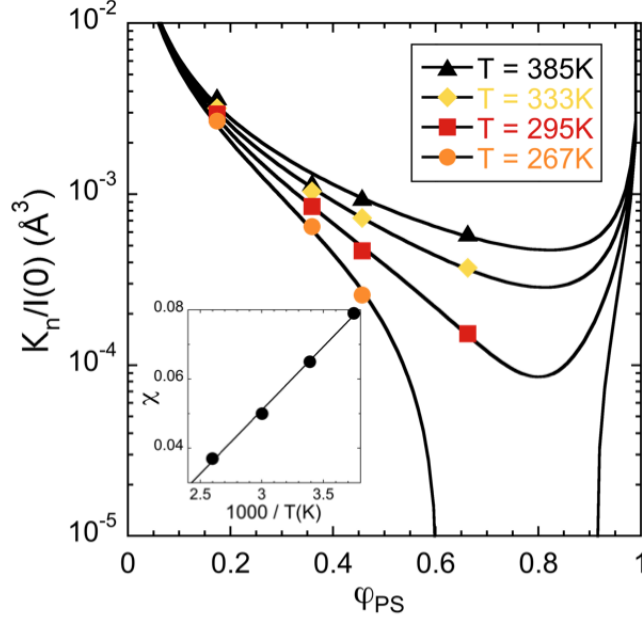
Figure 5.4: PS-volume fraction dependence of the magnitude $K_n/I(0)$ at the four temperatures indicated. Lines are fits to the equation 5.7. The inset shows the inverse temperature dependence of the χ-parameter obtained from these fits. The solid line corresponds to the law $\chi(T) = -0.0593 + 36.76/T(K)$.

As defined in the section 1.3.2 of the introduction chapter of this thesis, the Flory interaction parameter is a dimensionless measure of the difference in strength of pairwise interaction energies between components in the mixture. In the case of SBR/PS blends, the interaction parameter χ is here found positive, which temperature dependence can be express as

$$\chi(T) = A + B/T(K) \qquad (5.8)$$

where $A = -0.0593$ and $B = 36.76$ are respectively the enthalpic and entropic term. $B > 0$ confirms an UCST type behaviour. The solid line in the inset Figure 5.4 stands for the fit by means of the equation 5.8.

5.2 Relating Thermal Concentration Fluctuations with SANS

In this section, we aim to estimate the relevant volume for the fluctuation of concentration.

Fischer et al [1],[36] and later Kant, Kumar and Colby [54] deduced that the mean squared fluctuation of concentration can be expressed as:

$$\langle (\delta\varphi)^2 \rangle = \frac{b^3}{2\pi^2} \int_0^\infty S(Q) \, (QF_Q)^2 \, dQ \tag{5.9}$$

where $S(Q)$ would be given by the RPA approximation and F(Q) would be the form factor of the assumed average volume: a sphere of radius R_c. More recently, Kumar, Colby et al. proposed that for a binary polymer blend the equation 5.9 can be written as:

$$\langle (\delta\varphi_A)^2 \rangle = \langle (\delta\varphi_B)^2 \rangle = \langle (\delta\varphi)^2 \rangle = \frac{\sqrt{\nu_A \nu_B}}{4\pi^2} \int_0^\infty S(Q) \, (QF_Q)^2 \, dQ \tag{5.10}$$

and with some approximations, the previous equation reads as :

$$\langle (\delta\varphi)^2 \rangle = \frac{3\sqrt{\nu_A \nu_B}}{8\pi} \frac{S(0)}{R_c^3} \left\{ 1 - \frac{3(1+\breve{R}_c)^2}{2\breve{R}_c^3} \left[\frac{\breve{R}_c - 1}{\breve{R}_c + 1} + exp(-2\breve{R}_c) \right] \right\} \tag{5.11}$$

with $\breve{R}_c = \frac{R_c}{\xi}$.

If $\breve{R}_c = \frac{R_c}{\xi} < 0.3$. Finally the equation 5.11 can be approximated as: [54]

$$\langle (\delta\varphi)^2 \rangle \cong \frac{\sqrt{\nu_A \nu_B}}{8\pi R_c} \frac{S(0)}{\xi^2} \tag{5.12}$$

That implies that the values of R_c can be obtained if we know $\sigma^2 \equiv < (\delta\varphi)^2 >$ from the dielectric spectroscopy experiments and the value of $S(0)/\xi$ from SANS measurements. Thus, the radius of the sphere, considered as the relevant volume to describe the fluctuation of concentration can be written as:

$$R_c \approx \frac{\sqrt{\nu_A \nu_B}}{8\pi < (\delta\varphi)^2 >} \frac{S(0)}{\xi^2} \tag{5.13}$$

Therefore, an analysis of dielectric spectroscopy experiments on the same samples is required. The samples that have been here presented and analysed by means of Small Angle Neutron Scattering (SANS) were then fully characterised by means of BroadBand Dielectric Spectroscopy and the dielectric modelling procedure above described (see section 4.2.1 in Chapter 4) was carried out again. Figure 5.5 shows the comparison of the dielectric modelling with the experimental dielectric data. As can be observed, a very good description of the experimental data is obtained leading to the determination of the values of the

three fitting parameters, namely φ_s^{SBR}, φ_s^{PS} and σ, which is here the relevant parameter in order to characterise the fluctuations of concentration. From this fits, allowing to disentangled the contribution of each component in the blend as well as the contribution coming from the β-relaxation of the SBR component, we observe that the high frequency dielectric signal is mainly dominated by the SBR component even for blends with high concentration in polystyrene as it was the case for the other set of SBR/PS samples.
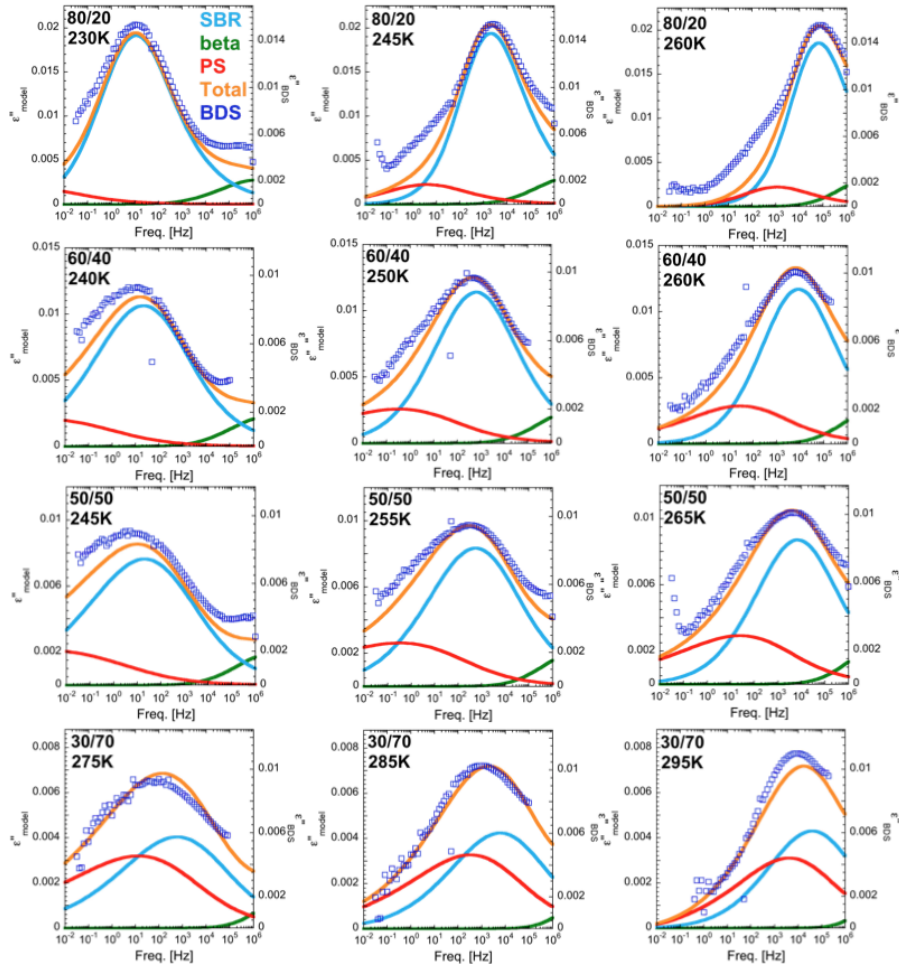
Figure 5.5: Output of the dielectric model compared to the experimental dielectric data for the same sample than the ones analysed by means of Small Angle Neutron Scattering (SANS). The different blends investigated are presented at three different temperatures where the peak corresponding to the α-relaxation is well observed in the experimental window. Blue empty squares stand for the experimental dielectric data. Solid lines stand for the different outputs of the model.

Figure 5.6 shows the concentration dependence of the dielectric modelling fitting parameters values also summarised in Table 5.2. As can be observed in the figure, the values of the parameters obtained from the fitting procedures of the SANS samples (full symbols) follow a very similar behaviour than the one obtained in the previous chapter (empty symbols). Beside the fact that the σ values of the SANS samples were needed in order to estimate the size of the

Table 5.2: Evolution of the dielectric modeling parameters in function of the concentration in SBR in the blend for the samples also investigated by SANS.

wt% SBR in the blend	σ	$\varphi_{s,SBR}$	$\varphi_{s,PS}$
80	0.10	0.35	0.27
60	0.16	0.28	0.25
50	0.18	0.23	0.24
30	0.18	0.05	0.18

relevant volume for concentration fluctuation, the good agreement obtained of the dielectric modelling with the experimental data on a new set of samples with different microstructures, confirms the robustness of the dielectric model above presented.
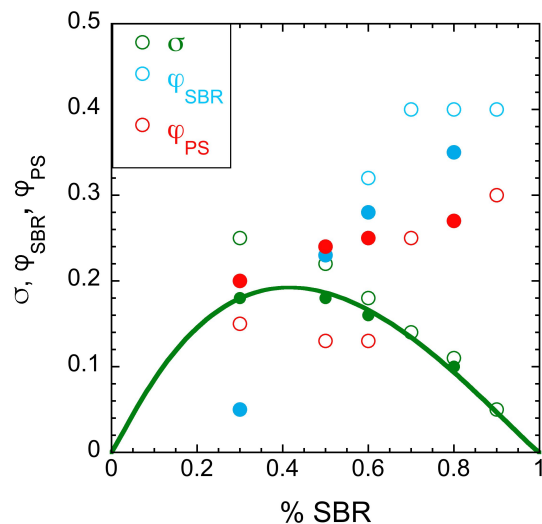
Figure 5.6: Temperature dependence of the dielectric modelling parameters values for the hSBR2/dPS samples (full symbols) compared to the values obtained for hSBR1/hPS1 (empty symbols).

Figure 5.7 shows the temperature dependence of the radius of the correlation sphere R_c for the different samples investigated. As can be observed, the values of R_c are independent of temperature and composition and we found $R_c \simeq 10\mathring{A}$. Therefore, the segmental dynamics of SBR/PS blends are only affected by a local environment of approximate size of $10\mathring{A}$ surronding a test monomer. This estimate of a relevant dynamic length scale is in good agreement with

the length scale generally accepted to be probed by the Dielectric Spectroscopy experiments. In addition, in their work, Kumar, Shenogin and Colby have found a similar average value for R_c for PVME/PoCS and PI/PVE blends, which suggest that the size of the relevant volume for the fluctuation of concentration is not much affected by the nature of the pure components, at least in the framework of binary asymmetric polymer blend.
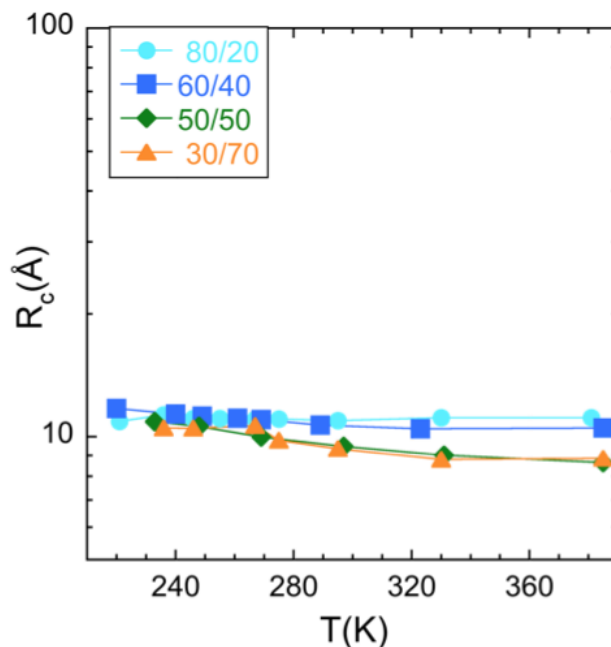
Figure 5.7: Temperature dependence of the radius of the correlation sphere R_c for the blends with respectively 70%, 50%, 40% and 20% of polystyrene.

5.3 Conclusions

In this chapter, the miscibility of the SBR/PS blends have been studied from the SANS experiments, leading to the determination of the temperature dependence of the Flory interaction parameter. The combination of the dielectric modelling and the SANS analysis made possible to estimate the radius of the sphere, taken as the relevant volume to describe the fluctuation of concentration in the blend. This radius is found to be of the order of $10\mathring{A}$, independent of the temperature and the concentration, confirming the conclusions of Kumar and coworkers for other binary miscible polymer blends. In the next chapter, the mechanical characterisation of the samples, as well as the methodology use to predict the high frequency mechanical behaviour of the SBR/PS blends are presented.

Chapter 6

Prediction of the high frequencies mechanical experiments

In the previous chapters a predictive dielectric model for SBR/PS blends in a wide range of concentrations was established and the size of the relevant volume characterising the fluctuation of concentration was estimated. The aim of this final chapter is to predict the high frequency mechanical behaviour of the SBR/PS blends. Regarding the application, the understanding of the mechanical behaviour of the blend at high frequency is very useful in order to design new tire's materials with improved grip properties. Prior to adapt the dielectric model already presented to the mechanical modelling, a complete mechanical characterisation study had to be performed.

6.1 Experimental results

In this section the mechanical experiments of the pure components are presented. The SBR component and the different blends have been previously vulcanised before being characterised by means of Dynamic Mechanical Analysis (DMA). The details of the vulcanization process can be found in the section 3.1.3 (Chapter 3) of this thesis. The pure PS oligomer had to be characterised by means of rheological technique which is more adapted to the measurement of samples that easily flow. As previously mentioned, the vulcanisation does not affect the relaxation of the samples and is only used in order to avoid the samples to flow during the experiments.

6.1.1 Pure components

Figure 6.1(a) shows representative examples of the frequency dependence of the normalized mechanical loss modulus at 227K, 229K and 231K for hSBR1 sample determined by Dynamic Mechanical Analysis. Dynamical mechanical spectra were obtained with a MTS Model 831 Dynamic Mechanical Analysis instrument. The mechanical properties of the samples were recorded varying the temperature from 173 to 373K and the frequency from 0.1 up to 1000Hz. In order to stay in the linear regime small shear deformation close to 0.2% was applied.

Figure 6.1(b) shows the dynamical mechanical spectra obtained with an Ares-LS2 rheometer from TA Instrument using the parallel plate geometry for hPS1 at 308K and 310K. Sample radii and gap were 8mm and 1mm and the dynamic shear modulus was measured from 15 to 0.1Hz at strain of 0.1 %.

For both pure homopolymers, we observed a mean loss peak attributable to the segmental α-relaxation, which peak position strongly depends on temperature. In agreement with the differential scanning calorimetry results presented in the previous chapter, and as already noticed in the dielectric characterisation, the peak of the homopolymers are centred at similar frequencies at much lower temperature for SBR than PS.
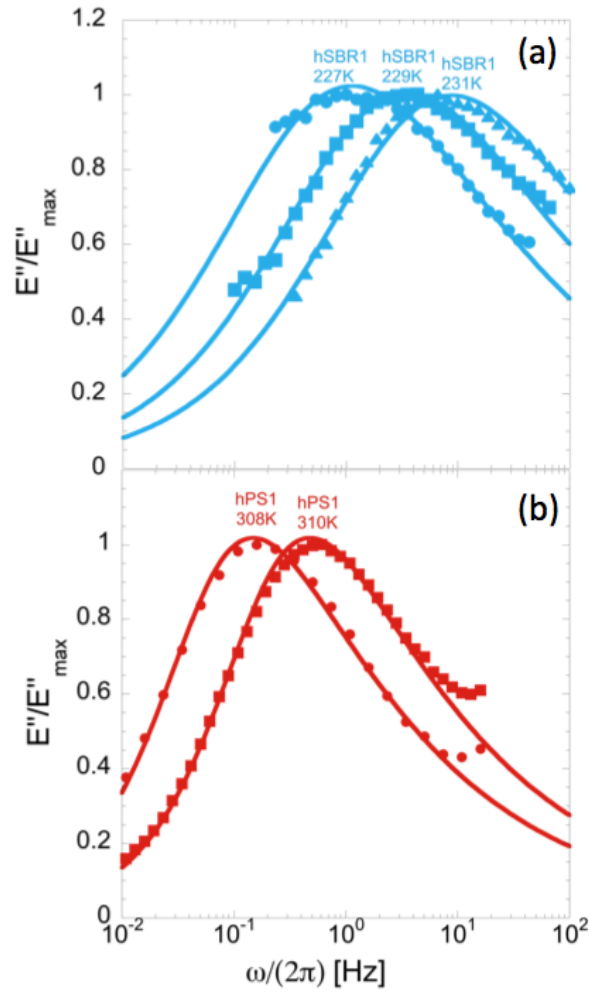
Figure 6.1: (a) Frequency dependence of the normalized mechanical elastic loss modulus at 227K, 229K and 231K for hSBR1 sample determined by Dynamic Mechanical Analysis (DMA). (b) Frequency dependence of the normalized mechanical elastic loss modulus at 308K and 310K for hPS1 sample determined by using the Ares rheometer.

The solid lines in Figure 6.1 stand for the fit by means of the equation 6.2 which corresponds to the Havriliak Negami Equation adapted to mechanical relaxation.

$$E'_{HN}(\omega) = E_\infty - Re\frac{\Delta E}{(1 + (i\omega\tau_M)^{\alpha_M})^{\gamma_M}}. \tag{6.1}$$

$$E_{HN}^{''}(\omega) = -Im\frac{\Delta E}{(1 + (i\omega\tau_M)^{\alpha_M})^{\gamma_M}}. \tag{6.2}$$

Where ΔE is the mechanical relaxation strength, τ_M is the mechanical characteristic relaxation times, and the fractional shape parameters α_M and γ_M describe respectively the symmetric and asymmetric broadening of the complex mechanical function. The values of the Havriliak Negami parameters are resumed in Table 6.1. As can be noticed, it was possible, for both homopolymers, to obtain a good description of the experimental data keeping the α and γ values for the mechanical experimental data equal to the ones found for the dielectric data in the previous chapter. This is particularly interesting in order to construct a model predicting the mechanical relaxation based on the dielectric experiments.

Figure 6.2 shows the temperature dependence of the characteristic times defined from the inverse of the frequencies of the mechanical loss maxima ($\tau_{max} = \omega_{max}^{-1}$) for the α-relaxation of the pure SBR. The line corresponds to the description by means of the VFT Equation (see Equation 1.9) with the values of the parameters reported in Table 6.1. As can be noticed, we have been able to obtain a good description of the data over all the temperature range investigated using, for both homopolymers, the same fragility (D) and Vogel Temperature (T_0) when probed by means of mechanical or dielectric spectroscopy. However the pre-factor (τ_0) was allowed to change respect to the values found for the dielectric data (see Table 4.1 and Table 6.1).

Table 6.1: Parameters involved in the VFT (see Equation 1.9) for the description of the homopolymers characteristic times. The mechanical strength and Havriliak-Negami parameters obtained fitting the curves well centered in the experimental frequency window are also given, as well as the value of the ratio of the pre-factors, τ_0^{DS}/τ_0^{DMA}.

Sample	τ_0^{DS}/τ_0^{DMA}	T_0[K]	D	$\Delta E(GPa)$	α	γ
hSBR1	10	176.9	8.6	2.0	0.57	0.526
hPS1	3.22	256.5	6.3	3.0	0.84	0.37
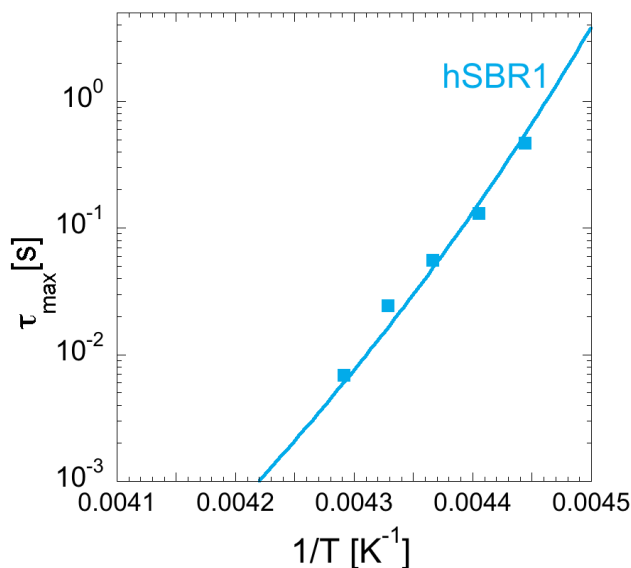
Figure 6.2: Temperature dependence of the characteristic times defined from the inverse of the frequencies of the mechanical loss maxima for the α-relaxation of the hSBR1 sample.

Therefore, with the aforementioned experimental characterisation performed for the pure components it is possible to plot the mechanical relaxation of the pure components at any frequency of interest. Figure 6.3 shows an isochronal representation of both the real and imaginary part of the mechanical modulus for the pure SBR component. It is usually complicated to evaluate with accuracy the mechanical modulus in the low temperature range where the sample is very hard and big forces are involved. Therefore, for both homopolymers, the values of the mechanical strength, namely, ΔE, was taken from the literature [47] where $\Delta E_{PS} = 3GPa$ and $\Delta E_{SBR} = 2GPa$. Moreover, in order to take into account the expected decreasing values of the mechanical strength as the temperature is increasing, the following equations were used:

$$\Delta E_{SBR}(T) = \frac{2GPa \times T_{g,SBR}^{DSC}}{T} \qquad (6.3)$$

$$\Delta E_{PS}(T) = \frac{3GPa \times T_{g,PS}^{DSC}}{T} \qquad (6.4)$$

To compare the model output with the experimental data, a normalized scale was used. Namely, the values at different temperatures were divided by the corresponding real modulus at 210K, a temperature where the mechanical α-relaxation is not active at the analyzed frequencies. In this way the effect of systematic errors associated mainly to inaccuracies in sample geometry would be minimized. As can be noticed, some discrepancies are still observed in the description of the pure SBR sample. These discrepancies mainly origin from the fact that our model is based on the description of the segmental α-relaxation and does not take into account any eventual additional relaxation processes in the sample. The differences mainly notable at high temperature could originate from long-time rearrangement processes namely, the SBR chain Rouse mode. Also at low temperatures the mechanical losses present a plateau-like behavior, most probably associated to the secondary mechanical relaxation of SBR [19]. A similar situation is expected to occur for the blends. Despite of these differences, a good general description of the experimental data of the pure hSBR1 sample is obtained.
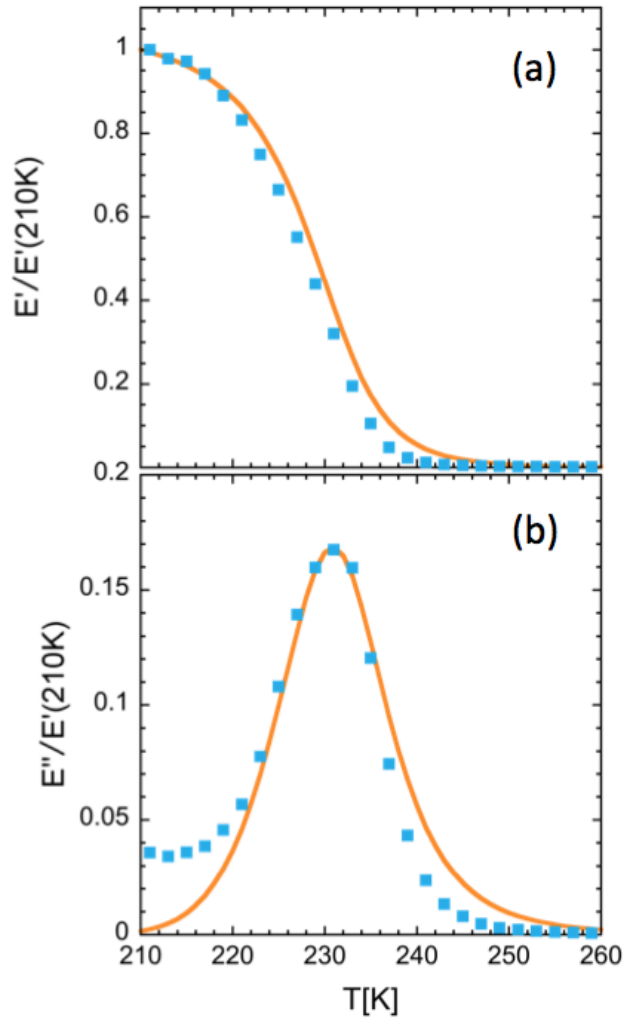
Figure 6.3: Isochronal representation for hSBR1 sample at 10Hz of the real (a) and imaginary part (b) of the normalized mechanical modulus (see text) in function of the temperature. Blue squares are experimental data, orange solid lines stand for the description of the model.

6.2 Modeling the mechanical data of the SBR/PS blends

In this section, a mechanical model based on the dielectric modelling previously introduced is presented. As it has been mentioned in the previous section the dielectric and mechanical relaxations of the SBR and PS components can be de-

scribe by the same Havriliak Negami parameters for the shape of the relaxation. Moreover, as it as been done for the dielectric model, the mechanical strength of each component in the blend is taken from the value corresponding to the pure component weighted by its composition. Concerning the dynamic of the pure components, the same values for the fragility (D) and the Vogel temperature (T_0) can be used for the dielectric or mechanical relaxation. Only the pre-factor value (τ_0) is allow to change respect to the dielectric values in order to describe the mechanical data. The different values of the parameters used in this model are summarised in Table 6.1.

When dealing with dielectric data, the total dielectric permittivity of the blend can be constructed by a simple addition of the dielectric permittivity of each component in the blend (see equation 4.17). However in the case of mechanical variables, the construction of the total complex modulus of the blend, based on the knowledge of the complex modulus of each component in the blend, is much more complicated. In the literature, some attempts [55] to solve this problem have been done, although this still remain a challenging problem to be resolved. These propositions to model the total mechanical modulus of the blend often involve a complex function of the mechanical modulus of the pure components in the blend. Davies and co-worker developed a general analysis for the determination of the effective elastic constants of a macroscopically isotropic and homogeneous two-phase composite material. In their work [25], approximate formulae are given and their validity discussed in terms of the general features of the sample geometry. In this framework, the complex mechanical modulus can be written as follow :

$$E_{AB}^*(\omega)^a = \varphi_A \times E_A^*(\omega)^a + \varphi_B \times E_B^*(\omega)^a \qquad (6.5)$$

This result comes from a particular case of the many-point joint probability function and its mathematical description is out of the scope of this thesis. For more details, the reader is referred to the reference [25]. In order to construct our mechanical model, we made the assumption that equation 6.4 can be used as an approximation to describe the complex mechanical modulus of each sub-volume (i), which implies:

$$E_{Blend,i}^*(\omega)^a = \varphi_i \times (E_{SBR}^* \left[\omega \times \tau(\varphi_i^{SBR}) \right])^a + (1 - \varphi_i) \times (E_{PS}^* \left[\omega \times \tau(\varphi_i^{PS}) \right])^a \qquad (6.6)$$

In addition, in order to describe the macroscopic mechanical modulus of the blend from the mechanical modulus of each sub-volume (i) we also assumed an expression similar to Eq. 6.6. Therefore one can write:

$$E_{Blend}^*(\omega)^a = \sum_i g(\varphi_i) \times E_{Blend,i}^*(\omega)^a \qquad (6.7)$$

where the expression of $g(\varphi_i)$ has been detailed in the equation 4.10.

The two simple ways to average the macroscopic mechanical properties are the models where the representative domains are being sum in parallel (a=1)

or in serie (a= -1). Therefore, by combining the mechanical characterisation of the pure components, and the dielectric modelling previously presented in the chapter 5 for the same set of samples, a mechanical model of the SBR/PS blends can be written with no additional fitting parameters other than those deduced from the dielectric modelling. In order to describe our data we used $a = \frac{1}{5}$ as suggested by Davies and coworkers for samples possessing continuity of both phases.[25]

6.3   Results of the mechanical modeling

In this section, the model above presented (with $a = \frac{1}{5}$) is confronted to the experiments. The results obtained for the model of the mechanical data of the SBR/PS blends are presented for two blends containing 20 wt% and 50 wt% of polystyrene. The comparison is presented at three different temperatures where the peak corresponding to the mechanical segmental α-relaxation are well observed in the experimental window. As can be observed in Figure 6.4 a good description of the experimental data is obtained for both the real and imaginary part of the mechanical modulus for the blend containing 20 wt%PS. In particular this good agreement can be better appreciated for the imaginary part of the mechanical modulus at the intermediate temperature (239K) where the peak corresponding to the mechanical α-relaxation is well centred in the experimental window and therefore more accurate experimental data can be obtained.
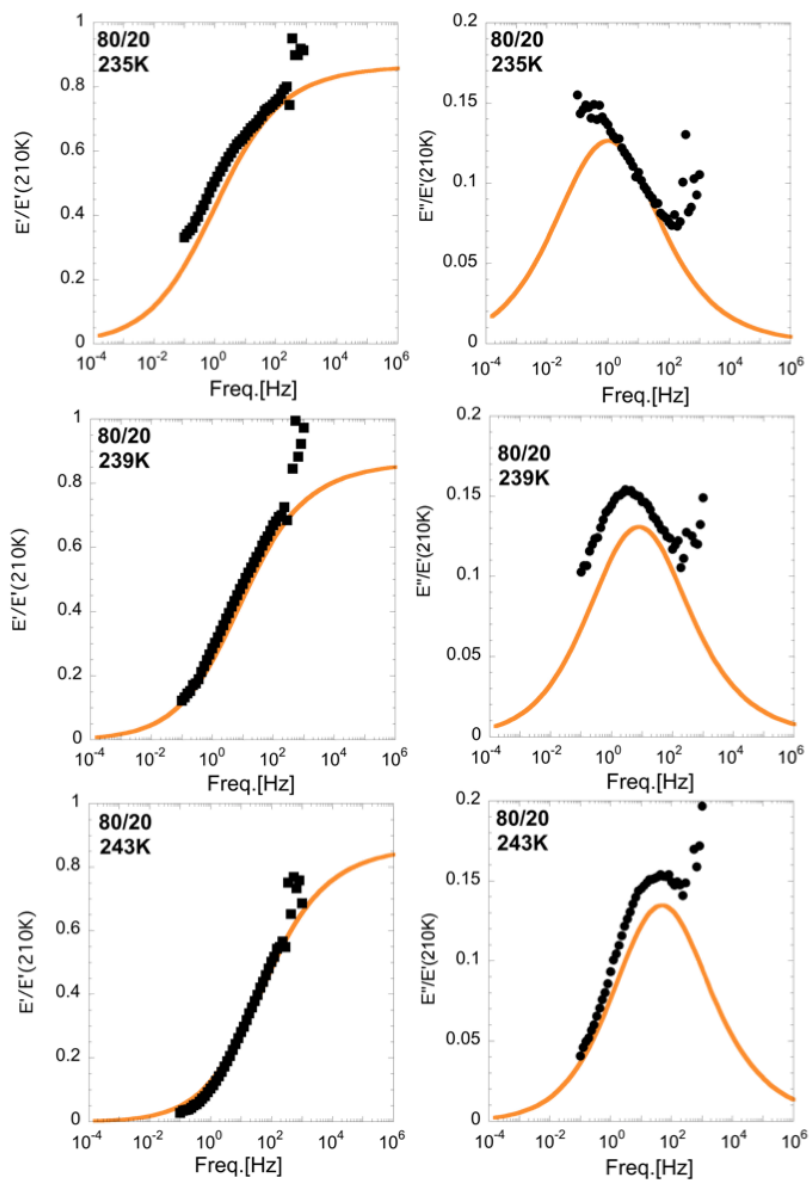
Figure 6.4: Output of the mechanical model compared to the experimental mechanical data (DMA) for the blend with 20 wt%PS. The comparison is presented at three different temperatures where the peak corresponding to the segmental α-relaxation is well observed in the experimental window. Both the real and imaginary part of the mechanical modulus are presented. Black symbols stand for the experimental mechanical data. The orange solid lines stand for the output of the model.

Figure 6.5 shows the output of the mechanical model compared to the experimental mechanical data (DMA) for the blend with 50 wt%PS. In this case, a very good description of the real part of the mechanical modulus is obtained over all the temperature range investigated. However, as can be noticed in Figure 6.5 it is quite challenging to obtain accurate measurements of the imaginary part of the mechanical modulus for samples containing such a high amount of PS. It has to be also notice that, good measurements where not possible in this blend below its glass transition and therefore the normalization to the modulus value at 210 K was made using an arbitrary value to match well the real part at the intermediate temperature.
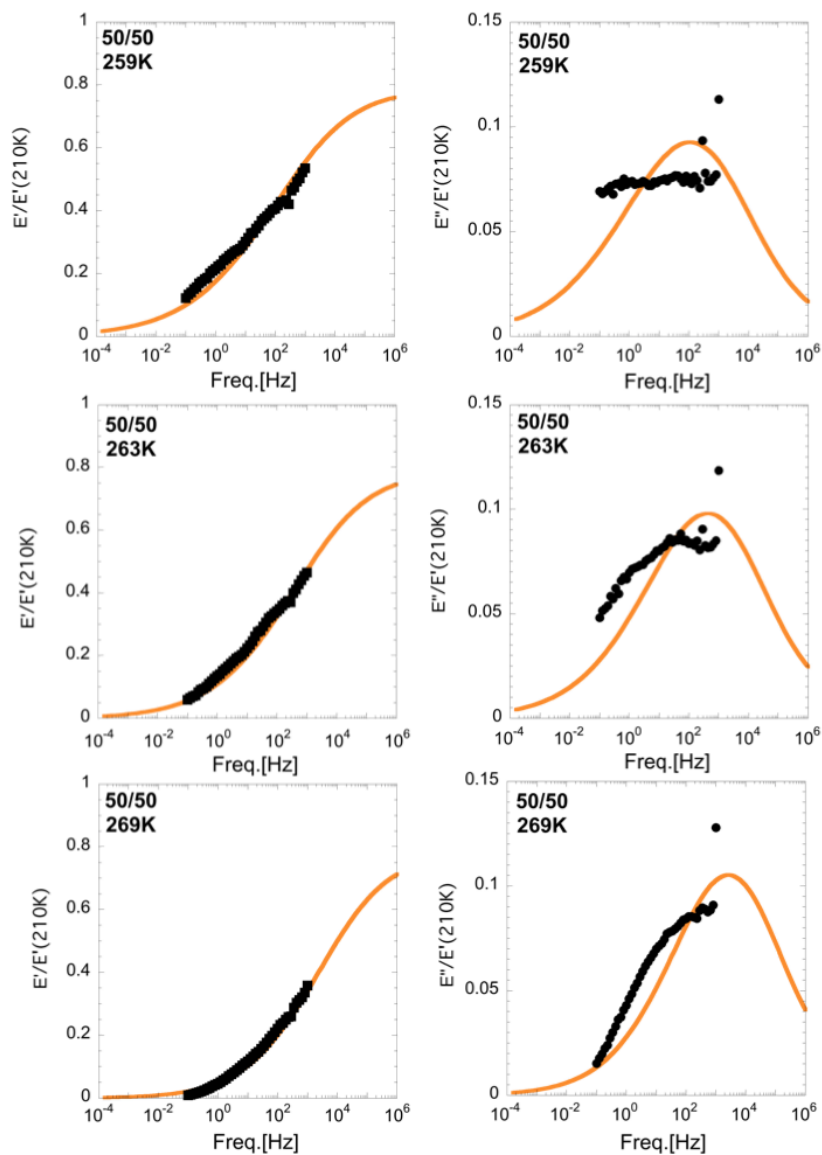
Figure 6.5: Output of the normalised mechanical model compared to the normalised experimental mechanical data (DMA) for the blend with 50 wt%PS. The comparison is presented at three different temperatures where the peak corresponding to the segmental α-relaxation is well observed in the experimental window. Both the real and imaginary part of the mechanical modulus are presented. Black symbols stand for the experimental mechanical data. The orange solid lines stand for the output of the model.

Another way to compare the experimental data with the output of the model is to look at the evolution of the mechanical modulus in function of the temperature namely the isochronal representation. As can be observed in Figure 6.6, both for the real and imaginary part of the mechanical modulus for the 80/20 blend a good agreement between the model and the experimental data is obtained over all the temperature range investigated at a constant frequency of $10Hz$. However some discrepancies are observed in the imaginary part of the mechanical modulus. These low temperature differences can be explained, as in the case of pure SBR, by the presence of a β-relaxation which contribution is not taken into account in the model here presented. Moreover, the model tends also to slightly overestimate the mechanical modulus in the range of temperatures where the imaginary part of the mechanical modulus reaches a maximum. In spite of these minors differences, as can be observed in Figure 6.6, the presented model can be used in order to evaluate the value of the mechanical modulus over all the temperature range of interest and at any desirable frequency. In particular, the mechanical modulus can be estimated at high frequencies ($> 100Hz$) and therefore, overcome the experimental frequency limit that occur when using mechanical spectroscopy. In this example, the mechanical modulus has been estimated for the lower and upper limit of the rolling resistance domain (green solid lines) and the adherence domain (red solid lines).
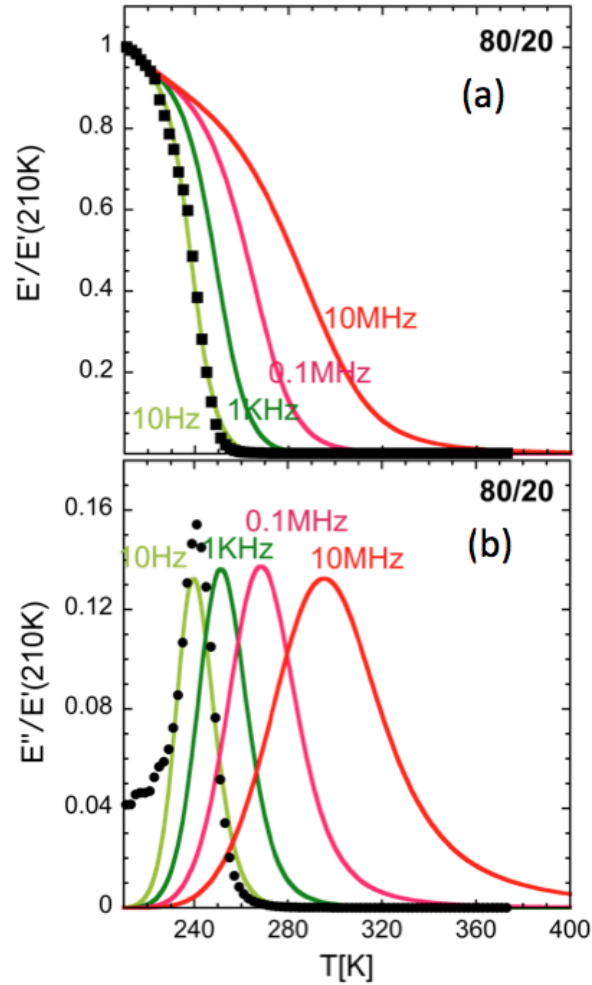
Figure 6.6: Output of the normalised mechanical model compared to the normalised experimental mechanical data (DMA) for the blend with 20 wt%PS. The comparison is presented at three different temperatures where the peak corresponding to the segmental α-relaxation is well observed in the experimental window. Both the real and imaginary part of the mechanical modulus are presented. Black symbols stand for the experimental mechanical data. The solid lines stand for the output of the model.

As can be observed in Figure 6.7 when comparing at $10Hz$ the experimental data and the output of the model for the blend with 50 wt%PS a good agreement is obtained for the description of the real part of the mechanical modulus, although the matching between the experimental data and the model is worse for the imaginary part of the mechanical modulus. For this sample containing

such a high amount of polystyrene, mechanical measurements are challenging due to the high mechanical modulus involve. As can be observed in the Figure 6.7 no reliable data have been measured at temperature inferior at 250K.
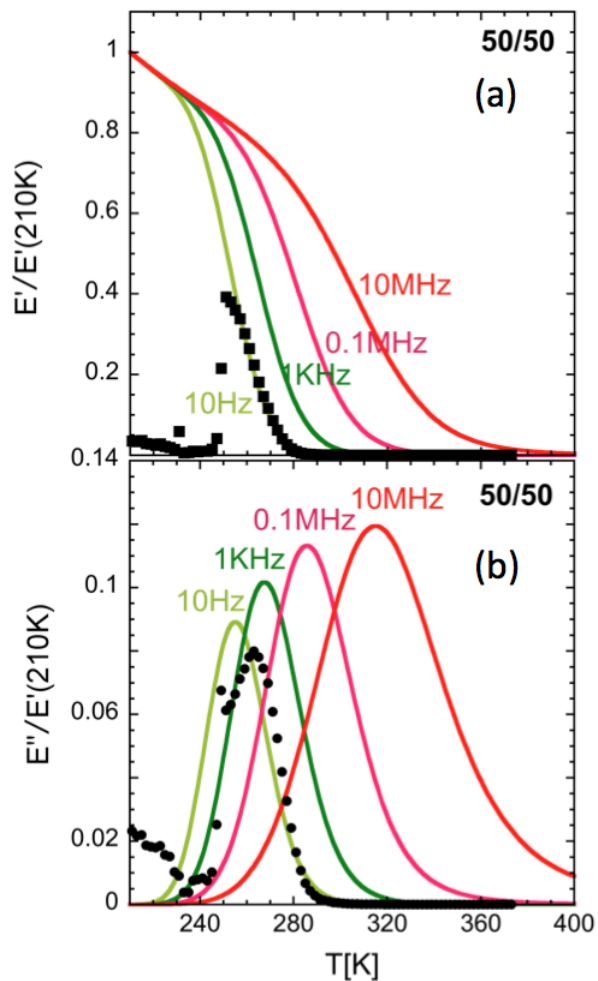
Figure 6.7: Output of the normalised mechanical model compared to the normalised experimental mechanical data (DMA) for the blend with 50 wt%PS at 10Hz. Both the real and imaginary part of the normalised mechanical modulus are presented. Black symbols stand for the normalised experimental mechanical data. The solid lines stand for the output of the model.

As previously mentioned, the model above presented can be used at any temperature, frequency, or concentration in SBR of interest provided the pure components are fully characterized and by interpolating the trends of the three fitting parameters used to describe the dielectric relaxation. Figure 6.8 shows, for

blends with respectively 10, 20, 30. 40 and up to 50% in weight of polystyrene, the curves characterising the mechanical dynamic behaviour of the sample that can be obtained from this model. In these selected concentrations the values of the parameters are available from the fitting of the dielectric data presented in a previous chapter. These curves (central lines) are constructed by picking up the maximum of the imaginary part of the mechanical modulus, in an isochronal representation, at different frequencies of interest. In order to obtain a more accurate idea of the temperature interval in which the sample is able to dissipate energy at a given frequency, one can estimate the Full Width at the Half Maximum (FWHM) of the peak corresponding to the mechanical loss modulus of the sample. By definition, the FWHM is an expression of the extent of function given by the difference between the two extreme values of the independent variable (in our case the temperature) at which the dependent variable (the mechanical loss modulus) is equal to half of its maximum value. As observed in Figure 6.8, adding polystyrene into the blend slows down the total dynamic of the blend, as well as increase the width of the temperature domain in which the sample is able to dissipate energy.
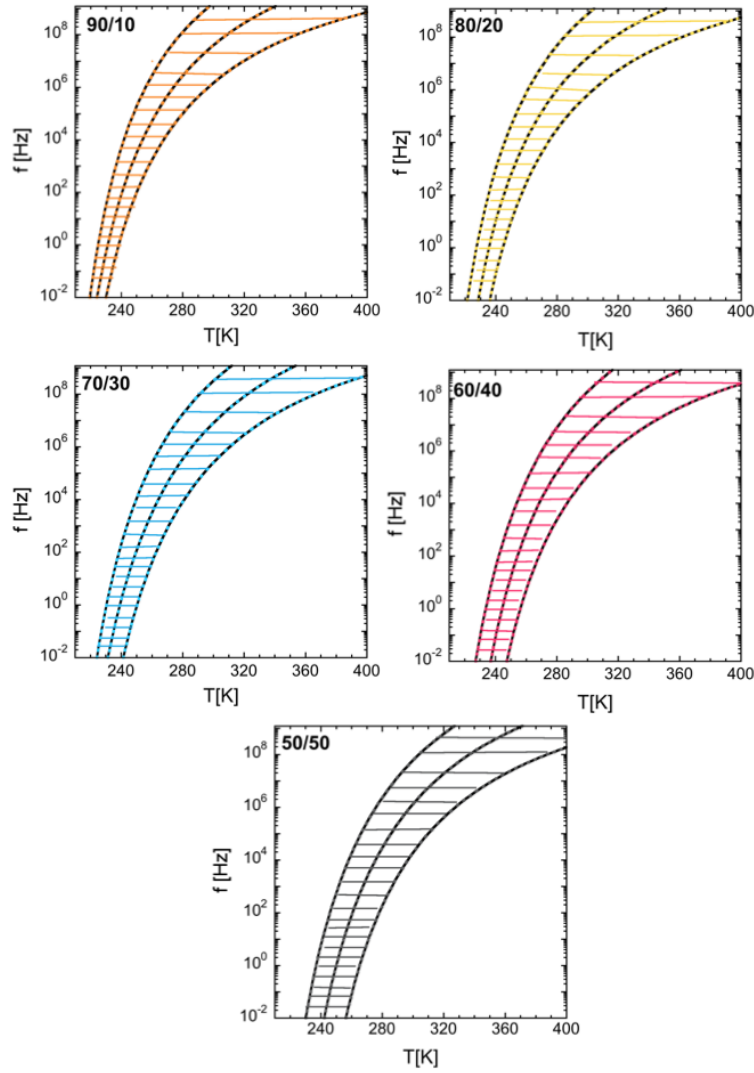
Figure 6.8: Dissipation plot determined using the model above presented (imaginary part of the mechanical modulus, see text) for blends containing respectively 10, 20, 30, 40 and 50 wt%PS.

As it has been shown in this chapter, the Davies formalism allowed to give a good description of the mechanical data of our system using $a = \frac{1}{5}$. One could also wonder about the accuracy of a more simplistic model, such as the model in parallel or in serie, in order to describe our experimental data.

Figure 6.9 shows the output of the parallel model ($a = 1$) compared to the experimental data and the Davies model (using $a = \frac{1}{5}$) for the blend containing 20 wt% of polystyrene at the intermediate temperature of 239K.

142

As can be observed, the parallel model clearly fails to give a good description of the data, especially in the low frequency range, where the real part of the mechanical modulus is clearly overestimated. Moreover, the mechanical loss obtained by using the model in parallel shows a broader and lower intensity peak than the actual experimental data measured by DMA. The model in serie (a= -1) predicts a null mechanical modulus for temperatures superior to 170K and therefore would not be able to describe the mechanical properties of our samples in the temperature range of interest (220-400K).
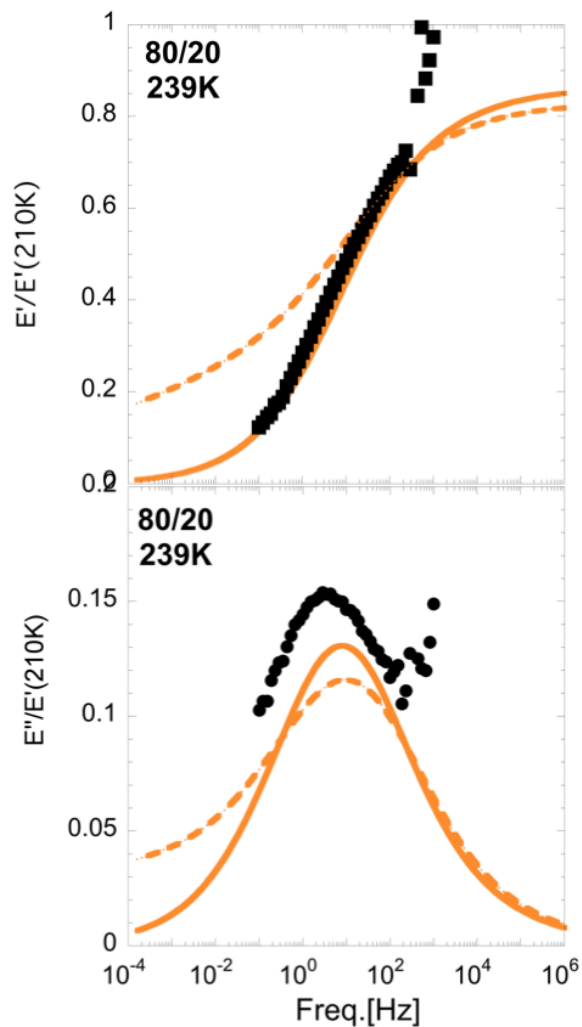
Figure 6.9: Output of the mechanical model compared to the experimental mechanical data (DMA) for the blend with 20 wt%PS. The comparison is presented at 239K where the peak corresponding to the segmental α-relaxation is well observed in the experimental window. Both the real and imaginary part of the mechanical modulus are presented. Black symbols stand for the experimental mechanical data. The orange solid lines stand for the output of the model with $a = \frac{1}{5}$. The orange dash lines stand for the output of the parallel model with $a = 1$.

6.4 Conclusions

In this chapter we have adapted the model previously presented for the modelling of the dielectric relaxation in order to predict the high frequencies mechanical behaviour of SBR/PS blends. This model shows a reasonable agreement with the experimental mechanical data measured for the blends with 20 wt % and 50 wt % of polystyrene for temperatures between 235K and 270K and frequencies from 10^{-1} up to 10^{3}Hz. This model is fully predictive, and can be run at any desirable frequency/temperature and concentration of interest. In particular, by using the model above presented, one can predicted the high frequency mechanical behaviour of the SBR/PS blends, which is impossible to be directly measured by any experimental mechanical characterisation technique.

Chapter 7

Concluding remarks

In this thesis, we have presented a detailed study of the dynamic properties of an elastomer, Styrene Butadiene Rubber (SBR) mixed with an oligomer of polystyrene (PS) allowing to tuned the dynamic properties of the tire tread material. The goal was to understand the plasticizer effect on the temperature dependence of mechanical relaxation in order to improve the performance of the tire such as adherence and decreasing rolling resistance. To do so, a judicious combination of experimental techniques such as Broadband Dielectric Spectroscopy (BDS), Dynamic Mechanical Analysis (DMA) as well as Neutron Scattering instruments (NS) were used, among others complementary techniques.

First, the methodology and concepts developed over the past years for the study of segmental dynamics on miscible polymer blends have been applied to the investigation of a blend of SBR/PS (50/50). In this way we obtain detailed information about the segmental dynamics of both components within the blend. To this end, a combination of broad-band dielectric spectroscopy (BDS) and quasi-elastic neutron scattering (QENS) results on deuterium-labeled blends was required. The strategy for data analysis developed in this work made it possible to readily resolve the components segmental dynamics of the investigated mixtures. It was found that Gaussian distributions of the components effective glass-transition temperatures provide a very good description of all the experimental data collected over the whole accessible temperature range, not only by BDS and QENS but also those obtained by differential scanning calorimetry and by neutron elastic fixed window scan experiments.

Secondly we detailed a simple dielectric model which works over a very broad range of concentration in PS in the blends up to 70 wt%. This model is based on the theoretical concepts of thermally driven concentration fluctuations and self-concentration. A good agreement was obtained between the experimental results and the outputs of the model using only three fitting parameters. The smooth variation of these parameters with average composition also allows the evaluation of the dielectric relaxation of any intermediate composition. Moreover, we have shown how the model remains also valid for evaluating the

dielectric relaxation at higher frequencies.

Then, the miscibility of the SBR/PS blends have been studied from the Small Angle Neutron Scattering (SANS) experiments, leading to the determination of the temperature dependence of the Flory interaction parameter. The combination of the dielectric modelling and the SANS analysis made possible to estimate the radius of the sphere, taken as the relevant volume to describe the fluctuation of concentration in the blend in connection with the segmental dynamics. This radius was found to be of the order of 10 $\mathring{A}$, independent of the temperature and the concentration.

Finally, we have adapted the model previously presented for the modelling of the dielectric relaxation in order to predict the high frequencies mechanical behaviour of SBR/PS blends. This model is fully predictive, and can be run at any desirable frequency/temperature and concentration of interest. In particular, by using the model above presented, one can predicted the high frequency mechanical behaviour of the SBR/PS blends, which is impossible to be directly measured by any experimental mechanical characterisation technique available to date.

The results obtained in this PhD thesis allow to gain a better understanding of the dynamics of polymer blends as well as the prediction of the high frequencies mechanical properties which is a determinant point for significant improvement in the easier design of materials with desired properties.

However, the work here presented was applied to a very simplified industrial system composed of one elastomer and one second component allowing to tune the dynamic properties of the tire tread material. Tires are generally composed of as many as 200 different raw materials, which are combined with rubber compounds to create the various components of a manufactured tire's. In a future work, it would be very interesting to be able to predict the high frequencies mechanical properties of a more "realistic", and therefore more complicated system, by adding for example to the actual system the usual fillers used in the tire industry, such as carbon black and silica, which are well known to improve the mechanical properties of the blend. Also, in practice, SBR as a synthetic rubber, is often substituted in part for natural rubber (NR) based on the comparative raw materials cost. It would be therefore interesting to see how we could adapted the study here presented to ternary blends of NR/SBR/PS.

Bibliography

[1] E. Fischer A. Zetsche. Dielectric studies of the α-relaxation in miscible polymer blends and its relation to concentration fluctuations. *Acta Polym*, 45:168–175, 1994.

[2] Gerold Adam and Julian H Gibbs. On the temperature dependence of cooperative relaxation properties in glass-forming liquids. *The journal of chemical physics*, 43(1):139–146, 1965.

[3] A. Alegría, J. Colmenero, K. L. Ngai, and C. M. Roland. Observation of the component dynamics in a miscible polymer blend by dielectric and mechanical spectroscopies. *Macromolecules*, 27(16):4486–4492, 08 1994.

[4] F. Alvarez, A. Alegría, and J. Colmenero. Relationship between the time-domain kohlrausch-williams-watts and frequency-domain havriliak-negami relaxation functions. *Physical Review B*, 44(14):7306–7312, 10 1991.

[5] F. Alvarez, A. Alegría, and J. Colmenero. Interconnection between frequency-domain havriliak-negami and time-domain kohlrausch-williams-watts relaxation functions. *Physical Review B*, 47(1):125–130, 01 1993.

[6] C. A. Angell. Perspective on the glass transition. *Journal of Physics and Chemistry of Solids*, 49(8):863–871, 1988.

[7] C Austen Angell. Formation of glasses from liquids and biopolymers. *Science*, 267(5206):1924?1935, 1995.

[8] A. Arbe and J. Colmenero. Relaxation processes in liquids and glass-forming systems: What can we learn by comparing neutron scattering and dielectric spectroscopy results? *Kremer, F. Loidl, A. (Eds.) Springer,* **2018**.

[9] A. Arbe, P. Malo de Molina, F. Alvarez, B. Frick, and J. Colmenero. Dielectric susceptibility of liquid water: Microscopic insights from coherent and incoherent neutron scattering. *Physical Review Letters*, 117(18):185501, 10 2016.

[10] A. Arbe, D. Richter, J. Colmenero, and B. Farago. Merging of the α and β relaxations in polybutadiene: A neutron spin echo and dielectric study. *Physical Review E*, 54(4):3853–3869, 10 1996.

[11] S. Arrese-Igor, A. Alegría, A. J. Moreno, and J. Colmenero. Effect of blending on the chain dynamics of the "low-tg" component in nonentangled and dynamically asymmetric polymer blends. *Macromolecules*, 44(9):3611–3621, 05 2011.

[12] S. Arrese-Igor, A. Arbe, B. Frick, and J. Colmenero. Glassy dynamics of polystyrene by quasielastic neutron scattering. *Macromolecules*, 44(8):3161–3168, 04 2011.

[13] M. Bee. Quasielastic neutron scattering. *Adam Hilger, Bristol and Philadelphia*, 54, 1988.

[14] Adrien Bouty, Laurent Petitjean, Julien Chatard, Rachid Matmour, Christophe Degrandcourt, Ralf Schweins, Florian Meneau, Pawel Kwasniewski, Francois Boue, Marc Couty, and Jacques Jestin. Interplay between polymer chain conformation and nanoparticle assembly in model industrial silica/rubber nanocomposites. *Faraday Discuss.*, 186:325–343, 2016.

[15] A. Kaesaman C. Nakason, P. Wannavilai. Effect of vulcanization system on properties of thermoplastic vulcanizates based on epoxidized natural rubber/polypropylene blends. *Polymer Testing*, 25:34?41, 2006.

[16] D. Cangialosi, A. Alegría, and J. Colmenero. "self-concentration"effects on the dynamics of a polychlorinated biphenyl diluted in 1,4-polybutadiene. *The Journal of Chemical Physics*, 126(20), 2018/01/29 2007.

[17] S. Capponi, A. Arbe, F. Alvarez, J. Colmenero, B. Frick, and J. P. Embs. Atomic motions in poly(vinyl methyl ether): A combined study by quasielastic neutron scattering and molecular dynamics simulations in the light of the mode coupling theory. *The Journal of Chemical Physics*, 131(20), 2018/01/29 2009.

[18] I. Cendoya, A. Alegría, J. M. Alberdi, J. Colmenero, H. Grimm, D. Richter, and B. Frick. Effect of blending on the pvme dynamics. a dielectric, nmr, and qens investigation. *Macromolecules*, 32(12):4065–4078, 06 1999.

[19] S Cerveny, A Ghilarducci, H Salva, and A.J Marzocca. Glass-transition and secondary relaxation in sbr-1502 from dynamic mechanical data. *Polymer*, 41(6):2227 – 2230, 2000.

[20] G. C. Chung, J. A. Kornfield, and S. D. Smith. Component dynamics miscible polymer blends: A two-dimensional deuteron nmr investigation. *Macromolecules*, 27(4):964–973, 02 1994.

[21] Morrel H Cohen and GS Grest. Liquid-glass transition, a free-volume approach. *Physical Review B*, 20(3):1077, 1979.

[22] Morrel H Cohen and David Turnbull. Molecular transport in liquids and glasses. *The Journal of Chemical Physics*, 31(5):1164–1169, 1959.

[23] R. H. Cole and K. S. Cole. Dispersion and absorption in dielectrics ii. direct current characteristics. *J. Chem. Phys.*, 54, 2002.

[24] J. Colmenero and A. Arbe. Segmental dynamics in miscible polymer blends: Recent results and open questions. *Soft Matter*, 3(12):1474–1485, 2007.

[25] W E A Davies. The theory of elastic composite materials. *Journal of Physics D: Applied Physics*, 4(9):1325, 1971.

[26] Arthur K Doolittle. Studies in newtonian flow. ii. the dependence of the viscosity of liquids on free-space. *Journal of Applied Physics*, 22(12):1471–1475, 1951.

[27] J. E.; Roland C. M. Erman, B.; Mark. The science and technology of rubber. *Elsevier*, 25:34–41, 2013.

[28] Gordon S. Fulcher. Analysis of Recent Measurements of the Viscosity of Glasses. *Journal of the American Ceramic Society*, 8(6):339–355, June 1925.

[29] G. Goracci, A. Arbe, A. Alegría, Y. Su, U. Gasser, and J. Colmenero. Structure and component dynamics in binary mixtures of poly(2-(dimethylamino)ethyl methacrylate) with water and tetrahydrofuran: A diffraction, calorimetric, and dielectric spectroscopy study. *The Journal of Chemical Physics*, 144(15), 2018/01/30 2016.

[30] A. Guillermo, C. Lartigue, and J. P. Cohen Addad. Peo temporary network in peo/pmma blends: Nmr approach. *Macromolecules*, 31(3):769–775, 02 1998.

[31] T. R. Lutz He, Y. Y. and M. D. Ediger. Segmental and terminal dynamics in miscible polymer mixtures: Tests of the lodge-mcleish model. *J. Chem. Phys.*, 119:9956–9965, 2003.

[32] J. S. Higgins and H. C. Benoît. Polymers and neutron scattering. *Clarendon Press, Oxford*, 54, 1994.

[33] A Hofmann. Secondary and segmental relaxation in polybutadienes of varying microstructure: Dielectric relaxation results. *Macromolecules*, 29(1):129–134, 1996.

[34] Avraam I. Isayev, editor. *Encyclopedia of Polymer Blends, Volume 1: Fundamentals.* Wiley, 2010.

[35] R Kahlau, D Bock, B Schmidtke, and EA Rössler. Dynamics of asymmetric binary glass formers. i. a dielectric and nuclear magnetic resonance spectroscopy study. *The Journal of Chemical Physics*, 140(4):044509, 2014.

[36] R. H.; Kumar S. K.; Karatasos K.; Floudas G.; Fytas G.; Roovers J. E. L. Kamath, S.; Colby. Segmental dynamics of miscible polymer blends: Comparison of the predictions of a concentration fluctuation model to experiment. *J. Chem. Phys.*, 13:6121–6128, 1999.

[37] Andreas Kremer, Friedrich; Schönhals, editor. *Broadband Dielectric Spectroscopy.* Springer, 2003.

[38] R.H; Anastasiadis S.H.; Fytas G. Kumar, S; Colby. Concentration fluctuations induced dynamic heterogeneities in polymer blends. *J. Chem. Phys.*, 9:3777–3788, 1996.

[39] Sanat K. Kumar, Sergei Shenogin, and Ralph H. Colby. Dynamics of miscible polymer blends: Role of concentration fluctuations on characteristic segmental relaxation times. *Macromolecules*, 40(16):5759–5766, 08 2007.

[40] Timothy P. Lodge and Thomas C. B. McLeish. Self-concentrations and effective glass transition temperatures in polymer blends. *Macromolecules*, 33(14):5278–5284, 07 2000.

[41] Timothy P. Lodge, Elizabeth R. Wood, and Jeffrey C. Haley. Two calorimetric glass transitions do not necessarily indicate immiscibility: The case of peo/pmma. *Journal of Polymer Science Part B: Polymer Physics*, 44(4):756–763, 2006.

[42] S. W. Lovesey. Theory of neutron scattering from condensed matter. international series of monographs on physics. *Clarendon Press, Oxford*, 54, 1984.

[43] Xinya Lu and R. A. Weiss. Development of miscible blends of polyamide-6 and manganese sulfonated polystyrene using specific interactions. *Macromolecules*, 24(15):4381–4385, 1991.

[44] Xinya Lu and R. A. Weiss. Relationship between the glass transition temperature and the interaction parameter of miscible binary polymer blends. *Macromolecules*, 25(12):3242–3246, 1992.

[45] Paula Malo de Molina, Fernando Alvarez, Bernhard Frick, Andrew Wildes, Arantxa Arbe, and Juan Colmenero. Investigation of the dynamics of aqueous proline solutions using neutron scattering and molecular dynamics simulations. *Physical Chemistry Chemical Physics*, 19(40):27739–27754, 2017.

[46] A. Narros, A. Arbe, F. Alvarez, J. Colmenero, and D. Richter. Atomic motions in the $\alpha\beta$-merging region of 1,4-polybutadiene: A molecular dynamics simulation study. *The Journal of Chemical Physics*, 128(22):224905, 2008.

[47] J. E. Mark. AIP Press. Physical properties of polymers handbook. *J. E. Mark. AIP Press. Woodbury, N.Y.*, 1996.

[48] D. L. Price and K. Skold. Methods of experimental physics: Neutron scattering. *Academic Press, Orlando.*, 54, 1986.

[49] D. Richter, M. Monkenbusch, A. Arbe, and J. Colmenero. *Neutron Spin Echo in Polymer Systems*, volume 174 of *Adv. Polym. Sci.* Springer Verlag, Berlin Heidelberg New York, 2005.

[50] Jean Marc Saiter, Jean Grenet, Eric Dargent, Allisson Saiter, and Laurent Delbreilh. Glass transition temperature and value of the relaxation time at tg in vitreous polymers. *Macromolecular Symposia*, 258(1):152–161, 2007.

[51] Victoria García Sakai and Arantxa Arbe. Quasielastic neutron scattering in soft matter. *Current Opinion in Colloid and Interface Science*, 14(6):381–390, 2009.

[52] O. Schärpf. Polarization analysis techniques for quasielastic neutron scattering. *Physica B: Condensed Matter*, 182(4):376–388, 1992.

[53] O Scharpf and H Capellmann. *Phys. Status Solidi A*, A27(135):359, 1993.

[54] Sergei Shenogin, Rama Kant, Ralph H. Colby, and Sanat K. Kumar. Dynamics of miscible polymer blends: Predicting the dielectric response. *Macromolecules*, 40(16):5767–5775, 08 2007.

[55] Peiluo Shi, Régis Schach, Etienne Munch, Hélène Montes, and François Lequeux. Glass transition distribution in miscible polymer blends: From calorimetry to rheology. *Macromolecules*, 46(9):3611–3620, 2013.

[56] Chloé Souillard, Laurent Chazeau, Jean-Yves Cavaillé, Sébastien Brun, and Regis Schach. On the beta relaxations in poly(butadiene) and poly(styrene-butadiene) rubbers. *Polymer*, 168:236 – 245, 2019.

[57] J. L. Squires. Introduction to the theory of thermal neutron scattering. *Dover Publiations Inc,New York.*, 54, 1996.

[58] E. Straube. Scaling concepts in polymer physics. von p. g. de gennes. cornell university press. *Acta Polymerica*, 32(5):290–290, 1981.

[59] G. Tammann and W. Hesse. Die Abhängigkeit der Viscosität von der Temperatur bei unterkühlten Flüssigkeiten. *Zeitschrift für anorganische und allgemeine Chemie*, 156(1):245–257, September 1926.

[60] Y. Tanaka, H. Sato, K. Saito, and K. Miyashita. Determination of sequence distribution in styrene-butadiene copolymer. h-nmr study of styrene oligomers. *Rubber Chemistry and Technology.*, 54(4):685–691, 1981.

[61] D. Turnbull and M.H Cohen. Concerning reconstructive transformation and formation of glass. *J. Chem. Phys.*, 29:1049, 1958.

[62] Madhusudan Tyagi, Angel Alegría, and Juan Colmenero. Heterogeneous dynamics of poly(vinyl acetate) far above tg: A combined study by dielectric spectroscopy and quasielastic neutron scattering. *The Journal of Chemical Physics*, 122(24), 2018/01/30 2005.

[63] Oxford University, editor. *Polymer Physics*. New York, 2003.

[64] H. Vogel. The law of the relationship between viscosity of liquids and the temperature. *Physikalische Zeitschrift*, 22:645–646, 1921.

[65] Graham Williams and David C. Watts. Non-symmetrical dielectric relaxation behaviour arising from a simple empirical decay function. *Transactions of the Faraday Society*, 66(0):80–85, 1970.

List of Figures

157

161

List of Tables

Acknowledgements

"Feeling gratitude and not expressing it is like wrapping a present and not giving it." -William Arthur Ward

The successful conclusion of this PhD thesis would not have been possible without the support and encouragement of many people. I would first like to thank Professor Juan Colmenero for giving me the opportunity to join the research group "Polymers and Soft Matter" at the Materials Physics Centre, as well as sharing his experience and expertise with me during these three years. Professor Arantxa Arbe is also acknowledged for introducing me to the field of neutron scattering with patience and constant encouragement. I would like to express my deepest gratitude to Professor Ángel Alegría, my direct supervisor, without whose help this manuscript wouldn't be possible. Thank you Angel, for always finding a moment to share your experience and knowledge with energy and interest. More than the scientific knowledge you shared, the way you taught me to conduct research made my journey toward this PhD an enjoyable experience.

I would like to thank Dr Severin Dronet for his help and support throughout my thesis, is has been nice to work within such a friendly atmosphere. Thank you Dr Nicolas Malicki for your truly helpful scientific thoughts, as well as your encouragement all through this project. Benoît Schnell is also acknowledged for his valuable contribution and insights to this work. Thanks to all of you, and Sophie, my stay in Clermont-ferrand was a really positive experience.

I am grateful to the people of the Centre for Neutron Science (JCNS) at Heinz Maier-Leibnitz Zentrum in Germany for their expert help with the neutron scattering experiments.

I'd like to thank Xavier, Jordan and Jorge, for their fantastic company and for the laughs we shared in CFM as well as the adventures rock climbing or trekking in the Pyrenees. Thank you also to Javier and Amaia for the wonderful atmosphere in the office. Working around people like you makes everything easier.

Many thanks to Amaia, Daniel, Luis, Isabel, Maud, Julen, Paula, Ester, Beatriz, Dani, Ali, Fabienne, Mariarita and Guido for their great company over these years sharing coffee breaks or time abroad at conferences. Thanks also to those who have already moved on towards their next destination Izaskun and Gerardo. Thank you Jon, for the good times shared in Germany or around Euskadi.

To all these people I would like to let them know that I am grateful for the opportunity that I had to work with them.

I also want to mention my comrades from Lyon: François, Aurélien, Quentin and Dylan. The fact that we have stuck together even though we are now scattered throughout Europe makes our friendship even more special to me. Our trips over the past few years have been the best distraction from PhD-life I could imagine. Your stories often motivate the choices I make.

I would also like to thanks the Anoeta running team Florian, Ana, Sergio, who made me feel at home in Basque Country since the very first day I arrived.

I want to give my grateful thanks to my family and Ashleigh, your steady and loving support allow me to reach my personal goals.

Finally, I would like to express my sincere gratitude to anyone not included in this section, but who for even a moment contributed to make these years abroad a wonderful experience.